

MODELING, SIMULATION, AND DESIGN OF A BIPEDAL WALKING ROBOT

by

Turgut Batuhan Baturalp

Submitted to the Institute of Graduate Studies in  
Science and Engineering in partial fulfillment of  
the requirements for the degree of  
Master of Science  
in  
Mechanical Engineering

Yeditepe University

2009

MODELING, SIMULATION AND DESIGN OF A BIPEDAL WALKING ROBOT

APPROVED BY:

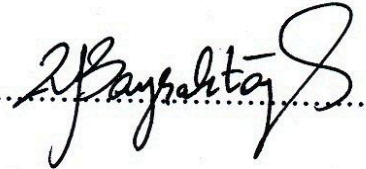
Assist. Prof. Koray K. Şafak  
(Supervisor)

.....  


Assist. Prof. Namık Çıblak

.....  


Assist. Prof. Zeki Y. Bayraktaroğlu

.....  


DATE OF APPROVAL: 25/12/2009

## **ACKNOWLEDGMENTS**

I would like to thank to my advisor Asst. Prof. Koray K. Şafak for his continuous support, ambition and patience during the study. I also thank to TÜBİTAK for supporting to this study. Finally, I would like to thank to my family and my friends for their encouragement.

## **ABSTRACT**

### **MODELING, SIMULATION, AND DESIGN OF A BIPEDAL WALKING ROBOT**

This thesis presents modeling, simulation and design studies within the scope of a Yeditepe University research project entitled “Biomimetic Biped Walking Robot”, which is funded by TUBITAK. In the thesis, modeling and simulation of a 2-linked simple walker, development of a synthetic gait generation algorithm and simulations of anthropomorphic and synthetic gaits on a dynamic model are presented. As the focus is to obtain human-like walking, the robot is designed to resemble human proportions in the CAD environment. Selected electrical and mechanical components are detailed and assembled with structural components. Designed and manufactured biped robot has a height of 1 m and a weight of approximately 20 kilograms. The planar biped robot has 6 actuated joints. A realistic simulation environment is created by using an impact-friction contact model and a faithful CAD model. Parameter based synthetic gaits are generated for this robot model. The trajectories are driven by joints of the robot in dynamic simulations. Results of the simulations indicate that designed robot will be able to realize stable human-like walking motion. Thus, reliability of the simulation environment is verified.

## ÖZET

### **İKİ AYAKLI YÜRÜYEN BİR ROBOTUN MODELLENMESİ, BENZETİMİ VE TASARIMI**

Bu tez, TÜBİTAK destekli “İki Ayaklı Biomimetik Yürüyen Robot” isimli Yeditepe Üniversitesi araştırma projesinin modelleme, benzetim ve tasarım bölümlerini kapsar. Tezde, 2 mafsallı en basit yürüyen mekanizmanın modellenmesi ve benzetimi, bir sentetik yürüyüş algoritmasının geliştirmesi ve dinamik bir modelde sentetik ve antropomorfik yürüyüşlerin gerçekleşmesi anlatılmıştır. Asıl amaç insan benzeri bir yürüyüş elde etmek olduğundan, robotun bilgisayar destekli tasarımı esnasında insan ölçütleri göz önüne alınmıştır. Seçilen elektrikli ve mekanik birleşenler bilgisayar destekli tasarım ortamında detaylandırıldı ve yapısal birleşenler ile montajlandı. Tasarlanan ve üretilen robotun boyu 1 metre, ağırlığı ise yaklaşık 20 kilogramdır. Düzlemsel olan robot motor yardımıyla tahrik edilen 6 adet döner eklemden oluşmaktadır. Aslına uygun robot modeli için sürtünme ve darbe modeli kullanan gerçekçi bir benzetim ortamı oluşturuldu. Aslına uygun robot modeli için parametre temelli sentetik yürüyüş algoritmasından iki farklı yürüyüş yörüngesi sentezlendi. Sentezlenen yürüyüş yörüngeleri dinamik benzetim ortamında döner eklemlere uygulandı. Simülasyon bulguları robotun insan benzeri yürüyüş için uygun olduğunu gösterdi. Böylece benzetim ortamının güvenilirliği doğrulandı.

## TABLE OF CONTENTS

ACKNOWLEDGMENTS .....	iii
ABSTRACT.....	iv
ÖZET .....	v
TABLE OF CONTENTS .....	vi
LIST OF FIGURES.....	viii
LIST OF TABLES .....	xiii
LIST OF SYMBOLS/ABBREVIATIONS.....	xiv
1. INTRODUCTION .....	1
2. LITERATURE SURVEY ON BIPED ROBOTS .....	3
2.1. DESIGN OF BIPEDAL ROBOTS .....	4
2.1.1. Anthropomorphic Designs .....	4
2.1.2. Vertical Hoppers .....	5
2.1.3. Passive Walkers .....	5
2.1.4. Walking Machines.....	6
2.2. GAIT GENERATION FOR BIPEDAL ROBOTS.....	7
2.2.1. Anthropomorphic Gait Generation.....	8
2.2.2. Synthetic Gait Generation.....	9
2.3. CONTROL OF BIPEDAL ROBOTS .....	10
2.3.1. Real-Time Trajectory Generation .....	10
2.3.2. Neural-Oscillatory Control Methods.....	11
3. MODELING AND SIMULATIONS .....	13
3.1. 2D SIMPLEST WALKER .....	13
3.1.1. Dynamic Modeling of 2D Simplest Walker .....	13
3.1.2. An Approximate Analytical Solution for Equations of Motion of 2D Simplest Walker .....	16
3.1.3. The Transition Rule at Heelstrike .....	18
3.1.4. Numerical Solution Method with MATLAB.....	23
3.1.5. Simplest Walker ADAMS Simulation and Comparison with MATLAB Results.....	25

3.2. PARAMETRIC ANALYSIS OF A GENERIC PLANAR BIPED MODEL DRIVEN BY ANTHROPOMORPHIC GAIT DATA .....	28
3.2.1. Parameterization.....	28
3.2.2. Anthropomorphic Gait Data .....	30
3.3. KINEMATICS OF BIPED WALKING .....	34
3.4. ADAMS MODEL OF THE MANUFACTURED ROBOT .....	39
4. DESIGN & PROTOTYPING .....	48
4.1. DRIVE COMPONENTS.....	48
4.1.1. Motor, Gearbox and Control Unit Selection.....	49
4.1.2. Gear Selection .....	51
4.2. STRUCTURAL COMPONENTS .....	54
4.3. LATERAL SUPPORTING SYSTEM.....	55
4.4. ELECTRICAL AND CONTROL SYSTEM DESIGN .....	57
4.4.1. IMU and External Encoders.....	59
4.4.2. Foot Contact Sensors.....	61
4.5. COMPUTER AIDED DESIGN (CAD).....	67
4.5.1. Knee Joint Design .....	68
4.5.2. Hip Joint Design.....	75
4.5.3. Ankle Joint Design .....	76
4.5.4. Foot Design.....	78
4.6. PROTOTYPING.....	78
5. CONCLUSION AND FUTURE WORKS .....	84

## LIST OF FIGURES

Figure 2.1 Computer simulation of human gait for anthropological studies [1] .....	3
Figure 2.2 Raibert's hopper .....	5
Figure 2.3 McGeer's passive dynamic walker.....	6
Figure 2.4 Jerry Pratt's Flamingo.....	7
Figure 2.5 Demonstration of support polygon in single and double support phases .....	8
Figure 3.1 Configuration and parameters of the dynamic model .....	14
Figure 3.2 Simplest walker in after the collision configuration.....	19
Figure 3.3 Simplest walker in before the collision configuration.....	21
Figure 3.4 Simplest walker model in ADAMS software .....	26
Figure 3.5 Superimposed gait images for the simplest walker model in ADAMS software .....	26
Figure 3.6 MATLAB and ADAMS simulation results for the simplest walker.....	27
Figure 3.7 Human segment length proportions with respect to the total height [32].....	29
Figure 3.8 Front and side view of the anthropomorphic parametric ADAMS model .....	30
Figure 3.9 Anthropomorphic gait data in angular position form for each joint.....	31



Figure 3.10 Superimposed view of the anthropomorphic model in ADAMS simulation for one step.....	31
Figure 3.11 Hip velocity along x and y cartesian coordinates.....	32
Figure 3.12 Torque and power diagrams based on anthropomorphic angular acceleration splines applied to the ADAMS model.....	32
Figure 3.13 Trajectory of center of mass in cartesian coordinates .....	33
Figure 3.14 Model and gait parameters of the seven-link planar biped robot.....	35
Figure 3.15 Characteristic behavior and phases of the left and right feet in one period of the gait cycle.....	36
Figure 3.16 Two kinematics results of the knee joint .....	38
Figure 3.17 Walking pattern of general seven link biped robot for one step .....	38
Figure 3.18 ADAMS assembly of the imported CAD models.....	39
Figure 3.19 Walking pattern of prototyped biped robot for two steps of gait 1 .....	42
Figure 3.20 Joint angle position splines for two steps of gait 1.....	42
Figure 3.21 Center of mass location in x and y coordinates for gait 1.....	43
Figure 3.22 Velocity of the hip joint in x and y direction for gait 1 .....	43
Figure 3.23 ADAMS simulation for gait 1 showing superimposed images in every 0.3 s (total of 6.6 s).....	44
Figure 3.24 Walking pattern of the prototyped biped robot for two steps of gait 2 .....	44

Figure 3.25 Joint angle position splines for two steps of gait 2.....	45
Figure 3.26 ADAMS simulation for gait 2 showing superimposed images in every 0.5 s (total of 14 s).....	45
Figure 3.27 ADAMS simulation for gait 2 showing superimposed images in every 0.5 s (total of 8 s).....	46
Figure 3.28 Center of mass location in x and y coordinates for gait 2.....	46
Figure 3.29 Velocity of the hip joint in x and y direction for gait 2 .....	47
Figure 4.1 Screenshot of the Maxon Motor Selection Program (msp) .....	50
Figure 4.2 Knee joint actuator characteristics .....	51
Figure 4.3 Description of joint design and gear force calculation parameters .....	53
Figure 4.4 Vertical collision limitations of robot's movement .....	56
Figure 4.5 Lateral supporting system and robot assembly .....	56
Figure 4.6 Electrical assembly diagram of the sub-systems of the robot.....	58
Figure 4.7 Maxon EPOS2 motor controller [33] .....	59
Figure 4.8 Picture of Nemicon HES external encoder [34].....	60
Figure 4.9 Picture of Microstrain 3D-GX2 Inertial Measurement Unit [35] .....	61
Figure 4.10 Force Sensitive Resistor [36] .....	62
Figure 4.11 Dual-source inverting amplifier circuit for FSR sensors [36].....	63

Figure 4.12 PCB component layout of the FSR sensor circuit .....	64
Figure 4.13 FSR sensor resistance with respect to load .....	65
Figure 4.14 FSR sensor's conductance with respect to load .....	66
Figure 4.15 FSR sensor circuit's $V_{OUT}$ with respect to load .....	66
Figure 4.16 Main dimensions and segment lengths of the robot (mm).....	67
Figure 4.17 Isometric view of CAD of the fully assembled robot.....	68
Figure 4.18 First version of the knee joint design, (May 2008) .....	69
Figure 4.19 Second version of the knee joint design, (July 2008).....	70
Figure 4.20 Third version of the knee joint design, (September 2008).....	71
Figure 4.21 Fourth version of the knee joint design, (October 2008).....	71
Figure 4.22 Fifth version of the knee joint design, (December 2008) .....	72
Figure 4.23 Final version of the knee joint design, (January 2009).....	72
Figure 4.24 Three dimensional view of the knee joint .....	73
Figure 4.25 Exploded view of the knee joint assembly .....	74
Figure 4.26 Three dimensional view of the hip joint .....	75
Figure 4.27 Exploded view of the hip joint assembly .....	76
Figure 4.28 Three dimensional view of the ankle joint.....	77

Figure 4.29 Exploded view of the ankle joint assembly .....	77
Figure 4.30 Exploded view of the foot assembly.....	78
Figure 4.31 First assembled prototype of the knee joint .....	79
Figure 4.32 Assembled knee joint and limbs.....	80
Figure 4.33 Picture of the disassembled hip joint parts.....	81
Figure 4.34 Picture of the assembled hip joint .....	81
Figure 4.35 Picture of the disassembled ankle joint parts .....	82
Figure 4.36 Picture of assembled ankle joint parts .....	82
Figure 4.37 Assembly of the whole robot .....	83

## LIST OF TABLES

Table 3.1 Total robot mass for different heights and materials .....	29
Table 3.2 Joint power and torque values (RMS) for one step with several heights and materials.....	34
Table 3.3 Characteristic via points for cubic splines of foot and ankle trajectories .....	37
Table 3.4 Link length parameters in mm of manufactured robot .....	40
Table 3.5 Gait parameters in mm of manufactured robot .....	40
Table 4.1 Bevel Gear Selection Guide (values are for the knee joint) .....	52
Table 4.2 Bevel Gear Selection Guide (values are for the ankle joint) .....	52
Table 4.3 Structural materials and their properties [38] .....	55

## LIST OF SYMBOLS/ABBREVIATIONS

$Ca_g$	The gear's gear ratio factor
$Ca_p$	The pinion's gear ratio factor
$C_1$	Capacitance of the FSR sensor circuit
$cm_1$	The center of mass of the leg 1
$cm_2$	The center of mass of the leg 2
$D$	Distance of the center of mass from the feet
$d_{o1}$	The pitch diameter of the pinion
$D_s$	The step length
$F$	The contact force
$Fa_g$	The axial force on gear
$Fa_p$	The axial force on pinion
$Fr_g$	The radial force on gear
$Fr_p$	The radial force on pinion
$G$	Gravity vector
$H$	Total height of a ordinary human
$H^+$	The total angular momentum of the system after collision
$H^-$	The total angular momentum of the system before collision
$H_{ao}$	The y coordinate of the highest point of swing foots ankle joint
$H_{ge}$	The height of the ground when the feet as it lands on the ground
$H_{gs}$	The height of the ground when the feet as it leaves on the ground
$H_{max}$	The highest vertical hip position
$H_{min}$	The lowest vertical hip position
$I$	Inertia with respect to the center of mass
$K$	The step number
$L$	The length of the leg
$l_{ab}$	The distance between ankle and heel
$l_{af}$	The distance between ankle and toe
$l_{an}$	The distance between sole and ankle
$L_{ao}$	The x coordinate of the highest point of swing foots ankle joint
$l_{sh}$	The length of the shank link
$l_{th}$	The length of the thigh link

$l_{tr}$	The length of the torso link
$M$	Mass
$N$	The force exponent
$q_b$	The slope angles of the feet as it lands on the ground
$q_f$	The slope angles of the feet as it leaves on the ground
$q_{ge}$	The slope of the ground when the feet as it lands on the ground
$q_{gs}$	The slope of the ground when the feet as it leaves on the ground
$\mathbf{r}$	Position vector
$R_{feedback}$	Feedback resistance of the FSR sensor circuit
$R_{flexiforce}$	Resistance of the FSR sensor
$T$	The total kinetic energy of the system
$T_l$	The maximum input torque
$T_c$	The sum of the single support and double support phases time
$T_d$	The time of the double support phase
$T_m$	The time of middle of the single support period
$U$	The total potential energy of the system
$\mathbf{V}$	Velocity vector
$V_{out}$	Voltage output of the FSR sensor circuit
$V_T$	Test Voltage of the FSR sensor circuit
$x_{ed}$	The distance of along the x-axis from hip to the ankle of the support foot at the end of the single support phase
$x_{sd}$	The distance of along the x-axis from hip to the ankle of the support foot at the start of the single support phase
$\alpha$	Angular acceleration
$\gamma$	The slope angle of the ramped surface
$\theta_1$	The angle between the stance leg and the surface normal
$\theta_2$	The exterior angle between the legs
$\phi$	The interior angle between the legs
$\omega$	Angular velocity
CAD	Computer Aided Design
CAN	Controlled Area Network
COG	Center of Gravity
CPG	Central Pattern Generation

DSP	Double Support Phase
EP	Evolutionary Programming
FSR	Force Sensitive Resistor
GA	Genetic Algorithm
IMU	Inertial Measurement Unit
LED	Light Emitting Diode
LIPM	Linear Inverted Pendulum Method
OGM	Optimal Gradient Method
PC	Personal Computer
PCB	Printed Circuit Board
PR	Personal Robot
RMS	Root Mean Square
Rpm	Revolution per minute
SSP	Single Support Phase
USB	Universal Serial Bus
VIPM	Virtual Inverted Pendulum Method
VMC	Virtual Model Control
ZMP	Zero Moment Point



## 1. INTRODUCTION

Today, development in the robotics technology is made possible to predict the next level of the personal computer (PC) concept will be to personal robot (PR) concept. Personal robot concept can only be true if they can interact directly with human and human environment. Bipedal robots glance at the subject because; design of the human environment is based on bipedalism.

This thesis concentrates on the design and prototyping of a biped robot within a TUBITAK funded research project entitled “Biomimetic Biped Walking Robot”. Design process includes electrical, mechanical and gait designs. Computer aid is intensively used in the design and analyses.

The mechanical design of the robot has been detailed based on the following criteria: human proportions are used to generate a robot gait similar to the natural gait. Another mechanical design criterion is the lightweight design. The robot’s structural frame is made of aluminum. The necessary actuator torques are predicted by simulations. A more compact robot design is more manageable in a research environment. It is easier to handle and less likely to damage itself or harm people around it. Coherence of components and having a modular design with replaceable components are also kept mind during the design process.

Progression of the studies presented in this thesis can be summarized as follows. First, a passive dynamic simplest walker model which has two rigid legs and specific parameters is constructed by using MATLAB and ADAMS software (section 3.1). Then, actuation components selection process has taken place in section 3.2. In this manner, a parametric ADAMS model has been generated with anthropomorphic dimensions for different heights and structural materials. The model is simulated in single support phase by using anthropomorphic gait data. These simulations give an idea on selection of the actuation components. Use of an anthropomorphic gait directly may not be suitable due to differences between human joints and robot’s joints. Hence, a synthetic gait generator is developed in MATLAB (section 3.3). Not only a synthetic gait can be generated for

various link lengths and gait parameters, but also it offers the flexibility of optimization with respect to power, stability or some other performance criterion. Selection of the robot components has started by selecting the drive components (section 4.1). After drive components are worked out, structural and electrical components are selected (section 4.2 to section 4.4). All of the components are combined in Pro/E CAD software (section 4.5). The result of the design phase is a planar biped robot which has a height of 1 m and a weight of approximately 20 kilograms with 6 actuated degrees of freedom. A realistic simulation environment is developed in ADAMS software by generating an faithful model of the manufactured robot. An impact and coulomb friction model is used for simulating interaction of the robot with the ground. Two different gait trajectories are applied to this model and reliability of this simulation environment is verified (section 3.4).

## 2. LITERATURE SURVEY ON BIPED ROBOTS

Walking is a characteristic behavior that has been gained by most of the animal species on earth. In the process of evolution, bipedalism has come along with advantages, like improved ability to see, moving on rough terrain and free forelimbs. So, even natural bipedal walking is changing in a big time scale or a small time scale. As mentioned in [1] by Hase “Over the period of time some of the creatures have shown a remarkable variation in walking modes compared to their ancestral mode, while others continued to walk at the same state. Human mode of walking or current form of biped walking started from quadruped and through an era of evolution gradually changed into the mode of biped walking.”

Figure 2.1 describes the changes in walking pattern first from the early stage of mankind to the walking of human beings in present day in human evolution and then from the childhood learning phase to adulthood.

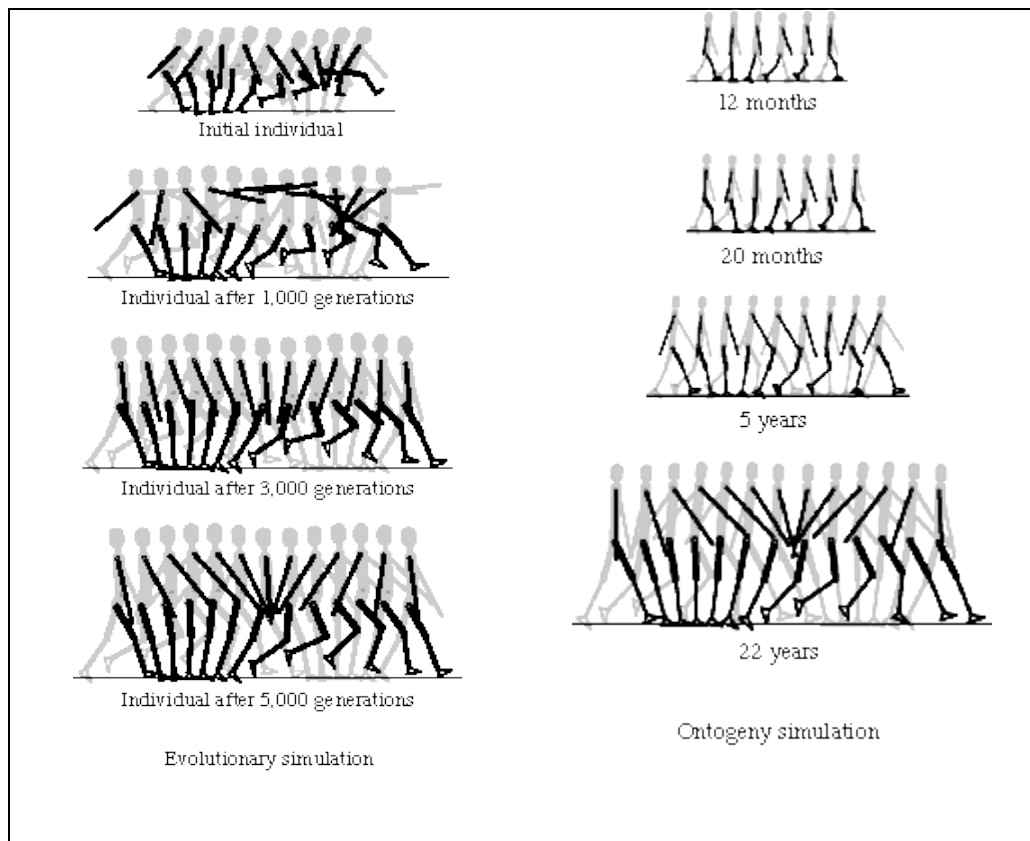


Figure 2.1 Computer simulation of human gait for anthropological studies [1]

The change into biped walking from quadruped walking demanded significant adaptations of the skeleton and muscles. Almost all mammals can stand upright, but a few can walk upright. The mechanical characteristics found in human assist in the control of walking. Today, research on bipedal robots aims making this dream real. In bipedal robot literature, papers can be split into 3 main categories as design, gait and control.

## **2.1. DESIGN OF BIPEDAL ROBOTS**

Research over the past three decades have been dedicated to a number of design approaches, including anthropomorphic designs, vertical hoppers, passive walkers, and planar walking machines. All of these fields of research have made significant impact in the field of biped locomotion.

### **2.1.1. Anthropomorphic Designs**

Waseda University introduced the world to WABOT-1 [2], which is the first to design and implement a successful active walker in 1973. Since then, the most recent breakthroughs in bipedal robots have been made by the Japanese companies Honda and Sony. Both of these bipeds are the products of decades of research and numerous prototypes.

One of the most stunning facets of ASIMO [3] and SDR-3X [4] is their smooth control, and seemingly effortless motions. These are anthropomorphic robots whose motions are achieved by mimicking joint trajectories of humans. Based on the recorded motions, a time-based trajectory was predetermined for each joint. By moving and tracking each joint, sophisticated feedback controls are used to insure that the predetermined trajectories of each joint are achieved by the integration of accelerometers and rate sensors.

While the movements produced by using trajectory tracking control are very impressive, it does not bring us closer to understanding human locomotion or what parameters are most influential in optimizing gait efficiency. This approach does not

feature an intelligent control design that can react to a changing and unpredictable environment on the fly. Additionally, these prototypes have very complex mechanical designs, making it difficult to study new control approaches.

### 2.1.2. Vertical Hoppers

Marc Raibert [5] demonstrated in the late 80's that steady-state running gaits could be accomplished by using a few simple decoupled control laws (see Figure 2.2). This research laid the groundwork for a theory applicable to running robots. Using an event-by-event control approach, the control for each succeeding step is based on the result of the previous step by employing simple laws of physics.

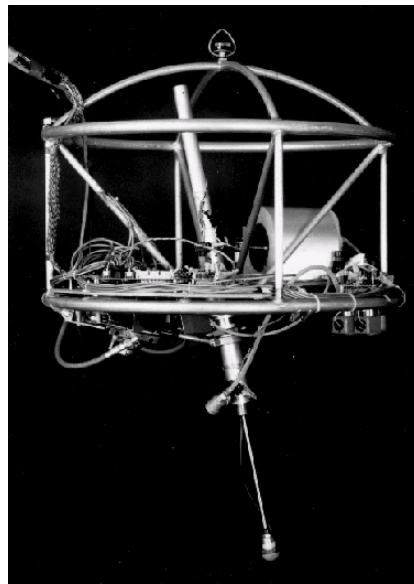


Figure 2.2 Raibert's hopper

### 2.1.3. Passive Walkers

Tad McGeer [6] modeled a no-actuation, no-control walker that is called passive dynamic walker (Figure 2.3). He proved by a physical model and computer simulation that, a passive dynamic walker can walk on a shallow slope. He also noticed that mechanical parameters of a passive dynamic walker have great effect on the range of the stability region.

Goswami et al. [7], [8] investigated the stability and the periodicity properties of the passive dynamic walker, which is termed as the compass gait. They put forward that, not only slope of the inclined plane, but also the mass distribution or geometric parameters affect the stability of the compass gait.

Mark W. Spong [9] tried to add actuation to a passive dynamic walker. He investigated the application of logic-based switching control for the bipedal balance and locomotion problem. He thought switching control is useful due to the complexity of the nonlinear dynamics of under-actuated systems, the nature of disturbances and limits on actuator forces and torques, and there is a change pattern in the structure of dynamics of the bipedal locomotion.

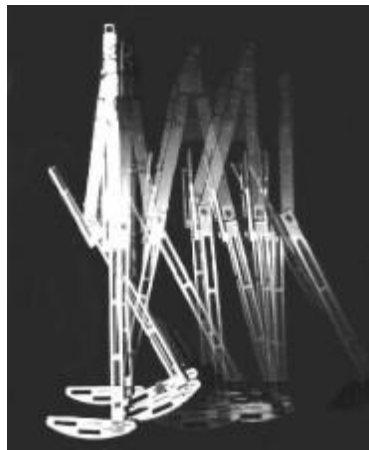


Figure 2.3 McGeer's passive dynamic walker

#### **2.1.4. Walking Machines**

In the late 90's, Jerry Pratt [10] developed Spring Flamingo, the most impressive planar walking machine to date, which made use of a unique control approach known as virtual model control (VMC) (see Figure 2.4). Spring Flamingo was developed to serve as an experimental platform for implementing various control algorithms and force control actuation techniques. The control approach implemented on Spring Flamingo was similar to the one developed by Raibert in that, it used a few simple rules. However, Pratt was the first to successfully implement VMC in walking gaits.



Figure 2.4 Jerry Pratt's Flamingo

## 2.2. GAIT GENERATION FOR BIPEDAL ROBOTS

Gait and walk do not have the same meanings. Gait is a way of walking. Hence biped robots can walk in different gaits. Walking is what you do and gait is how you do it. Gait and its parameters can be defined by the following terms:

A step is defined as in Vukobratovic [10]: “In the direction of motion, during the contact with the ground, the leg from the front position with respect to the trunk comes to the rear position, then it is deployed from the ground and in the transfer phase moves to the front position, to make again contact with the ground, and the cycle is repeated.”

A single walking step includes two phases. These phases are defined in the literature as the double support phase (DSP) and single support phases (SSP). The double support phase occurs when there are two legs in contact with the ground. The single support phase occurs when there is only one leg in contact with the ground. The beginning of a walking cycle can start from either the double or single support phase, but each phase must succeed the other. The single support phase can also be divided into two phases as left (SSP-L) and right (SSP-R) with respect to which foot is in contact with the ground.

The support polygon of a biped is the area whose perimeter corresponds to the footprint outlined by the extents of its feet

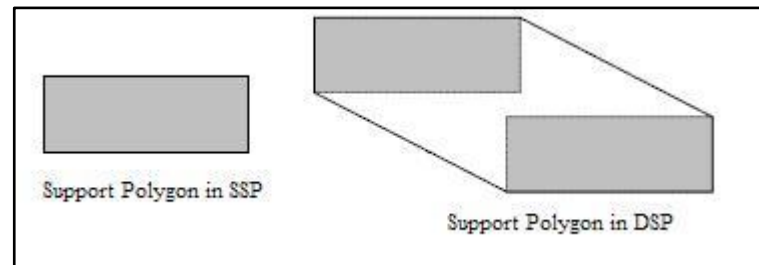


Figure 2.5 Demonstration of support polygon in single and double support phases

Gait generation for biped robots can be divided into two main categories.

### 2.2.1. Anthropomorphic Gait Generation

Gait generation methods use real human gait data that are obtained from gait analysis instruments. Gait analysis commonly involves the measurement of the movement of the body in space (kinematics) and the forces involved in producing these movements (kinetics). Kinematics can be recorded using a variety of systems and methodologies:

Chronophotography is the most basic method for the recording of movement. Strobe lighting at known frequency has been used in the past to aid in the analysis of gait on single photographic images.

Cine film or video recordings using footage from single or multiple cameras can be used to measure joint angles and velocities. This method has been aided by the development of analysis software that greatly simplifies the analysis process and allows for analysis in three dimensions rather than two dimensions only.

Optical marker systems, using reflective markers (typically reflective balls), allow for accurate measurement of movements using multiple cameras (typically five to ten cameras), simultaneously. The cameras send out infra-red light signals and detect the reflection from the markers placed on the body. Based on the angle and time delay between



the original and reflected signal triangulation of the marker in space is possible. These are also used for motion capture in the motion picture industry.

In the literature, ASIMO [3] and SDR-3X [4] bipeds are using anthropomorphic joint trajectories that are obtained by gait analysis of humans.

### **2.2.2. Synthetic Gait Generation**

These methods try to generate a dynamically stable walking pattern offline and they assume that the robot and environment models are available. The created dynamically stable offline trajectories can be optimized due to jerk, stability and power consumption.

Most of the methods belonging to the latter type rely on the ZMP for pattern generation and control (see [12], [13], [14]). Those ZMP-based methods usually require precise knowledge of the robot's dynamics (e.g. mass, center-of-mass location, and inertia of each link) to generate the walking patterns. Hence, they are dependent on the accuracy of the models.

Contrary, there are other methods, which use limited knowledge of the dynamics (e.g. total center-of-mass location, total angular momentum). Since the controller knows a little about the system structure, they rely on a feedback control. Those methods are usually termed as the inverted pendulum approach, since they frequently use variations of the inverted pendulum model. Kajita [15] suggested the Linear Inverted Pendulum Mode (LIPM) and generated center-of-gravity (COG) trajectories using strict linearization of the motion equation. In a further study, Minakata [16] introduced the Virtual Inverted Pendulum Method (VIPM) and used it to vary the walking speed and step length of a "bird-like walking" robot in real-time. Several researchers have also combined motion generation through ZMP manipulation with inverted pendulum models. Napoleon [17] described the limitation of performance using ZMP feedback control with one-mass inverted pendulum model as it is a non-minimum phase system, bearing "undershoot" and "waterbed" effects/problems. Instead, they proposed a two-mass inverted pendulum model and provided the mathematical equations to depict the two-mass inverted pendulum model, in order to force actual ZMP trajectory to become closer to the reference ZMP trajectory.

Offline gait trajectories can be optimized by various methods. One of these methods is genetic algorithm (GA). Arakawa [18] aimed to generate natural motion of a biped robot, similar to human walking in various environments. They applied a hierarchical method through energy optimization consisting of a GA layer that minimized the total energy of all actuators, and an evolutionary programming (EP) layer that optimized interpolated configuration of the biped. By formulating the trajectory generation problem as an energy minimization problem, they applied the hierarchical method.

Nagasaka [19] described another method for optimization of trajectories. Walking patterns based on the ZMP are generated by an optimal gradient method (OGM) in which at first the designer gives prescribed time trajectories of feet, hand and a reference of ZMP. Then, initial trajectories of a trunk are determined based on a static walk. Finally, OGM optimizes the horizontal motion of a trunk to reduce the deviation of the calculated ZMP from its reference. They also show that it can be applied to the yaw moment compensation problem and soles-ground shock compensation problem by simply changing the objective function of OGM.

### **2.3. CONTROL OF BIPEDAL ROBOTS**

Many studies have been conducted on biped locomotion control, and many biped locomotion methods have been proposed. This section of literature survey is going to review these previous studies.

#### **2.3.1. Real-Time Trajectory Generation**

Online motion control methods ignore the environment model and thus can considerably reduce the complexity of biped locomotion. Nevertheless, they are susceptible to real world uncertainties. Thus, the second point of view is from the design of a controller. Some of these controllers have been developed based on momentum feedback control and presented a combination with a preset reference obtained offline gait generation methods (see [20], [21], [22]). Hence, those are considered less robust against disturbances.

Some methods used dynamic filtering to convert an input trajectory to a physically consistent and dynamic trajectory (see [23], [24]). In these methods, the authors generate motions for biped humanoid robots interactively using “dynamics filter” as a motion generator. They state that interactivity is the key issue of many humanoid applications working in a constantly changing environments with humans. Since their filter uses only temporal-local information, they can vary the preset reference trajectory by kinematic combination of several motions in response to the humanoid’s interactions with the environment.

Other inspiring online trajectory generation methods include: Nishiwaki [25] proposed an efficient online method to generate humanoid walking motions, which satisfy a desired upper body trajectories, while simultaneously carrying objects by subsequent updates to motion patterns and connecting them to the old ones in a stable manner, and Kagami [26] proposed a fast dynamically equilibrated trajectory generation method for a humanoid robot. Again, for a given input motion and a desired ZMP trajectory, the algorithm generates a dynamically equilibrated trajectory.

### **2.3.2. Neural-Oscillatory Control Methods**

These control methods are based on the concept that biomimetic combination of artificial neural networks and the biped’s dynamics can realize robust bipedal locomotion control in terms of external disturbances and energy consumption. Most of these methods use Central Pattern Generators (CPGs), neural oscillators proposed by Matsuoka [27] in 1987 which model the firing rate of two mutually inhibiting neurons depicted in a differential equations set. Taga [28] applied CPG for musculoskeletal bipedal control and proved that an adaptive walking motion through various terrains could be realized from the interaction between the neural oscillatory controller and the body and environment dynamics.

Nakanishi [29] proposed a learning method for biped locomotion from human demonstration. The method adapts its frequency using rhythmic dynamical motion primitives as a CPG. In these primitives, the kinematic motion plans are depicted in a nonlinear differential equations set with well-defined attractor dynamics, and demonstrated trajectories

are learned using locally weighted regression. The author's numerical simulations illustrated the effectiveness and within a short term of walking, the simulation discovered an energy efficient walking frequency, roughly at the natural frequency of the combined robot-oscillator environment system.

### 3. MODELING AND SIMULATIONS

#### 3.1. 2D SIMPLEST WALKER

The simplest walker is an irreducibly simple, uncontrolled, 2D, two-link model, vaguely resembling human legs, and can walk down a shallow slope, powered only by gravity (see Figure 3.1). It has two rigid legs hinged at the hip. This linked mechanism moves on a rigid ramp of slope  $\gamma$ . When a foot hits the ground (ramp surface), it has a plastic (no-slip, no-bounce) collision and its velocity jumps to zero. That foot remains on the ground, acting like a hinge, until the swinging foot reaches the ground. During walking, only one foot is in contact with the ground at any time; double support occurs instantaneously. The walker model consists of a 2-D legged mechanism without the knees.

##### 3.1.1. Dynamic Modeling of 2D Simplest Walker

Two angles are used to describe the orientation of the dynamic model of 2D simplest walker.  $\theta_1$  is the angle between the stance leg and the surface normal.  $\theta_2$  is the exterior angle between the legs. If this system is considered as an inverted pendulum,  $\theta_2$  is the angle relative to  $\theta_1$ . Points denoted by  $cm_1$  and  $cm_2$  are the center of mass of the legs and that are located at a distance  $d$  from the feet. Each leg has inertia,  $I$  with respect to the center of mass, mass  $m$  and length  $L$ . The slope angle of the ramped surface is  $\gamma$ . Illustration of configuration and parameters of the dynamic model can be seen in Figure 3.1. Stance leg in the figure is subscripted as 1 and swing leg as 2. Hip joint is subscripted in the equations as 0. This approach is inspired from a study in Cornell University [30].

The model's motion is governed by the laws of classical rigid-body mechanics. A non-physical assumption has been considered that the swing foot can briefly pass through the ramp surface when the stance leg is near vertical. This concession is made to avoid the inevitable scuffing problems of straight legged walkers.

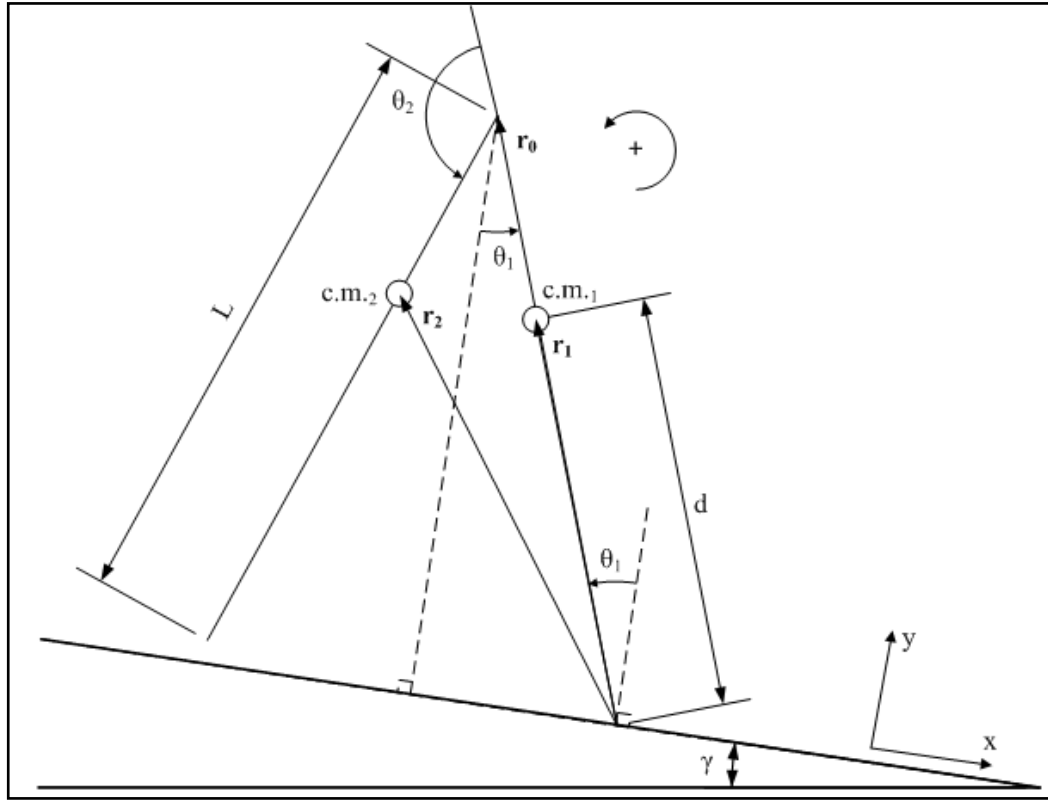


Figure 3.1 Configuration and parameters of the dynamic model

Position vectors are calculated for stance leg, swing leg and hip as:

$$\mathbf{r}_1 = [-\sin(\theta_1) d]\mathbf{i} + [\cos(\theta_1) d]\mathbf{j} \quad (3.1)$$

$$\mathbf{r}_0 = [-\sin(\theta_1) L]\mathbf{i} + [\cos(\theta_1) L]\mathbf{j} \quad (3.2)$$

$$\begin{aligned} \mathbf{r}_2 = & [-\sin(\theta_1)L - \sin(\theta_1 + \theta_2)(L - d)]\mathbf{i} \\ & + [\cos(\theta_1)L + \cos(\theta_1 + \theta_2)(L - d)]\mathbf{j} \end{aligned} \quad (3.3)$$

Acceleration due to gravity is rotated with respect to  $\gamma$  to convert it from global frame to local frame.

$$\mathbf{g} = [g \sin(\gamma)]\mathbf{i} + [-g \cos(\gamma)]\mathbf{j} \quad (3.4)$$

$$\omega_1 = \dot{\theta}_1, \quad \omega_2 = \dot{\theta}_1 + \dot{\theta}_2 \quad (3.5)$$

$$\mathbf{V}_1 = \frac{d}{dt} \mathbf{r}_1, \quad \mathbf{V}_2 = \frac{d}{dt} \mathbf{r}_2 \quad (3.6)$$

Lagrangian dynamics is used to derive the equations of motion. Thus, from energy point of view, T and U are the total kinetic and potential energies of the system.

$$T = \frac{1}{2} \{ I \dot{\theta}_1^2 + I (\dot{\theta}_1 + \dot{\theta}_2)^2 + m d^2 \dot{\theta}_1^2 \} \quad (3.7)$$

$$+ m \left[ \dot{\theta}_1^2 L^2 + (\dot{\theta}_1 + \dot{\theta}_2)^2 (L - d)^2 + 2(\dot{\theta}_1 + \dot{\theta}_2) \dot{\theta}_1 L (L - d) \cos(\theta_2) \right]$$

$$U = mg [\cos(\theta_1 - \gamma) (L + d) + \cos(\theta_1 + \theta_2 - \gamma) (L - d)] \quad (3.8)$$

$$L = T - U \quad (3.9)$$

Lagrangian formulation for the equations of motion results:

$$0 = \frac{d}{dt} \left( \frac{dL}{d\dot{\theta}_1} \right) - \frac{dL}{d\theta_1} \quad (3.10)$$

$$0 = \frac{d}{dt} \left( \frac{dL}{d\dot{\theta}_2} \right) - \frac{dL}{d\theta_2} \quad (3.11)$$

Non-linear equations of motion are obtained from derivatives of Lagrangian. To solve these equations of motion analytically linearization is required. Following linearized set of expressions are obtained:

$$\theta_1 \approx 0, \quad \theta_2 \approx \pi \quad (3.12)$$

$$\sin(\theta_1) \cong \theta_1, \quad \cos(\theta_1) \cong 1 \quad (3.13)$$

$$\sin(\theta_2) \cong \pi - \theta_2, \cos(\theta_2) \cong -1 \quad (3.14)$$

$$\dot{\theta}_1^2 \cong \dot{\theta}_2^2 \cong \dot{\theta}_1 \dot{\theta}_2 \cong 0 \quad (3.15)$$

So we obtained a set of linearized equation of motion in state-space form.

$$\begin{aligned} & \begin{bmatrix} 2I + 2md^2 & I + md(d-L) \\ I + md(d-L) & I + m(L-d)^2 \end{bmatrix} \begin{bmatrix} \ddot{\theta}_1 \\ \ddot{\theta}_2 \end{bmatrix} + \begin{bmatrix} -2mgd & mg(L-d) \\ mg(L-d) & mg(L-d) \end{bmatrix} \begin{bmatrix} \theta_1 \\ \theta_2 \end{bmatrix} \\ & = \begin{bmatrix} mg(\pi(L-d) - 2d\gamma) \\ mg(L-d)(\pi + \gamma) \end{bmatrix} \end{aligned} \quad (3.16)$$

### 3.1.2. An Approximate Analytical Solution for Equations of Motion of 2D Simplest Walker

State-space equations of motion are solved by following formulations and assumptions [31]:

$$\begin{bmatrix} a_{11} & a_{12} \\ a_{21} & a_{22} \end{bmatrix} \begin{bmatrix} \ddot{\theta}_1 \\ \ddot{\theta}_2 \end{bmatrix} + \begin{bmatrix} b_{11} & b_{12} \\ b_{21} & b_{22} \end{bmatrix} \begin{bmatrix} \theta_1 \\ \theta_2 \end{bmatrix} = \begin{bmatrix} c_1 \\ c_2 \end{bmatrix} \quad (3.17)$$

$$\mathbf{A}\ddot{\theta} + \mathbf{B}\theta = \mathbf{C} \quad (3.18)$$

$$\mathbf{A}^{-1}(\mathbf{A}\ddot{\theta} + \mathbf{B}\theta) = \mathbf{A}^{-1}\mathbf{C} \quad (3.19)$$

$$\ddot{\theta} = \mathbf{A}^{-1}\mathbf{C} - \mathbf{A}^{-1}\mathbf{B}\theta \quad (3.20)$$

$$\begin{bmatrix} \ddot{\theta}_1 \\ \ddot{\theta}_2 \end{bmatrix} = \underbrace{\mathbf{A}^{-1}\mathbf{C}}_{\mathbf{D}} + \underbrace{(-\mathbf{A}^{-1}\mathbf{B})}_{\mathbf{E}} \begin{bmatrix} \theta_1 \\ \theta_2 \end{bmatrix} \quad (3.21)$$

If we define  $\mathbf{D} = \mathbf{A}^{-1}\mathbf{C}$  and  $\mathbf{E} = -\mathbf{A}^{-1}\mathbf{B}$ , new representation of state-space equations will be:



$$\begin{bmatrix} \ddot{\theta}_1 \\ \ddot{\theta}_2 \end{bmatrix} = \begin{bmatrix} d_1 \\ d_2 \end{bmatrix} + \begin{bmatrix} e_{11} & e_{12} \\ e_{21} & e_{22} \end{bmatrix} \begin{bmatrix} \theta_1 \\ \theta_2 \end{bmatrix} \quad (3.22)$$

$$\dot{\mathbf{y}} = \begin{bmatrix} \dot{\theta}_1 \\ \dot{\theta}_1 \\ \dot{\theta}_2 \\ \dot{\theta}_2 \end{bmatrix} = \underbrace{\begin{bmatrix} 0 \\ d_1 \\ 0 \\ d_2 \end{bmatrix}}_{\mathbf{P}} + \underbrace{\begin{bmatrix} 0 & 1 & 0 & 0 \\ e_{11} & 0 & e_{12} & 0 \\ 0 & 0 & 0 & 1 \\ e_{21} & 0 & e_{22} & 0 \end{bmatrix}}_{\mathbf{Q}} \begin{bmatrix} \theta_1 \\ \dot{\theta}_1 \\ \theta_2 \\ \dot{\theta}_2 \end{bmatrix} \quad (3.23)$$

If we set  $\mathbf{P} = \begin{bmatrix} 0 \\ d_1 \\ 0 \\ d_2 \end{bmatrix}$  and  $\mathbf{Q} = \begin{bmatrix} 0 & 1 & 0 & 0 \\ e_{11} & 0 & e_{12} & 0 \\ 0 & 0 & 0 & 1 \\ e_{21} & 0 & e_{22} & 0 \end{bmatrix}$ , The equation becomes a non-

homogeneous ordinary differential equation that can be expressed as:

$$\dot{\mathbf{y}} = \mathbf{P} + \mathbf{Q}\mathbf{y} \quad (3.24)$$

For solving homogeneous part we set  $\mathbf{P} = 0$

$$\dot{\mathbf{y}} = \mathbf{Q}\mathbf{y} \quad (3.25)$$

And the solution can be expressed as:

$$\mathbf{y} = \mathbf{x}e^{\lambda t} \quad (3.26)$$

Where  $\mathbf{x}$  is the matrix of eigenvectors and  $\lambda$  is the vector of eigen values of  $\mathbf{Q}$ .

$$\begin{bmatrix} \theta_1 \\ \dot{\theta}_1 \\ \theta_2 \\ \dot{\theta}_2 \end{bmatrix} = \mathbf{y} = c_1\mathbf{x}^{(1)}e^{\lambda_1 t} + c_2\mathbf{x}^{(2)}e^{\lambda_2 t} + c_3\mathbf{x}^{(3)}e^{\lambda_3 t} + c_4\mathbf{x}^{(4)}e^{\lambda_4 t} \quad (3.27)$$

$$\mathbf{x} = [\mathbf{x}^{(1)} : \mathbf{x}^{(2)} : \mathbf{x}^{(3)} : \mathbf{x}^{(4)}] \quad (3.28)$$

For particular solution:

$$0 = \mathbf{P} + \mathbf{Q}\mathbf{y} \quad (3.29)$$

$$\mathbf{y}_p = -\mathbf{Q}^{-1}\mathbf{P} \quad (3.30)$$

$$\mathbf{y}_p = \begin{bmatrix} \gamma \\ 0 \\ \pi \\ 0 \end{bmatrix} \quad (3.31)$$

Finally general solution is obtained.

$$\begin{bmatrix} \theta_1 \\ \dot{\theta}_1 \\ \theta_2 \\ \dot{\theta}_2 \end{bmatrix} = \mathbf{y} = \begin{bmatrix} \gamma \\ 0 \\ \pi \\ 0 \end{bmatrix} + c_1 \mathbf{x}^{(1)} e^{\lambda_1 t} + c_2 \mathbf{x}^{(2)} e^{\lambda_2 t} + c_3 \mathbf{x}^{(3)} e^{\lambda_3 t} + c_4 \mathbf{x}^{(4)} e^{\lambda_4 t} \quad (3.32)$$

### 3.1.3. The Transition Rule at Heelstrike

While one step is modeled and solved in the previous sections, for multiple steps a transition rule is required to continue the walking. Transition rule is applied when the swing foot hits the ground at heelstrike. To derive the transition rule at heelstrike, best way is to divide the collision into two instants as just before and just after the collision. Between those instants conservation of angular momentum is applied. Angular momentum of the system is considered conserved about the point, which is in contact with the ground. A superscript definition is utilized to denote the parameters after the collision as + and before the collision as -. Configuration of the model and parameters after the collision is shown in Figure 3.2.

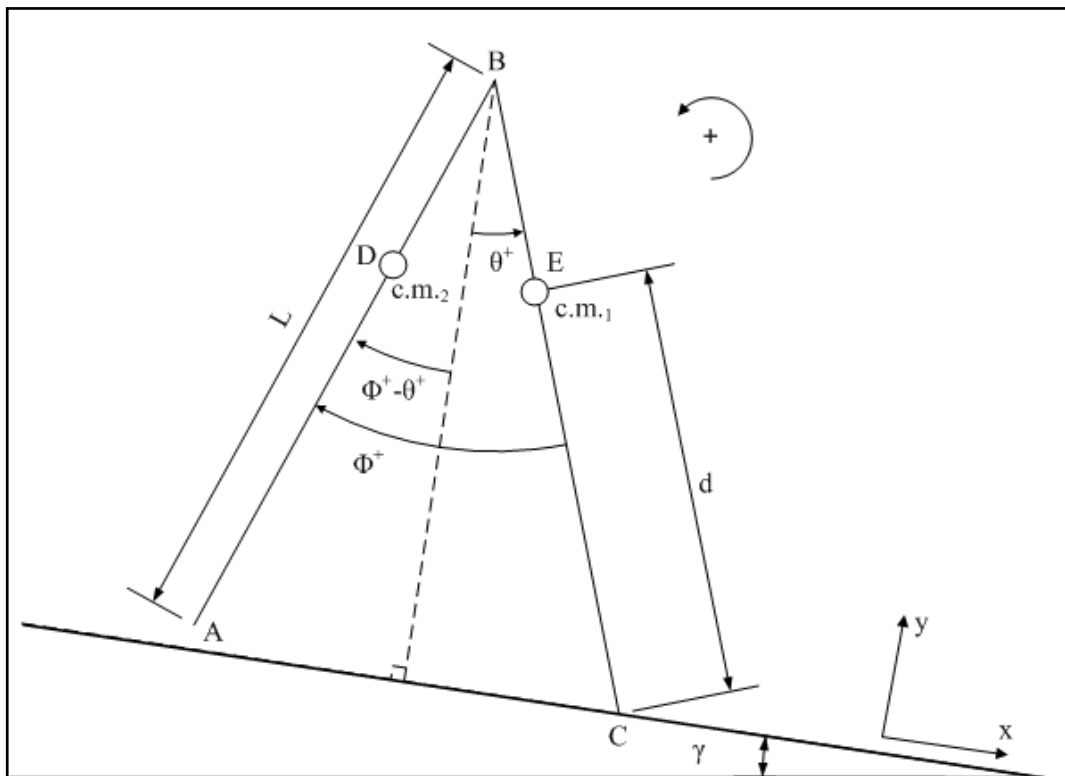


Figure 3.2 Simplest walker in after the collision configuration

At heelstrike, a collision occurs at point C. Some assumptions have been made to equate the angular momentum of the system before and after the heelstrike. The assumptions are always one point is in contact with the ground and the impulsive force is much larger than non-impulsive forces for example gravitational forces for the duration of the impact. With these two assumptions angular momentum about the impact site is conserved through the heelstrike collision. In Figure 3.2, point A at the end of the swing leg is in before the collision configuration and point C at the end of the stance leg is in after the collision configuration. In reality, the impact site remains at the same location, but due to the terminology that is being used in describing stance and swing legs, name for the impact site has changed (i.e. the leg that is called "swing" leg is renamed as the "stance" leg after the collision takes place). If we use a coordinate system which is tilted with the slope we can write the expressions for angular momentum of the walker both before and after the collision. Following equations give total angular momentum of the simplest walker after the collision about point C ( $H_C^+$ ).

$$\mathbf{H}_C^+ = \mathbf{r}_{E/C}^+ \times (m \mathbf{V}_E^+) + \mathbf{r}_{D/C}^+ \times (m \mathbf{V}_D^+) \quad (3.33)$$

$$\mathbf{r}_{E/C}^+ = [-d \sin(\theta^+)]\mathbf{i} + [d \cos(\theta^+)]\mathbf{j} \quad (3.34)$$

$$\mathbf{r}_{B/C}^+ = [-L \sin(\theta^+)]\mathbf{i} + [L \cos(\theta^+)]\mathbf{j} \quad (3.35)$$

$$\mathbf{r}_{D/B}^+ = [(L - d) \sin(\theta^+ - \phi^+)]\mathbf{i} + [-(L - d) \cos(\theta^+ - \phi^+)]\mathbf{j} \quad (3.36)$$

$$\mathbf{r}_{D/C}^+ = \mathbf{r}_{D/B}^+ + \mathbf{r}_{B/C}^+ \quad (3.37)$$

$$\mathbf{V}_E^+ = \frac{d}{dt} \mathbf{r}_{E/C}^+ \quad (3.38)$$

$$\mathbf{V}_D^+ = \frac{d}{dt} \mathbf{r}_{D/C}^+ \quad (3.39)$$

Angular momentum of link AB after the collision about point B is given by:

$$\mathbf{H}_B^+ = \mathbf{r}_{A/B}^+ \times (m \mathbf{V}_A^+) \quad (3.40)$$

$$\mathbf{r}_{B/C}^+ = [-L \sin(\theta^+)]\mathbf{i} + [L \cos(\theta^+)]\mathbf{j} \quad (3.41)$$

$$\mathbf{r}_{A/B}^+ = [L \sin(\theta^+ - \phi^+)]\mathbf{i} + [-L \cos(\theta^+ - \phi^+)]\mathbf{j} \quad (3.42)$$

$$\mathbf{r}_{A/C}^+ = \mathbf{r}_{B/C}^+ + \mathbf{r}_{A/B}^+ \quad (3.43)$$

$$\mathbf{V}_A^+ = \frac{d}{dt} \mathbf{r}_{A/C}^+ \quad (3.44)$$

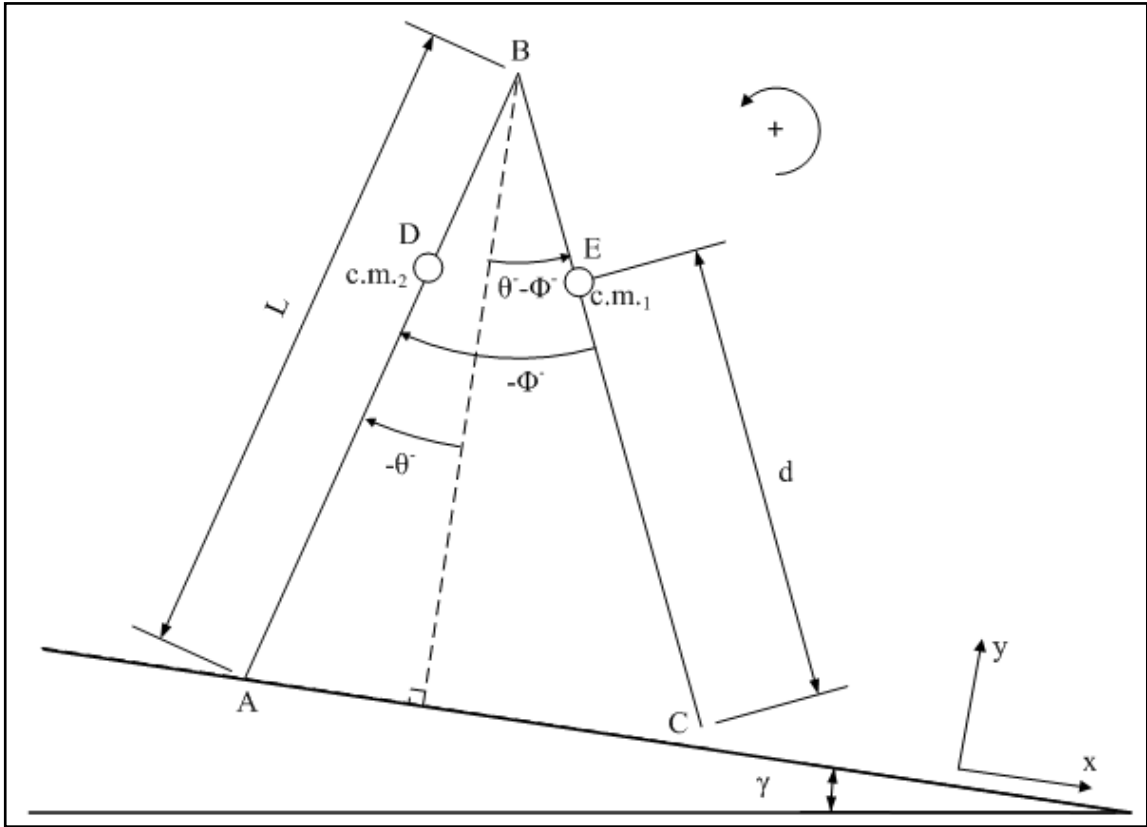


Figure 3.3 Simplest walker in before the collision configuration

Before collision configuration of the simplest walker is shown in Figure 3.3. Following equations give total angular momentum of the simplest walker before the collision about point C ( $\mathbf{H}_C^-$ ).

$$\mathbf{H}_C^- = \mathbf{r}_{D/C}^- \times (m \mathbf{V}_D^-) + \mathbf{r}_{E/C}^- \times (m \mathbf{V}_E^-) \quad (3.45)$$

$$\mathbf{r}_{B/C}^- = [-L \sin(\theta^- - \phi^-)] \mathbf{i} + [L \cos(\theta^- - \phi^-)] \mathbf{j} \quad (3.46)$$

$$\mathbf{r}_{E/C}^- = [-d \sin(\theta^- - \phi^-)] \mathbf{i} + [d \cos(\theta^- - \phi^-)] \mathbf{j} \quad (3.47)$$

$$\mathbf{r}_{D/B}^- = [-(L - d) \sin(-\theta^-)] \mathbf{i} + [-(L - d) \cos(-\theta^-)] \mathbf{j} \quad (3.48)$$

$$\mathbf{r}_{\bar{D}/C} = \mathbf{r}_{\bar{B}/C} + \mathbf{r}_{\bar{D}/B} \quad (3.49)$$

$$\mathbf{r}_{\bar{D}/A} = [-d \sin(\theta^-)]\mathbf{i} + [d \cos(\theta^-)]\mathbf{j} \quad (3.50)$$

$$\mathbf{r}_{\bar{B}/A} = [-L \sin(\theta^-)]\mathbf{i} + [L \cos(\theta^-)]\mathbf{j} \quad (3.51)$$

$$\mathbf{r}_{\bar{E}/B} = [(L - d) \sin(\theta^- - \phi^-)]\mathbf{i} + [-(L - d) \cos(\theta^- - \phi^-)]\mathbf{j} \quad (3.52)$$

$$\mathbf{r}_{\bar{E}/A} = \mathbf{r}_{\bar{E}/B} + \mathbf{r}_{\bar{B}/A} \quad (3.53)$$

$$\mathbf{V}_{\bar{E}} = \frac{d}{dt} \mathbf{r}_{\bar{E}/A} \quad (3.54)$$

$$\mathbf{V}_{\bar{D}} = \frac{d}{dt} \mathbf{r}_{\bar{D}/A} \quad (3.55)$$

Angular momentum of link AB before the collision about point B is given by:

$$\mathbf{H}_{\bar{B}} = \mathbf{r}_{\bar{A}/B} \times (m \mathbf{V}_{\bar{A}}) \quad (3.56)$$

$$\mathbf{r}_{\bar{A}/B} = [L \sin(\theta^-)]\mathbf{i} - [L \cos(\theta^-)]\mathbf{j} \quad (3.57)$$

$$\mathbf{r}_{\bar{D}/A} = [-d \sin(\theta^-)]\mathbf{i} + [d \cos(\theta^-)]\mathbf{j} \quad (3.58)$$

$$\mathbf{V}_{\bar{A}} = \frac{d}{dt} \mathbf{r}_{\bar{D}/A} \quad (3.59)$$

After all terms are computed, equations of heelstrike transitions can be built by equating angular momenta before and after the collision.

$$\mathbf{H}_B^+ = \mathbf{H}_B^- \quad (3.60)$$

$$L^2[\dot{\theta}^+(1 - \cos(\phi^+)) - \dot{\phi}^+] = d^2\dot{\theta}^- \quad (3.61)$$

$$\mathbf{H}_C^+ = \mathbf{H}_C^- \quad (3.62)$$

$$\begin{aligned} & 2\dot{\theta}^+[L^2(1 - \cos(\phi^+)) + d^2 + Ld(\cos(\phi^+) - 1)] \\ & + \dot{\phi}^+[-(L - d)^2 + L(L - d)\cos(\phi^+)] \\ & = d[2\dot{\theta}^-(d - L + L\cos(\phi^-)) + \dot{\phi}^-(L - d)] \end{aligned} \quad (3.63)$$

Equations of leg transition in matrix form are obtained.

$$\begin{bmatrix} L^2(1 - \cos(\phi^+)) & -L^2 \\ 2(L^2(1 - \cos(\phi^+)) + d^2 + Ld(\cos(\phi^+) - 1)) & (L - d)(L\cos(\phi^+) - L + d) \end{bmatrix} \quad (3.64)$$

$$\begin{bmatrix} \dot{\theta}^+ \\ \dot{\phi}^+ \end{bmatrix} = \begin{bmatrix} d^2 & 0 \\ 2d((d - L + L\cos(\phi^-)) & d(L - d) \end{bmatrix} \begin{bmatrix} \dot{\theta}^- \\ \dot{\phi}^- \end{bmatrix}$$

### 3.1.4. Numerical Solution Method with MATLAB

Now, we have 13 equations 2 from transition of heelstrike, 8 from equations of motion and 3 from geometry. To get results from this study, 13 equations with 13 unknowns must be solved. A numerical approach is considered in MATLAB by using the ‘‘Fsolve’’ function. A new angle configuration is defined as:

$$\theta_1 = \theta, \quad \dot{\theta}_1 = \dot{\theta} \quad (3.65)$$

$$\theta_2 = \pi - \phi, \quad \dot{\theta}_2 = -\dot{\phi} \quad (3.66)$$

Angular position and speed at initial ( $t = 0$ ) and final time ( $t = \tau$ ) for one step are obtained by using equations 3.67 to 3.70.

At  $t = 0$

$$\mathbf{y}(0) = \mathbf{y}^+ \quad (3.67)$$

$$\mathbf{y}^+ = \begin{bmatrix} \theta_1^+ \\ \dot{\theta}_1^+ \\ \theta_2^+ \\ \dot{\theta}_2^+ \end{bmatrix} = \begin{bmatrix} \gamma \\ 0 \\ \pi \\ 0 \end{bmatrix} + \sum_{i=1}^4 c_i \mathbf{x}^{(i)} \quad (3.68)$$

At  $t = \tau$

$$\mathbf{y}(\tau) = \mathbf{y}^- \quad (3.69)$$

$$\mathbf{y}^- = \begin{bmatrix} \theta_1^- \\ \dot{\theta}_1^- \\ \theta_2^- \\ \dot{\theta}_2^- \end{bmatrix} = \begin{bmatrix} \gamma \\ 0 \\ \pi \\ 0 \end{bmatrix} + \sum_{i=1}^4 c_i \mathbf{x}^{(i)} e^{\lambda_i \tau} \quad (3.70)$$

Three equations are obtained from geometry:

$$\theta_2^+ = \pi - 2\theta_1^+ \quad (3.71)$$

$$\theta_2^- = \pi - 2\theta_1^- \quad (3.72)$$

$$\theta_1^+ = -\theta_1^- \quad (3.73)$$

Rearrangements of two equations that are obtained from heelstrike transition are shown in Equations 3.74 to 3.76.



$$\mathbf{F}^+(\theta_1^+) \begin{bmatrix} \dot{\theta}_1 \\ \dot{\theta}_2 \end{bmatrix}^+ = \mathbf{F}^-(\theta_1^+) \begin{bmatrix} \dot{\theta}_1 \\ \dot{\theta}_2 \end{bmatrix}^- \quad (3.74)$$

$$\begin{bmatrix} \dot{\theta}_1 \\ \dot{\theta}_2 \end{bmatrix}^+ = \underbrace{(\mathbf{F}^+)^{-1}(\mathbf{F}^-)}_{\mathbf{K}(\theta_1^+)} \begin{bmatrix} \dot{\theta}_1 \\ \dot{\theta}_2 \end{bmatrix}^- \quad (3.75)$$

$$\begin{bmatrix} \dot{\theta}_1 \\ \dot{\theta}_2 \end{bmatrix}^+ = \mathbf{K}(\theta_1^+) \begin{bmatrix} \dot{\theta}_1 \\ \dot{\theta}_2 \end{bmatrix}^- \quad (3.76)$$

The unknowns are solved numerically to identify a fixed gait cycle.

### 3.1.5. Simplest Walker ADAMS Simulation and Comparison with MATLAB Results

The same geometry in the previous section is generated in the ADAMS multi-body dynamic simulation software. Simplest walker is modeled in ADAMS as shown in Figure 3.4. A frictionless revolute joint is used at the hip for the swing movement. Length of the legs is determined as 1 m, center of masses are lumped at a distance of 0.75 m from the feet and each leg has a mass of 0.5 kg. Point-to-plane contact is used and planes are separated, so the swing foot can pass through the ramp surface when the stance leg is near vertical. Ground surface has a fixed slope of 0.025 radians. Inertia of the legs is set to  $10^{-6}$  kg.m<sup>2</sup> to compensate the inertial forces. Stable initial conditions are used. Figure 3.4 shows the model of the simplest model in ADAMS simulation environment. An artificial joint is obtained by using a script that uses a sensor and measures the force in the foot contact. When initial swing leg becomes the stance leg, the sensor triggers and script command returns to the script and the script deactivates the revolute joint. A superimposed image of the simplest walker gait in ADAMS is shown in Figure 3.5.

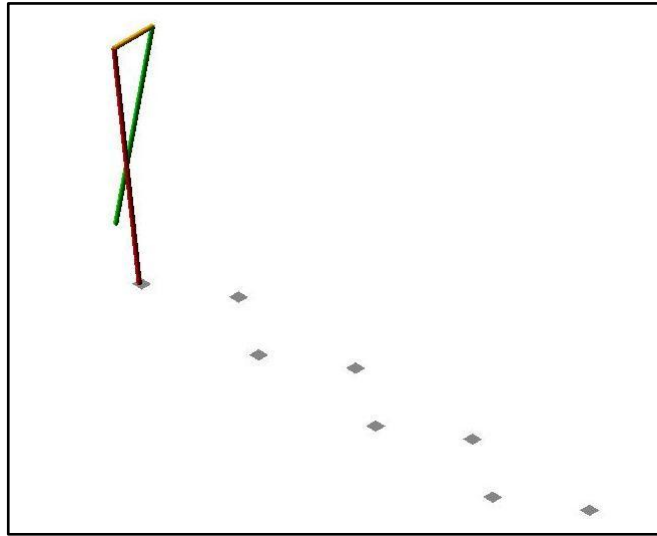


Figure 3.4 Simplest walker model in ADAMS software

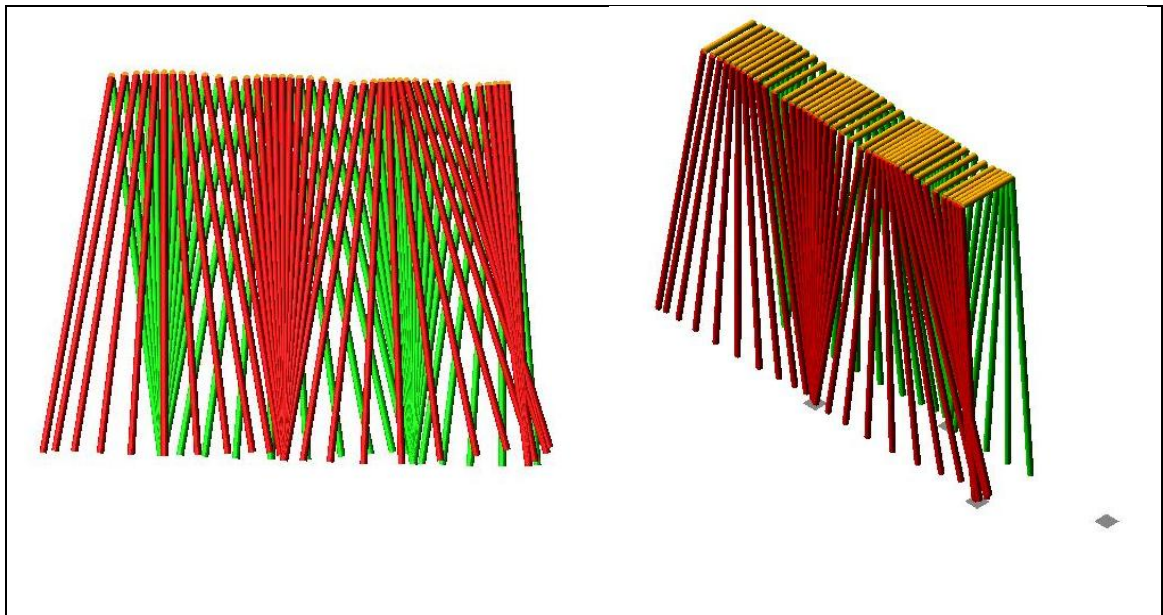


Figure 3.5 Superimposed gait images for the simplest walker model in ADAMS software

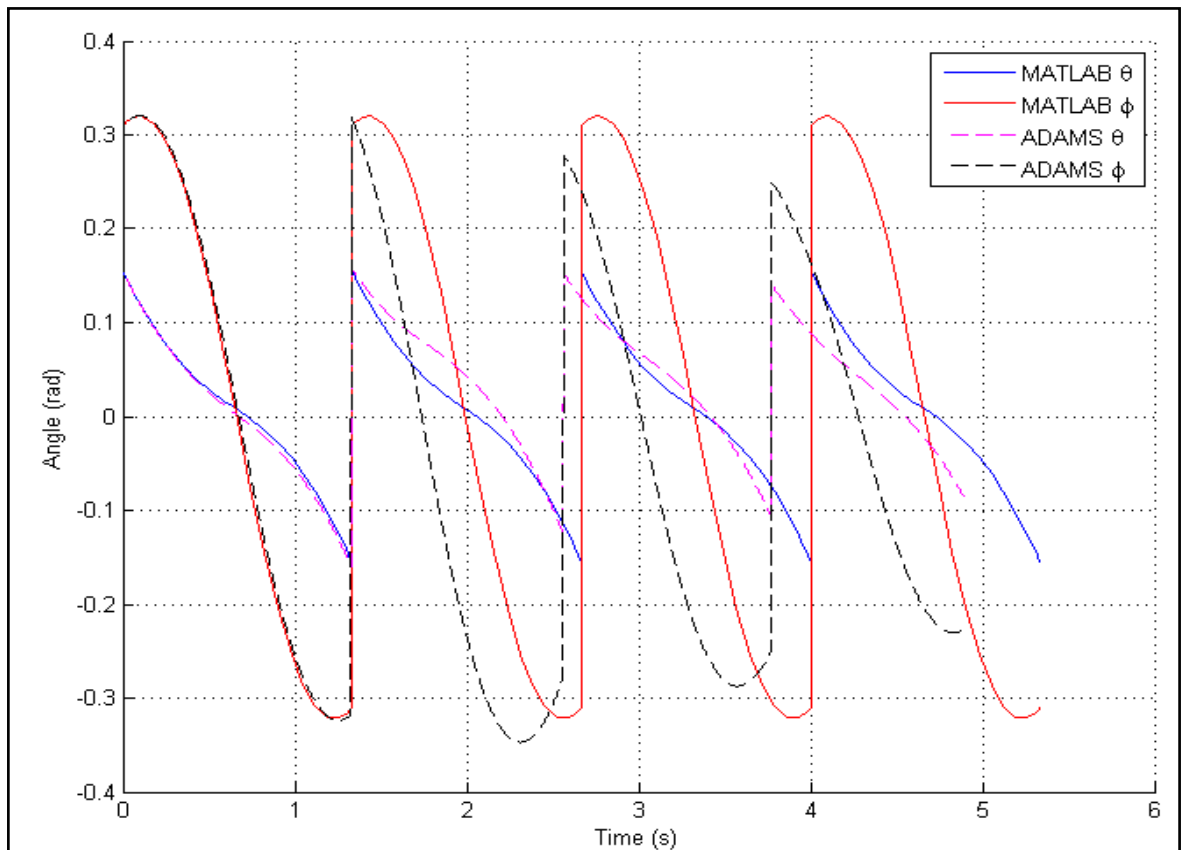


Figure 3.6 MATLAB and ADAMS simulation results for the simplest walker

Figure 3.6 MATLAB and ADAMS simulation results for the simplest walker shows the change of the generalized coordinate angles  $\theta$  and  $\Phi$ , in MATLAB and ADAMS software. Although results are generally similar, after the collision, the assumption that is being made in MATLAB simulation model becomes invalid in the ADAMS model. Average speed of the ADAMS simulation is 0.19 m/s for 4 seconds and average speed of the MATLAB simulation is 0.24 m/s for 4 seconds. While change of the  $\theta$  and  $\Phi$  is similar for the first step, after first collision ADAMS simulation results differentiates from MATLAB results. The main reason of this differentiation is two different collision models. While a more realistic impact-friction based collision model is used in ADAMS, a transition rule is applied in collision in MATLAB. As the real environment, amplitude of the of the angles are decreasing due to the energy loses in collision in ADAMS and simplest walker is going to fall in the end, on the other hand, in MATLAB simulation the system is going to reach its optimum angular tractories.

## **3.2. PARAMETRIC ANALYSIS OF A GENERIC PLANAR BIPED MODEL DRIVEN BY ANTHROPOMORPHIC GAIT DATA**

An actuated bipedal robot with torso is modeled by using the ADAMS simulation software for different heights and materials. Required torque and power consumption values are calculated for six actuators (2 hip, 2 knee, 2 ankle) of the bipedal robot for 5 different walking speeds, for steel, carbon fiber, and aluminum materials and for 3 different heights.

### **3.2.1. Parameterization**

A parametric ADAMS model has been built at human anthropomorphic dimensions [32] for 1.50, 1.75 and 2.00 meters tall human. This study has been performed within the scope of a research project entitled “Biomimetic Biped Walking Robot”. Therefore the design was focused on the biomimetic properties of the robot. The anthropomorphic proportions are shown in Figure 3.7. The length of the foot (from heel to toe) will be 15.2% of the height. Segment lengths are given as fractions of the total height. Steel and aluminum are selected as structural materials. In each case, mass distribution is computed for different geometry and material types. ADAMS software can define parameters by using a tool called design variable. Design variable is used for the parameterization by creating segment lengths that are proportional to the height of the reference human body. Total mass is calculated according to the selected material and height of the bipedal robot, as shown in Table 3.1. In this calculation, the total masses of only the structural components are included.

This study provides the criteria for selecting the actuators. Moment and power consumption table (Table 3.2) summarizes the actuators continuous loading capacity requirements.

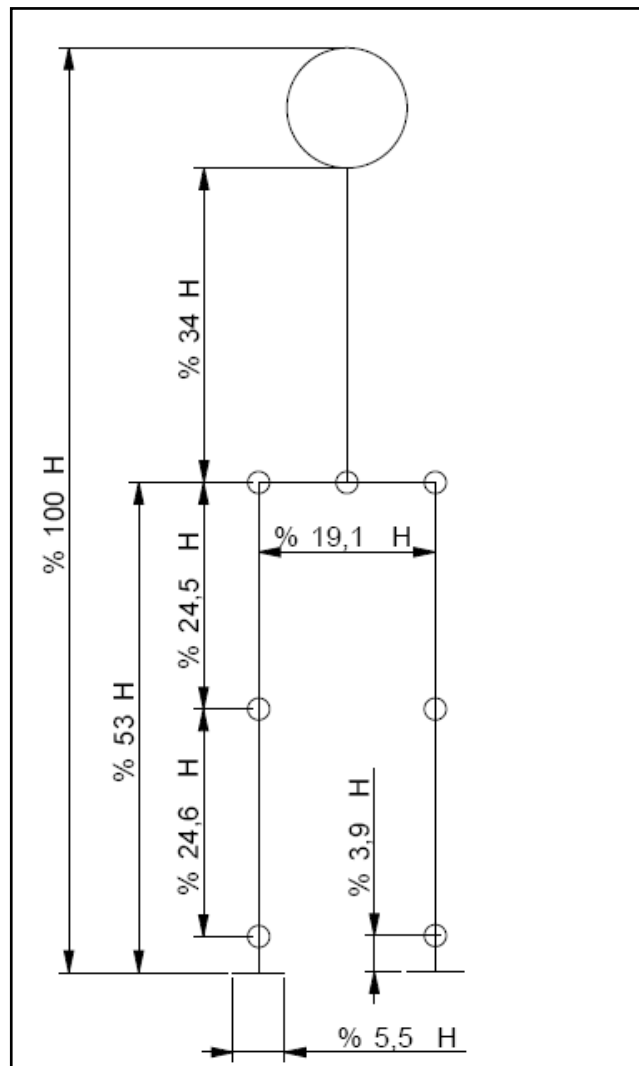


Figure 3.7 Human segment length proportions with respect to the total height [32]

Table 3.1 Total robot mass for different heights and materials

Material	H (m)	Mass (kg)
Steel	1.50	14.50
Steel	1.75	17.82
Steel	2.00	21.51
Aluminum	1.50	4.96
Aluminum	1.75	6.24
Aluminum	2.00	7.57
RTP Carbon	1.75	3.11

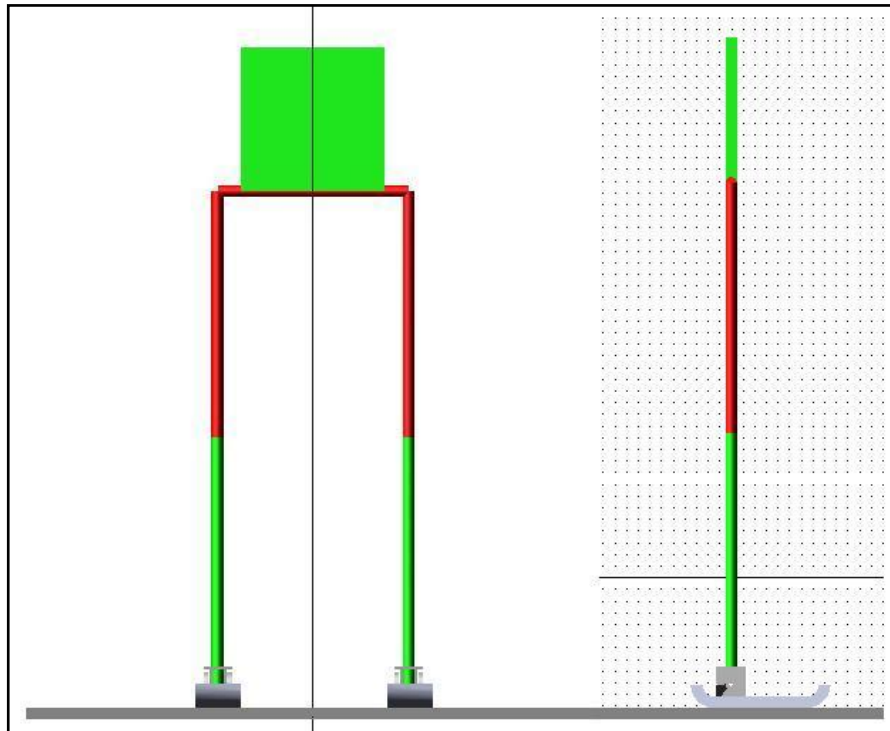


Figure 3.8 Front and side view of the anthropomorphic parametric ADAMS model

### 3.2.2. Anthropomorphic Gait Data

Actuators are driven by the joint angular position values during the gait cycle. These angular position values are taken from a reference human gait [32]. Three cubic splines are used on hip, knee and ankle joints to form a gait cycle. Stance and swing leg movements are generated by using the same splines with a 50 percent phase difference. These values are obtained from a reference natural human gait by using optical measurement techniques and a motion analysis software. Anthropomorphic angular position values for one and a half step are shown in Figure 3.9. In posture and gait analysis, joint angles are used to track the location and orientation of the body parts. Gait analysis is also used in sports to optimize the athletic performance or to identify motions that may cause injury or strain.

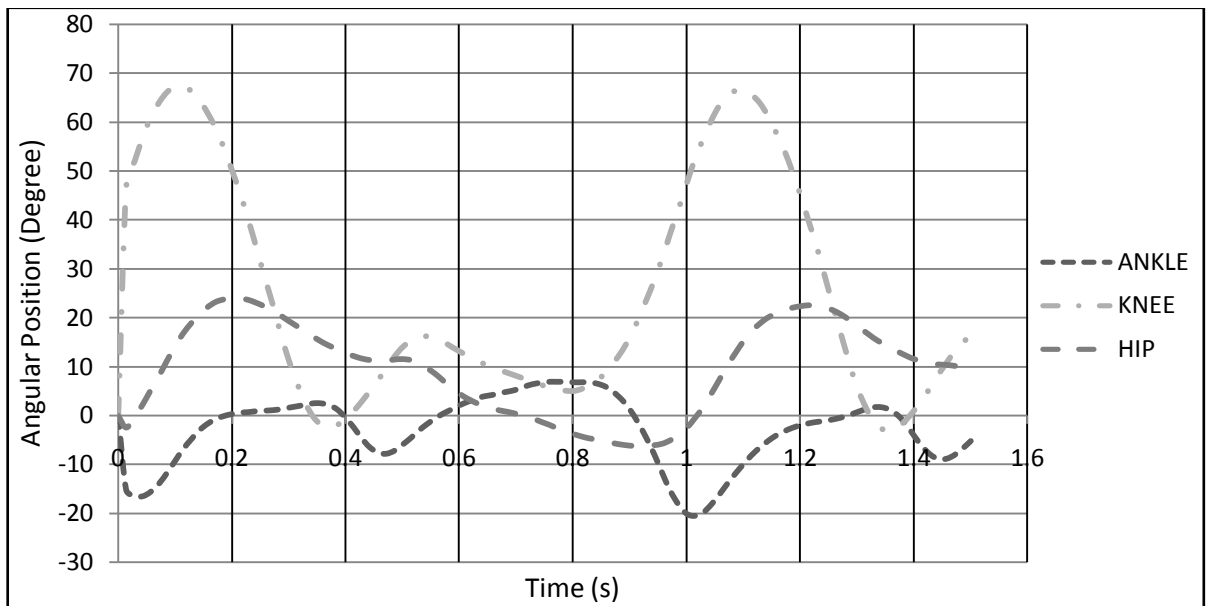


Figure 3.9 Anthropomorphic gait data in angular position form for each joint

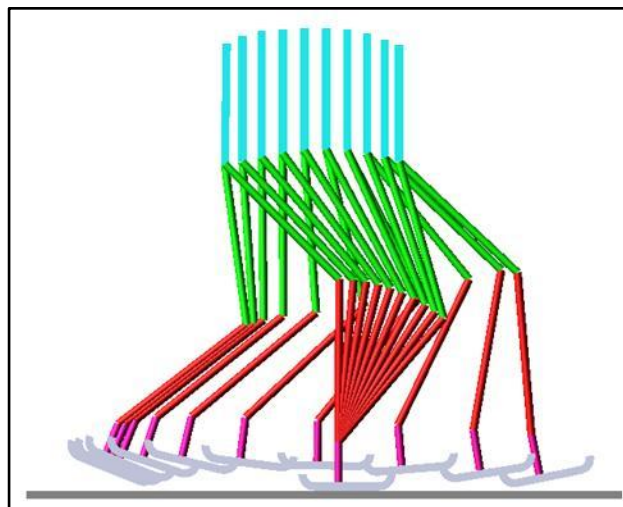


Figure 3.10 Superimposed view of the anthropomorphic model in ADAMS simulation for one step

An ADAMS model is created by fixing the stance foot of the robot to the ground (see Figure 3.10). Thus, a manipulator like mechanism is obtained. Anthropomorphic gait is applied to each joint for a single support phase of one step. Power and torque values are calculated for each joint. But only stance leg joint values are taken into account due to their significantly higher values compared to the swing leg joint values.

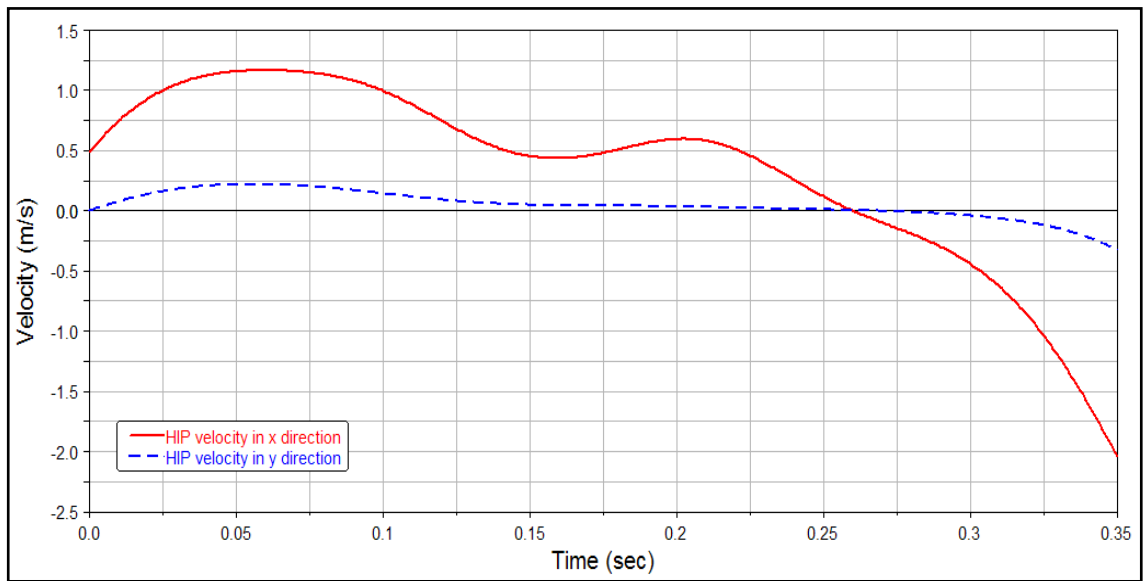


Figure 3.11 Hip velocity along x and y cartesian coordinates

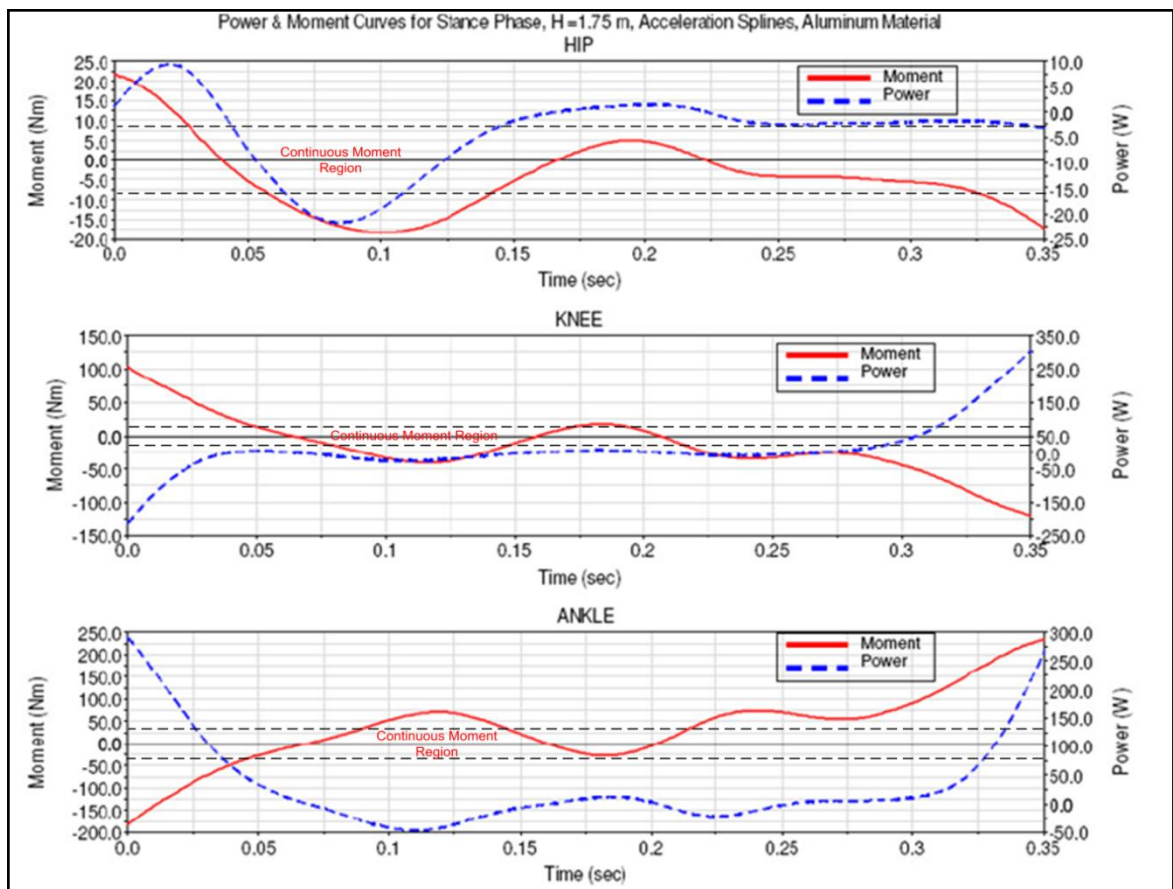


Figure 3.12 Torque and power diagrams based on anthropomorphic angular acceleration splines applied to the ADAMS model



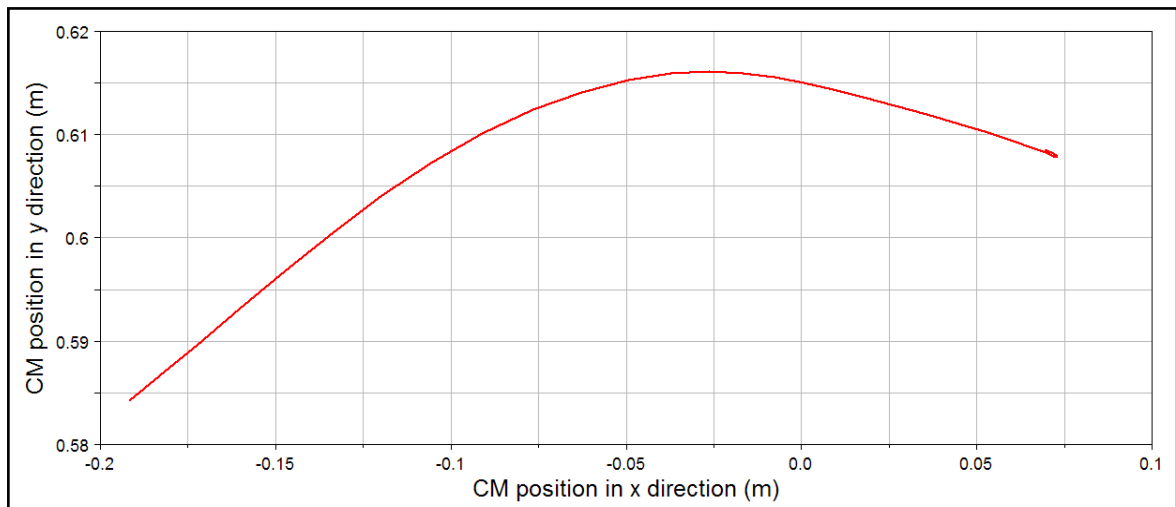


Figure 3.13 Trajectory of center of mass in cartesian coordinates

In Figure 3.11 velocity of the hip joint in x and y direction is showed. Average human walking speed is 1.3 m/s. The end of the velocity graph is sloped downwards because the stance foot is fixed to the ground. ADAMS software has a cubic spline generator that is used for combining data points. Angular acceleration values have been used to obtain reliable results. ADAMS created cubic splines by using given initial angular velocity and position values. Human gait data in angular joint acceleration form is imported to ADAMS and angular acceleration splines are generated for hip, knee, and ankle joints. These splines are implemented to joints as motion functions and a one step simulation is run to obtain necessary torques and power values for humanlike walking. In Figure 3.12 graphs of the torque and power requirements in the joints are showed. Horizontal dashed lines in the middle of the graphs refer to the continuous torque region of the purchased motor and gearhead couple.

Center of mass location of the model in standing configuration is 0.6 m above from the ground. Figure 3.13 shows the change of center of mass position in x and y coordinates in one step for 1.75 m height human proportion model.

In Table 3.2 root mean square (RMS) joint power and torque values are listed. Sample 7 and 8 are simulations that are created with human angular acceleration values instead of human angular position values. Significant drop down on the values by using

angular acceleration values can be seen if sample 8 is compared with sample 5. By the help of parameterized simulations, sample 7 is chosen as a guide to selection of actuation components. 100 W brushless servo motors and aluminum structural materials are selected in the light of this study.

Table 3.2 Joint power and torque values (RMS) for one step with several heights and materials

Sample	Material	H (m)	STANCE					
			Hip		Knee		Ankle	
			M (N.m)	P (W)	M (N.m)	P (W)	M (N.m)	P (W)
1	Steel	1.5	33.5	32.2	87.1	105.4	163.9	145.4
2	Steel	1.75	50.5	47.8	156.2	191.2	292.6	260.5
3	Steel	2	75.0	69.6	260.8	321.5	485.2	433.6
4	Aluminum	1.5	11.7	11.3	30.6	37.0	57.6	51.1
5	Aluminum	1.75	17.7	16.8	54.9	67.2	102.7	91.5
6	Aluminum	2	26.3	24.4	91.6	112.9	170.4	152.3
7(accel.)	Aluminum	1.75	10.1	8.5	44.8	73.2	86.4	80.1
8(accel.)	Carbon-fiber	1.75	5.0	4.2	22.2	36.4	42.9	39.8
Sample	Material	H (m)	SWING					
1	Steel	1.5	28.8	59.6	15.7	71.7	1.3	2.4
2	Steel	1.75	39.8	81.3	21.4	97.5	1.4	2.5
3	Steel	2	53.2	107.1	28.2	128.2	1.5	2.7
4	Aluminum	1.5	10.1	20.9	5.5	25.1	0.4	0.8
5	Aluminum	1.75	14.0	28.5	7.5	34.2	0.5	0.9
6	Aluminum	2	18.7	37.6	9.9	45.0	0.5	0.9
7(accel.)	Aluminum	1.75	7.2	20.2	4.5	14.5	0.3	0.7
8(accel.)	Carbon-fiber	1.75	3.6	10.0	2.2	7.2	0.2	0.3

### 3.3. KINEMATICS OF BIPED WALKING

Biped robots have better mobility than conventional wheeled robots, but tipping them over is also easier compared to other kinds. To be able to maintain stability in various environments, rough terrains, slopes, regions containing obstacles, it is necessary that the robot be adaptable to the ground conditions.

A gait trajectory is generated by using MATLAB, with an approach given in the literature [13]. First, hip and ankle trajectories in cartesian coordinates are generated with

cubic splines by using a few characteristic via points. These characteristic via points and initial phase of tracing the path for the generation of a simple walking trajectory are shown in Figure 3.14. Planar seven-link model is utilized (see Figure 3.14) with link offsets, locations of link centroids and angular position values determining the system's relation with the environment. End of the double support phase configuration is represented on the left side of the figure. Right side of the figure represents the beginning of the double support phase. Projection of the foot and hip trajectory in the single support phase can also be seen in this figure.

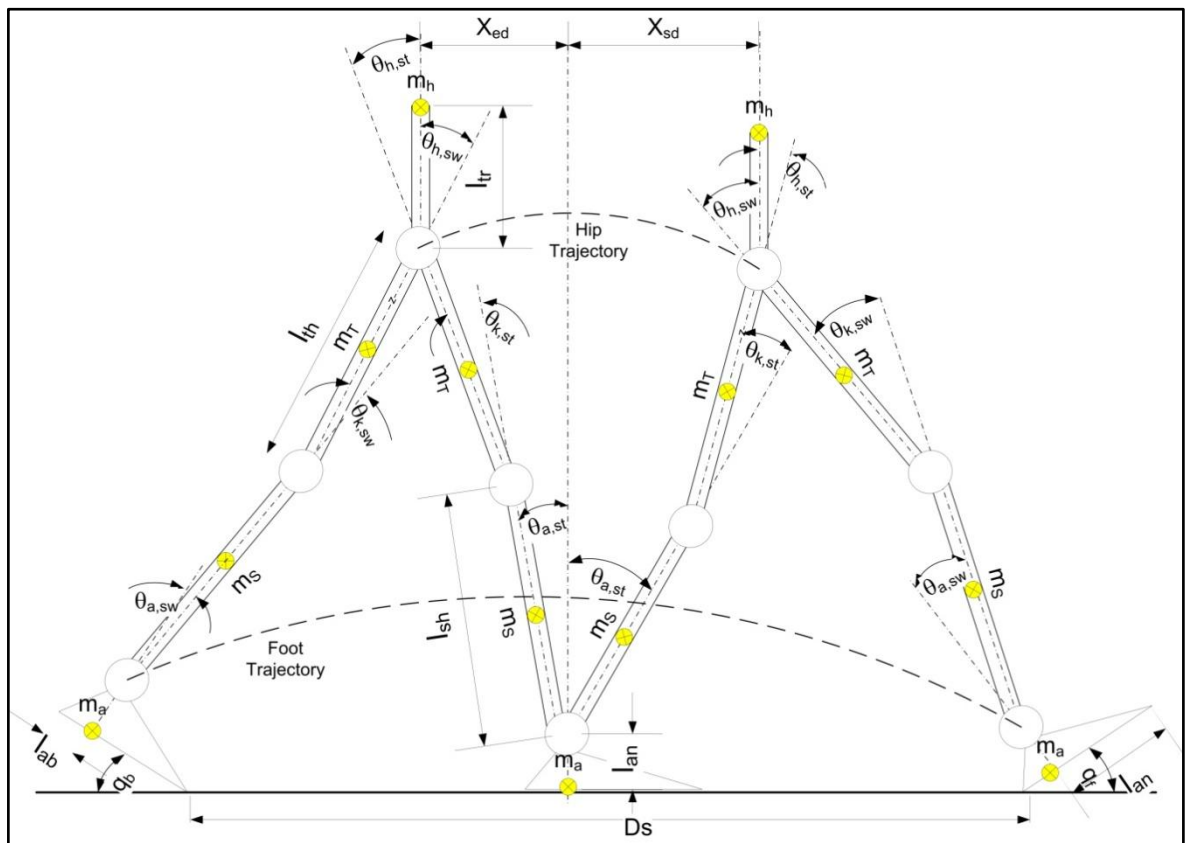


Figure 3.14 Model and gait parameters of the seven-link planar biped robot

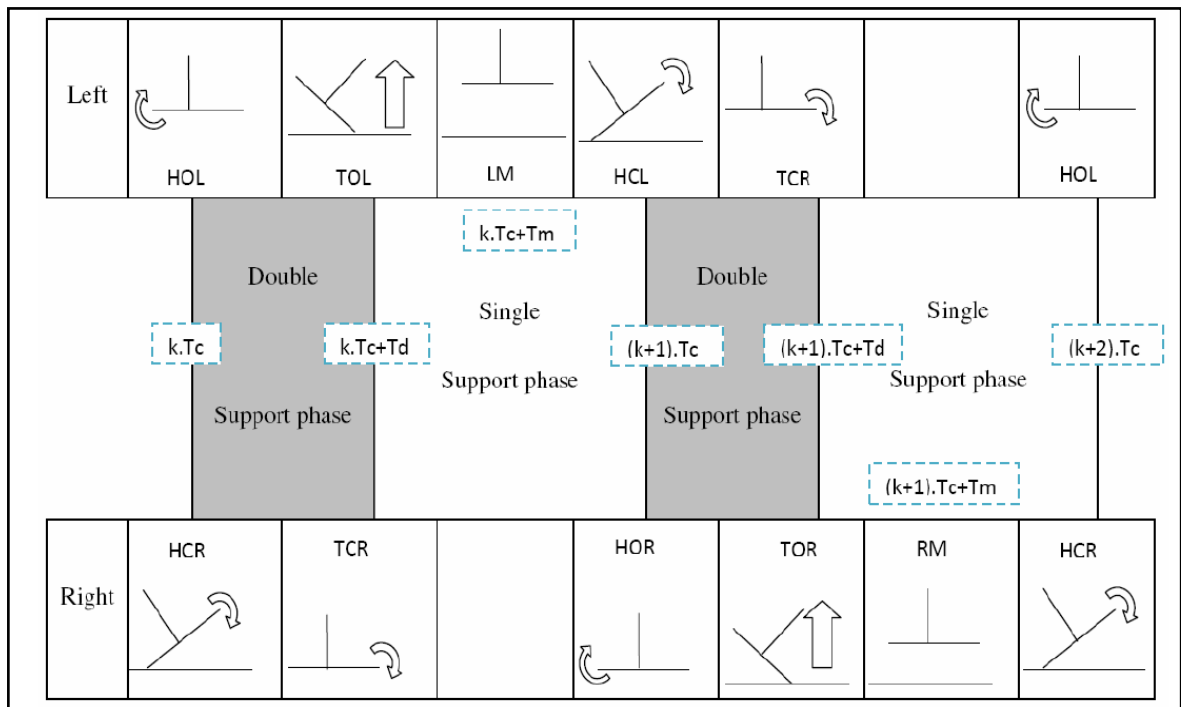


Figure 3.15 Characteristic behavior and phases of the left and right feet in one period of the gait cycle

A MATLAB m-file is written that creates a cubic spline by the predetermined via points from the characteristics of walking. The synchronization of the left and right feet is described and the characteristic via points of the foot trajectory and their timings are detailed in Figure 3.15. One period of the walking cycle is shown in this figure. Here,  $k$  is the step number.  $T_c$  is the sum of the single support and double support phases and  $2 T_c$  is one period of the cycle.  $T_d$  is time of the double support phase and  $T_m$  is the time of middle of the single support period. Walking pattern starts with double support and initially the right foot is the support foot until next double support phase. The meanings of capital letters are H: heel, T: toe, O: off, C: contact, M: max, L: left, R: right.

The significant via points for generating the gait are the ankle and hip positions. Table 3.3 shows the via point descriptions for cubic splines in order to time.  $q_b$  and  $q_f$  are the designated slope angles of the feet as it leaves and lands on the ground.  $q_{gs}$  and  $q_{ge}$  are slope of the ground, in this case both of them are zero. Letting  $H_{gs}$  and  $H_{ge}$  be the heights of the ground which is under the support foot, particularly they are zero on level ground.  $L_{a0}$  and  $H_{a0}$  are the coordinates of the highest point of swing foots ankle joint.  $D_s$  is the step

length. The link lengths  $l_{an}$ ,  $l_{af}$ ,  $l_{ab}$ ,  $l_{sh}$ ,  $l_{th}$  and  $l_{tr}$  are described in Figure 3.14.  $H_{max}$  and  $H_{min}$  are the highest and lowest vertical hip positions. The distance of along the x-axis from hip to the ankle of the support foot at the start and end of the single support phase and are denoted as  $x_{sd}$  and  $x_{ed}$ , which are shown in Figure 3.15. Absolute angle of the torso  $q_h$  is considered vertical with respect to the ground.

Table 3.3 Characteristic via points for cubic splines of foot and ankle trajectories

	$k.T_c$	$k.T_c+T_d$	$k.T_c+T_m$	$(k+1)T_c$	$(k+1)T_c+T_d$	$(k+2).T_c$
$x_a$	$k.D_s$	$k.D_s + l_{an} \cdot \sin(q_b) + l_{af} \cdot [1 + \cos(q_b)]$	$k.D_s + L_{ao}$	$(k+2).D_s - l_{an} \cdot \sin(q_f) - l_{ab} \cdot [1 + \cos(q_f)]$	$(k+2).D_s$	
$z_a$	$h_{gs} + l_{an}$	$H_{gs} + l_{af} \cdot \sin(-q_b) + l_{an} \cdot \cos(-q_b)$	$H_{ao}$	$H_{ge} + l_{ab} \cdot \sin(q_f) + l_{an} \cdot \cos(q_f)$	$h_{ge} + l_{an}$	
$q_a$	$q_{gs}$	$q_b$		$q_f$	$q_{ge}$	
$x_h$	$k.D_s + x_{sd}$	$k.D_s + x_{ed}$		$(k+1).D_s + x_{sd}$	$(k+1).D_s + x_{ed}$	$(k+2).D_s + x_{sd}$
$q_h$	$\pi/2$	$\pi/2$	$\pi/2$	$\pi/2$	$\pi/2$	$\pi/2$
$z_h$	$H_{min}$	$H_{max}$		$H_{min}$	$H_{max}$	$H_{min}$

After splines are generated for ankle and hip trajectories with respect to via points, it is time to find x and y coordinates of the knee joint. While, link lengths of thigh and shank and x, y coordinates of hip and ankle are known, two results are obtained for the coordinates of knee joint. The source of two solutions (see Figure 3.16) is the intersections of two circles, as the link lengths are considered to be radius of these circles. Only one of the solutions is possible due to physical limits of the knee joint. Thus, the solution that shows the knee to be bent forwards is chosen.

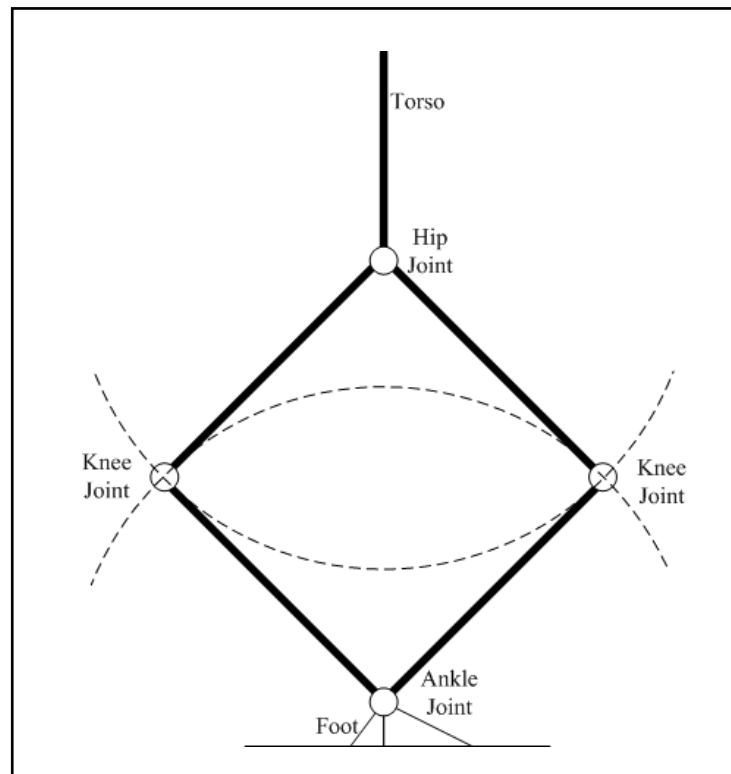


Figure 3.16 Two kinematics results of the knee joint

The 2-D stick diagram in Figure 3.17 of the robot is plotted by a MATLAB function. All of the cartesian coordinates of joints and link lengths are sent by wrapper function to drawstick diagram to plot a stick animation. In Figure 3.17 a generic robot gait is shown.

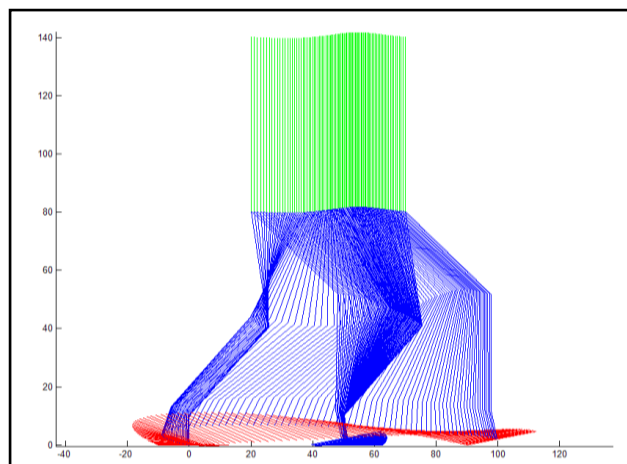


Figure 3.17 Walking pattern of general seven link biped robot for one step

### 3.4. ADAMS MODEL OF THE MANUFACTURED ROBOT

Robot parts designed in 1:1 scale (as detailed in Chapter 4) in Pro/E Wildfire are imported to ADAMS software as parasolid files. When the material properties are assigned, ADAMS automatically handled calculation of center of mass and inertia tensors for each part. These are assembled together by using fix and revolute joints at assigned joint coordinates (see Figure 3.18). Parts like bearings, sensors and gussets that are not significant compared to other parts are removed from the assembly to reduce the complexity of the model. The completed multi-body dynamic model is used to obtain essential data such as center of mass location and the total mass. Total mass of the model is 18.32 kg. The revolute motors (provided by ADAMS) mounted at the revolute joints are used for active position control of the joints and the angular displacements are assigned in the form of cubic spline functions for each joint. The generated planar biped robot model has 87 moving parts, 6 revolute joints, 80 fixed joints, 6 revolute motors and 3 degrees of freedom in its sagittal plane.

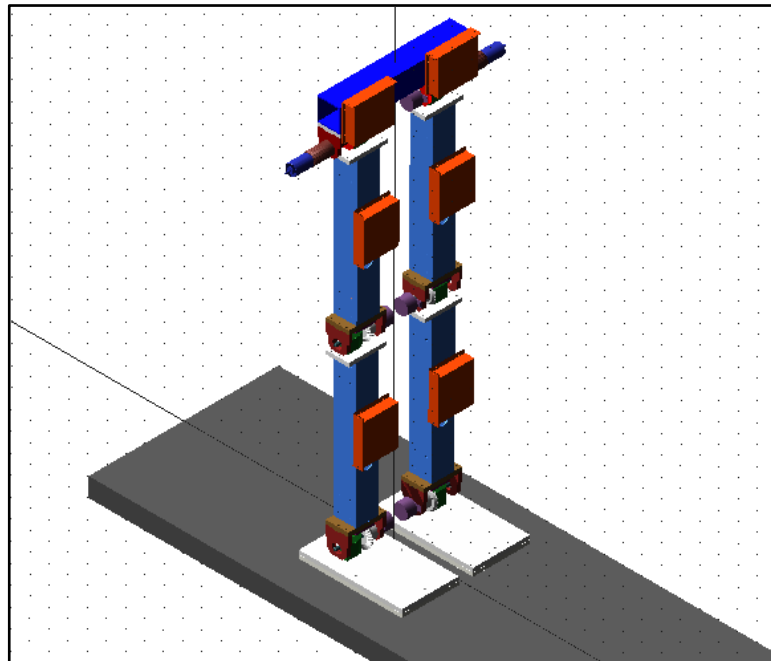


Figure 3.18 ADAMS assembly of the imported CAD models

All link length measurements are taken from Pro/E CAD software and implemented to the gait generator function in MATLAB. Gait parameters and link lengths explained in section 3.3 are shown in Table 3.4 and Table 3.5 .

Table 3.4 Link length parameters in mm of manufactured robot

	$l_{an}$	$l_{tr}$	$l_{af}$	$l_{ab}$	$l_{sh}$	$l_{th}$
<b>Link Lengths in mm</b>	60	104	175	65	460	465

Table 3.5 Gait parameters in mm of manufactured robot

	$q_b$ (rad)	$q_f$ (rad)	$L_{ao}$ (mm)	$H_{ao}$ (mm)	$H_{max}$ (mm)	$H_{min}$ (mm)	$x_{sd}$ (mm)	$x_{ed}$ (mm)	$D_s$ (mm)	$T_c$ (s)	$T_d$ (s)	$T_m$ (s)
<b>Gait 1</b>	-0.4	0.2	250	160	900	890	340	160	500	0.9	0.3	0.5
<b>Gait 2</b>	0	0	250	160	900	890	340	160	500	0.9	0.3	0.5

Parameters are entered to the gait generator and two different gaits are obtained. These gait trajectories are in the form of cubic splines, which is shown in Figure 3.20 and Figure 3.25. Time and angle samples are gathered for every 0.1 s in vector form from these splines. The time and angle samples are imported to the ADAMS and cubic splines are generated again. Then, cubic splines are applied to each joint.

Contacts are created at four corners of each foot where FSR's are mounted. Using contacts has upfront advantage that can be go beyond just modeling how parts meet at points and model how solid bodies react when they come in contact with one another when the model is in motion. Two types of contact models can be created in ADAMS: restitution and impact model. In order to get realistic results, impact model and coulomb friction model are chosen. Proper stiffness and damping values that are found by tuning method are entered. These are 10000 N/m for stiffness and 1000 N.s/m for damping. Solid to solid



contact is chosen that has an algorithm which is explained in ADAMS help as “To greatly simplify the contact detection algorithm, Adams/Solver assumes that the volume of intersection between two solids will be much, much less than the volume of either solid. After contact occurs between two solids, Adams/Solver computes the volumes of intersection. There may be only one volume of intersection, or there may be multiple volumes of intersection (this would correspond to multiple locations of contact). In this discussion, we assume that there is only a single volume of intersection. The algorithm is the same for every intersection volume. Once there is contact, Adams/Solver finds the centroid of the intersection volume. This is the same as the center of mass of the intersection volume (assuming the intersection volume has uniform density). Next, Adams/Solver finds the closest point on each solid to the centroid. The distance between these two points is the penetration depth.” Equation 5.1 shows how ADAMS calculates the contact forces without damping and friction feature.  $F$  is the contact force,  $d$  is the penetration depth which is selected as 0.1 mm and  $n$  is the force exponent which is selected as 2.2.

$$F = K \cdot d^n \quad (3.77)$$

On the friction side of the contact, coulomb friction model is used. Static and dynamic friction coefficients are found from material contact properties table in ADAMS help. From material contact properties table, dry rubber and dry steel have a static friction coefficient of 0.8 and dynamic friction coefficient of 0.76. Friction transition velocity is given as 1 m/s. ADAMS/Solver gradually adjusts the coefficient of friction from the value for static coefficient to the value for dynamic coefficient as the slip velocity at the contact point increases. When the slip velocity is equal to the value specified for friction transition velocity, the effective coefficient of friction is set to the dynamic coefficient.

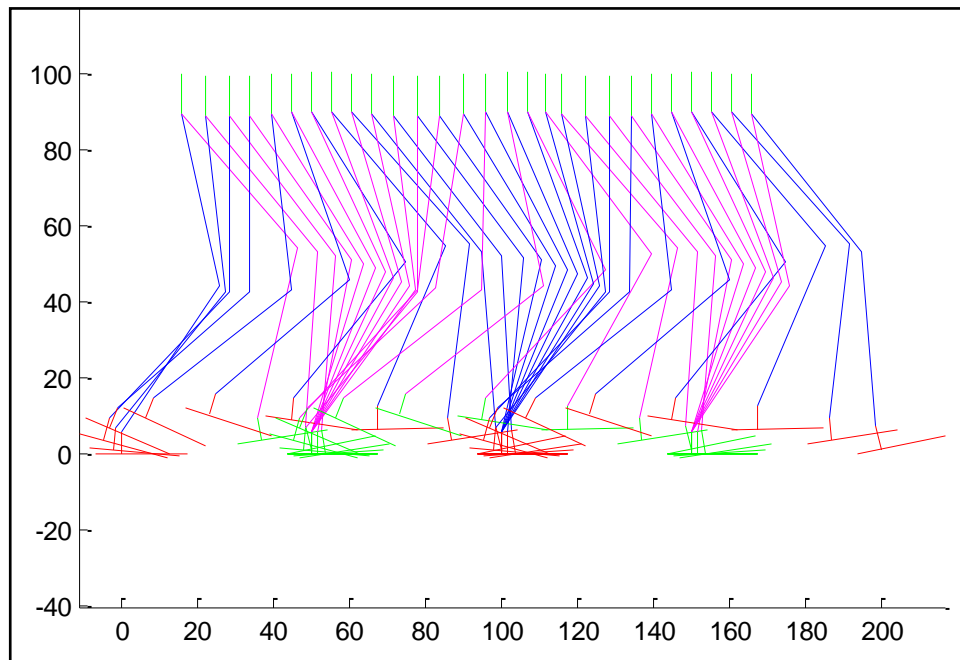


Figure 3.19 Walking pattern of prototyped biped robot for two steps of gait 1

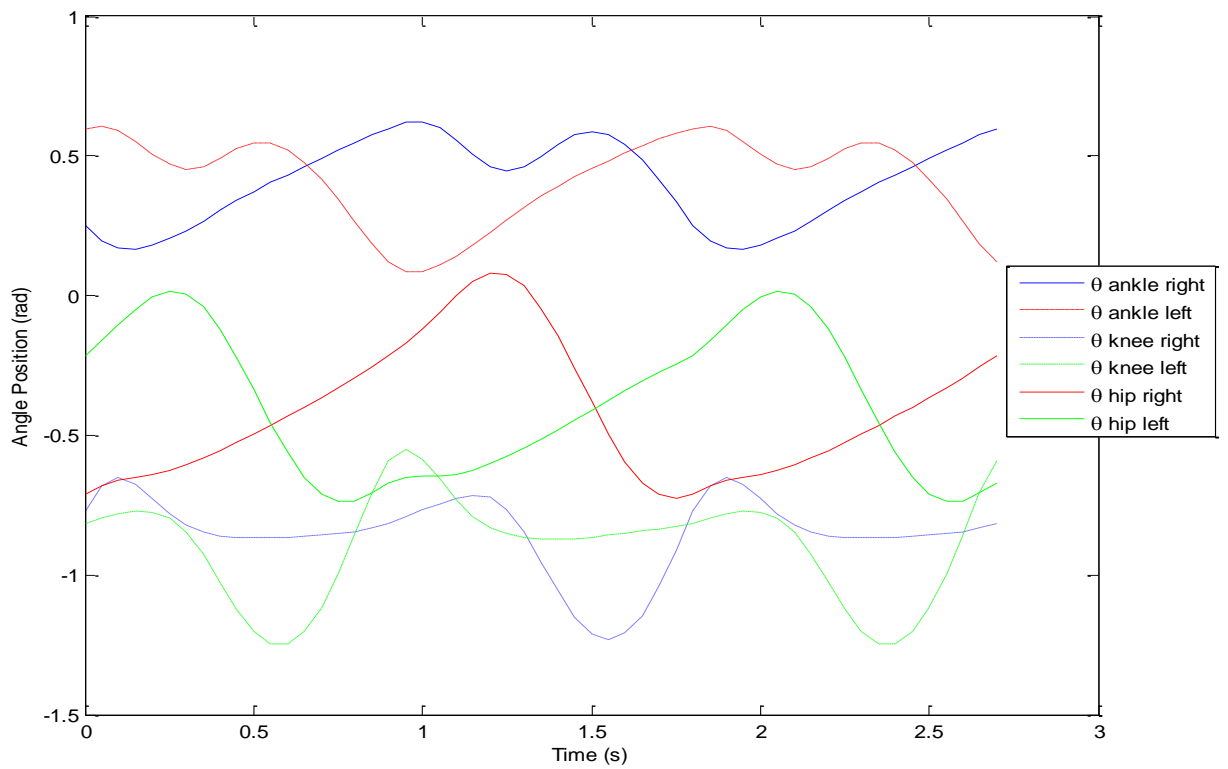


Figure 3.20 Joint angle position splines for two steps of gait 1

In Figure 3.19 and Figure 3.24 stick diagrams of both gaits are shown. These stick diagrams are outputs of the MATLAB gait generation program. As seen in the figures and also in Table 3.5 the difference between two gaits is  $q_b$  and  $q_f$  angles, which are the designated slope angles of the feet as it leaves and lands on the ground. Figure 3.20 and Figure 3.25 shows the generated angular trajectories that applied to each joint of the robot for gait 1 and gait 2.

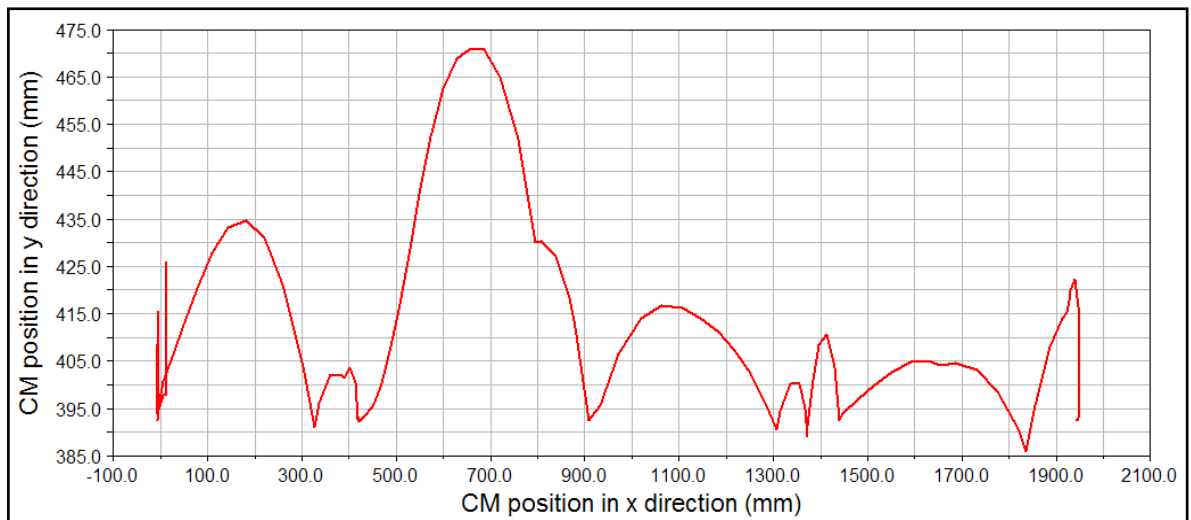


Figure 3.21 Center of mass location in x and y coordinates for gait 1

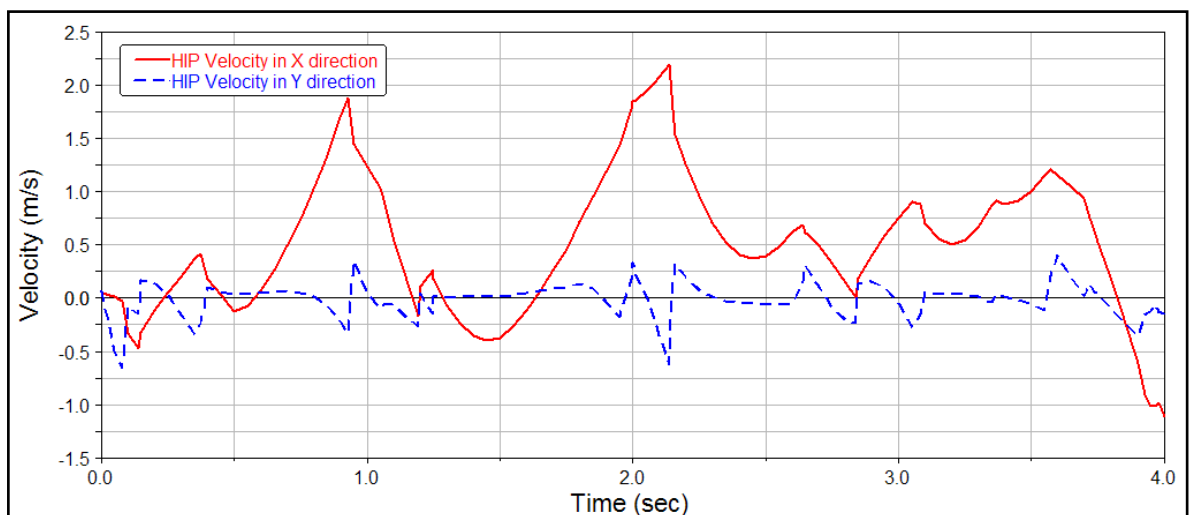


Figure 3.22 Velocity of the hip joint in x and y direction for gait 1

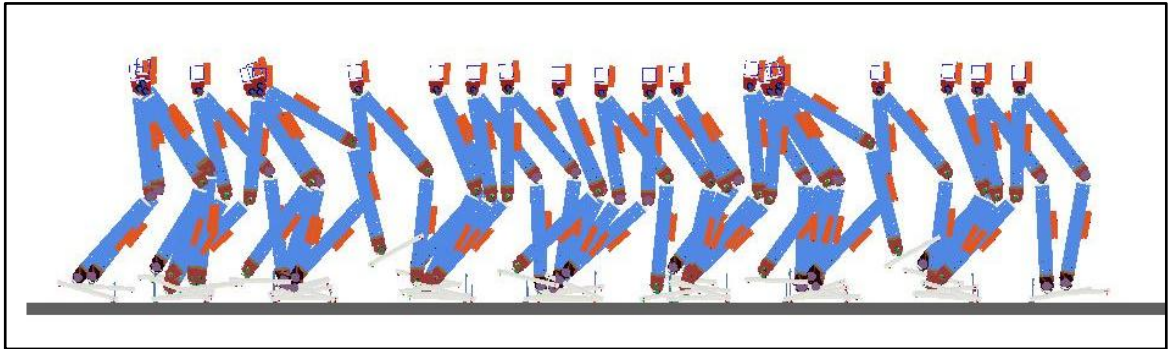


Figure 3.23 ADAMS simulation for gait 1 showing superimposed images in every 0.3 s (total of 6.6 s)

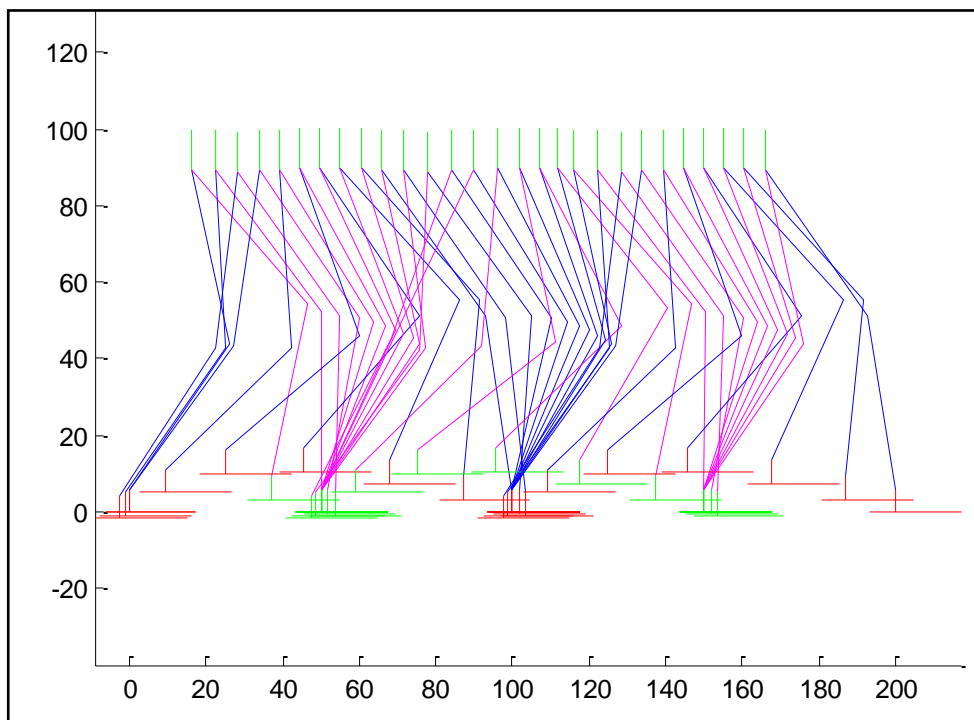


Figure 3.24 Walking pattern of the prototyped biped robot for two steps of gait 2

Velocity of the hip joint in x and y direction is showed in Figure 3.22 and Figure 3.29 for gait 1 and gait 2. Average speeds of gait 1 and gait 2 are 0.53 m/s and 0.58 m/s.

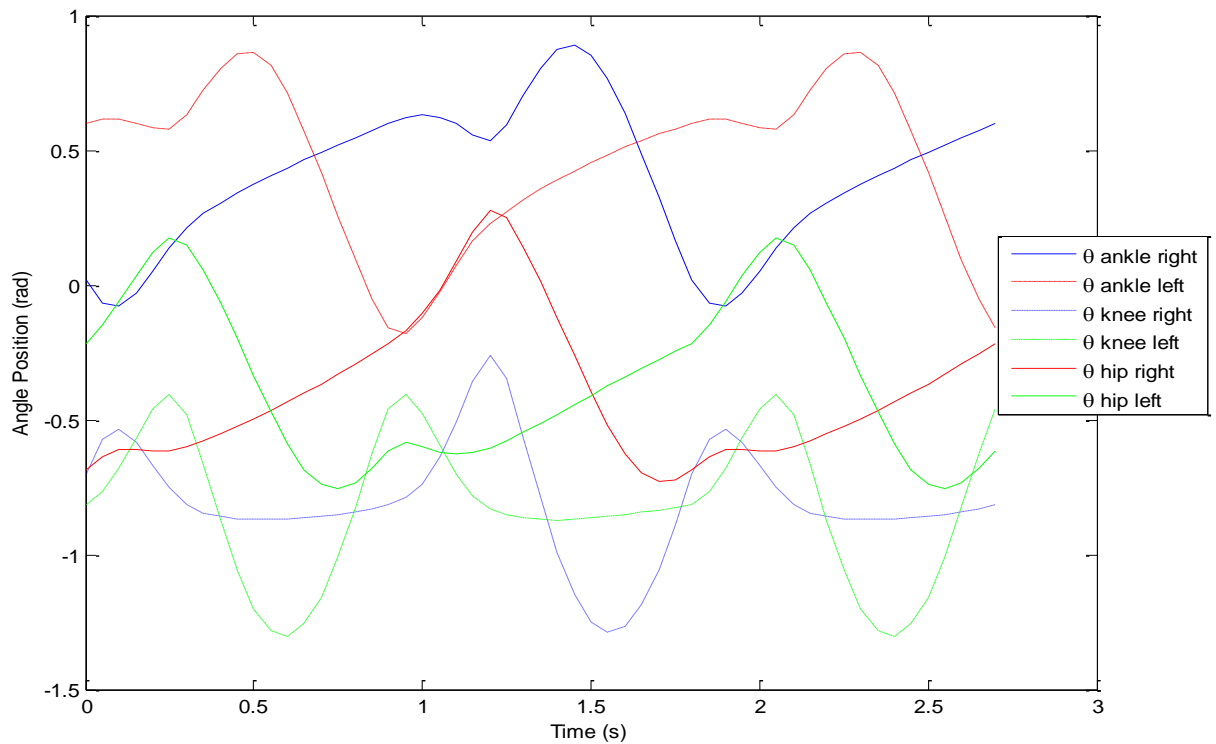


Figure 3.25 Joint angle position splines for two steps of gait 2

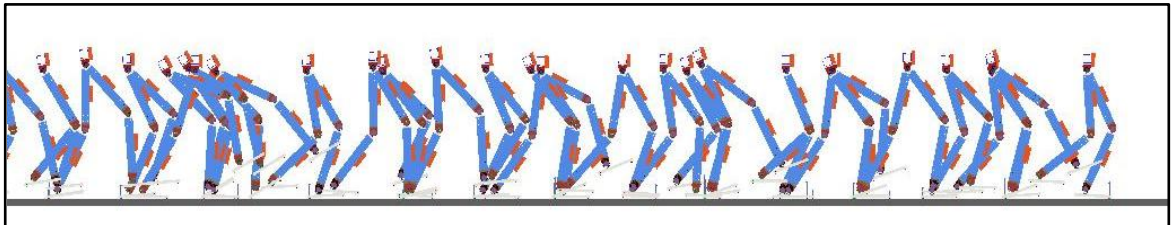


Figure 3.26 ADAMS simulation for gait 2 showing superimposed images in every 0.5 s  
(total of 14 s)

Center of mass location in sagittal plane is 430 mm from the bottom of the feet when the robot is in standing configuration. Change of center of mass in cartesian coordinates is showed in Figure 3.21 and Figure 3.28.

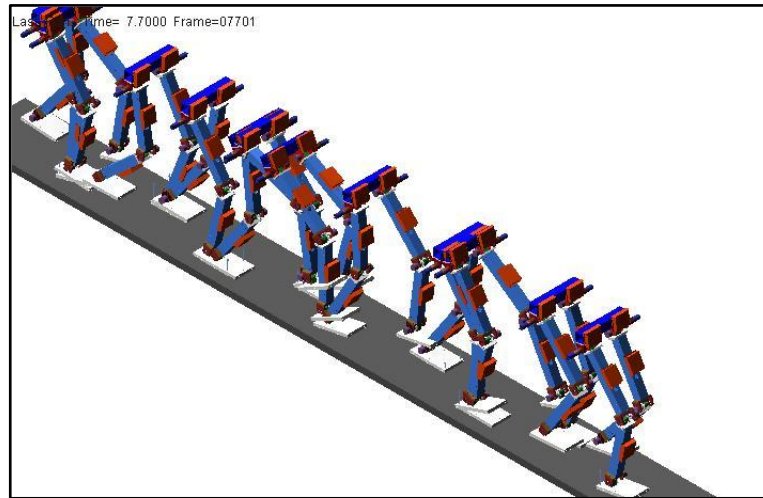


Figure 3.27 ADAMS simulation for gait 2 showing superimposed images in every 0.5 s (total of 8 s)

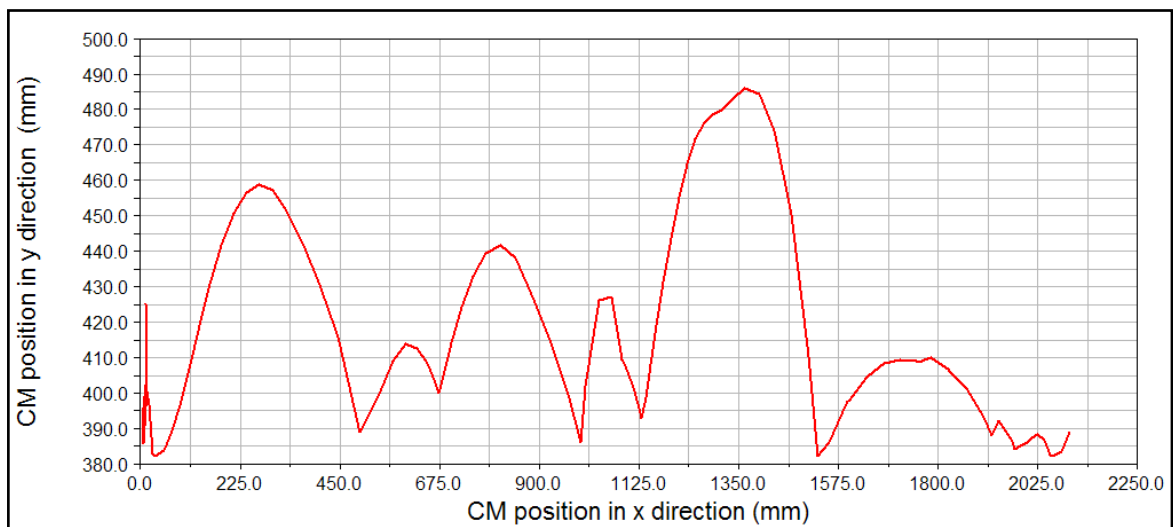


Figure 3.28 Center of mass location in x and y coordinates for gait 2

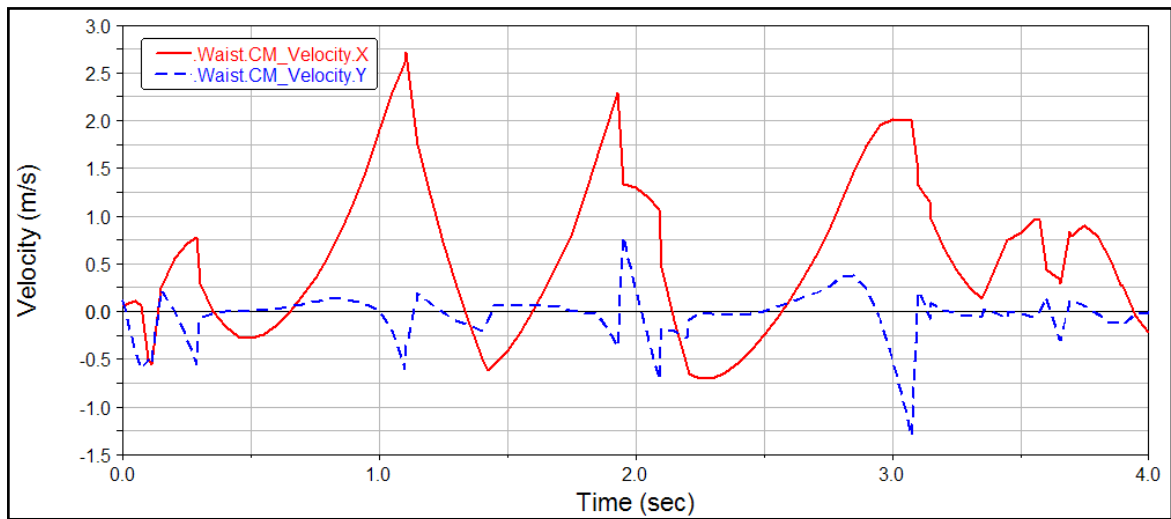


Figure 3.29 Velocity of the hip joint in x and y direction for gait 2

In Figure 3.23, front view of ADAMS simulation driven by gait 1 is shown. Figure 3.26 and Figure 3.27 shows the front and isometric views of ADAMS simulation, driven by gait 2. Both gaits have limping behavior. Gait 2 is found more stable than gait 1 because robot is falling down after 10 steps in gait 1. The robot in gait 2 simulation walked 15 steps which is the length of the spline and fitted to a stable walking pattern. Although, limping action increases power consumption and jerk, stable gait is obtained as shown by ADAMS simulation results.

## **4. DESIGN & PROTOTYPING**

Selection of components for the robot is a very important part of the design process. After a full-scale internet search the parts that satisfy the required specifications are filtered and a purchase list with the rough descriptions of the parts such as, brand, model, main specs, link to datasheets, distributor and price has been created. To compute the requirements, small programs or spreadsheet files (called selection tools) are created. For example gear selection tool that calculates all the forces on the joint gears was quite useful because the forces that occur on bevel gears can harm important components like the gearhead. Components research is divided into 3 main sections with respect to their usage of components: drive components, structural components and sensors.

### **4.1. DRIVE COMPONENTS**

Drive components section includes all the actuation and control parts of the robot like motors, gearheads, bevel gears, gearboxes, and motor controllers. There are several actuation choices in literature for biped robots. Alternatives include use of electric motors, hydraulic, or pneumatic actuation. Electric motors are preferred due to flexibility in application, providing compact packages and considered as clean systems. Besides, they have some disadvantages like poor force to weight ratio and running at high speeds to generate the required torque. For this reason speed reducers are usually necessary. The downsides of using speed reducers include increased complexity, weight, compliance and backlash.

The necessary torques to drive the biped robot is computed by simulations. A right combination of bevel gears, gear heads, motors, motor controllers that will meet the desired criteria has to be selected. Design criteria for selecting the drive components are maximum continuous and intermittent torque, output speed of the gearbox, motor power, rated motor current and peak current values that the motor control unit can supply.



#### 4.1.1. Motor, Gearbox and Control Unit Selection

In the previous sections, primary ADAMS simulations provide enough data to select the suitable set of motor and gearbox in the market. Maxon and Faulhaber brands are considered due to their high precision miniature products. Selection of motors and gearboxes for each joint type are made separately. Accordingly, ankle joint have the highest torque value (11 Nm, rms) and knee joint have the highest angular speed (70 rpm, max).

Preferred motor control unit is a smart brushless motor control unit that can provide 5 A continuous, 10 A intermittent current. Motor control units and all other electrical hardware components in the system are selected in order to work with a 15 V rechargeable battery supply, when it is necessary.

Maxon motor company catalogs and product selection tools are intensively used. Product selection guide (Figure 4.1) makes possible to enter load, drive layout (bevel gears) and electrical supply as inputs to the program. Drive layout input has already been chosen due to specified load and angular velocity. In this section, gear ratio and efficiency values are entered. Load values are determined from simulations and various calculations for each joint. Cyclic load is chosen, thus rms and maximum load torque, duration of maximum load and maximum load speed for each joint are given. Parameters in electrical supply block are selected according to available battery specifications. In the light of the foregoing, suitable gearbox, motor, sensor and control unit combinations are listed by the program and most efficient ones are chosen for each joint.

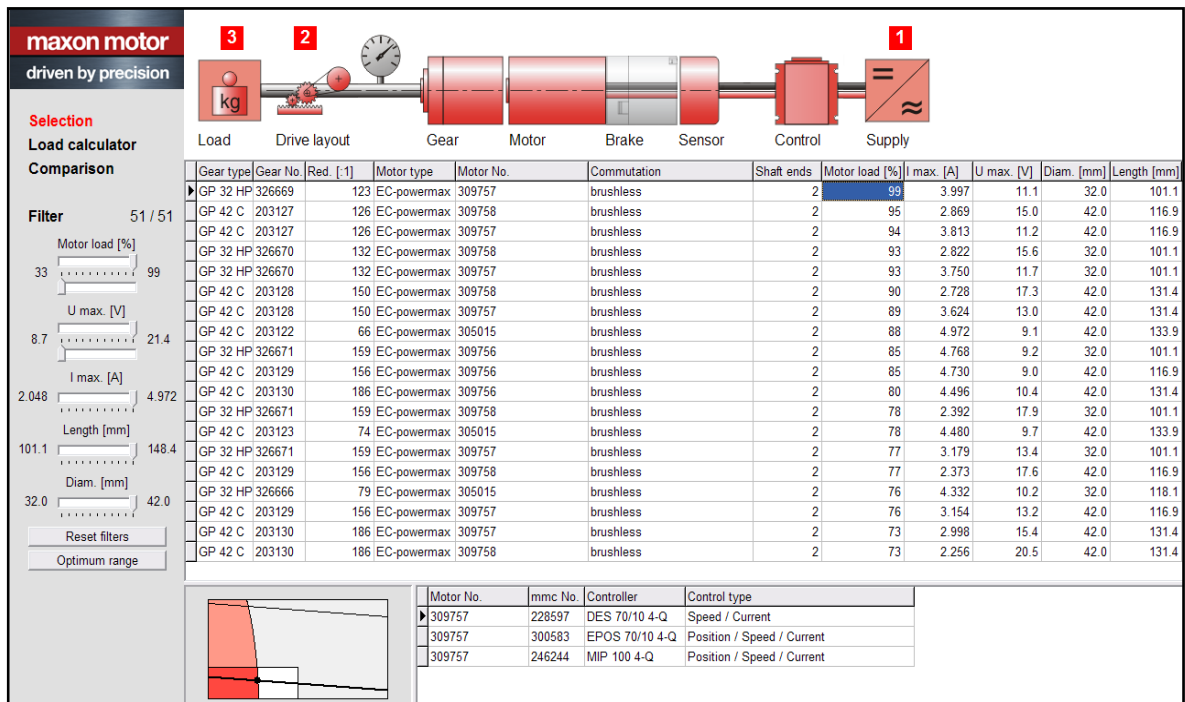


Figure 4.1 Screenshot of the Maxon Motor Selection Program (msp)

Speed-torque diagrams for the motors are provided by the program. The program also comes with the ability to check whether desired operating conditions remain in the continuous operating region of the speed-torque diagrams. Figure 4.2 shows the speed-torque diagram of the knee joint motor. The point on the left of the diagram refers to the desired continuous operating condition and the point on the right refers to the desired intermittent operating condition. Dark area is the allowable continuous operating region. All other lines are labeled on the right of the diagram.

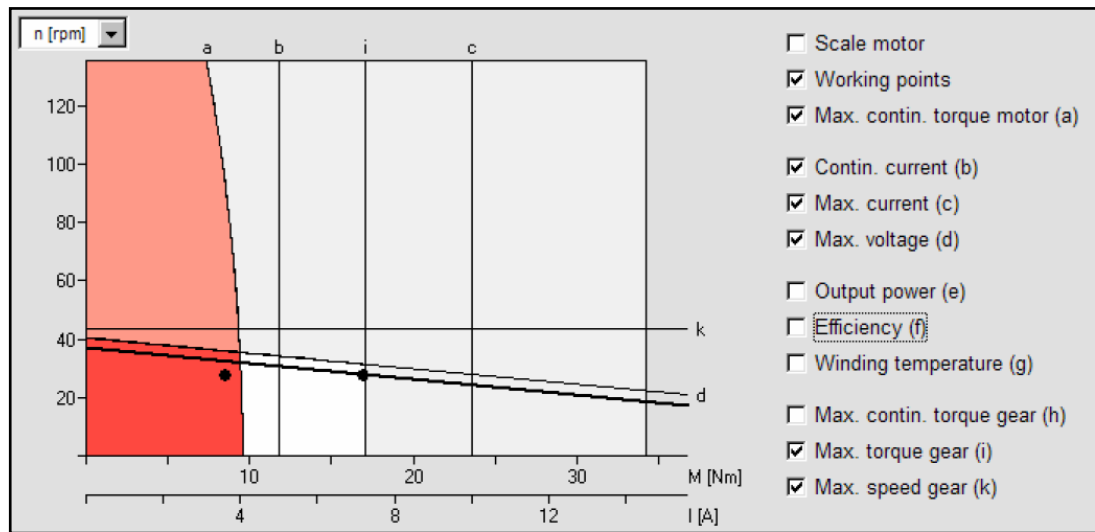


Figure 4.2 Knee joint actuator characteristics

#### 4.1.2. Gear Selection

After many conceptual designs, for the sake of compactness and stability of the robot, a joint design that encapsulates the motor within the leg link is chosen. In this design, the motor is placed to be in line with the leg link. This requires that the joint be constructed in such a way that the motor output shaft and the joint axis are perpendicular to each other. This design reduces the overall volume of the joint, therefore, reduces the risk of entanglement with the other legs or the surrounding obstacles in the environment as the biped robot takes a step.

Bevel gears are suitable for this application due to their high efficiency, low weight and backlash properties. A large market search about bevel gears had been done. Atlanta Gear Company products are preferred as a result of their durability to high moment values. Several gear selection diagrams are used that are provided by this company. These diagrams set operating factors that depend on shocks, speed and safety. After these factors are determined, they are multiplied by input torque and this new torque value was used in a final gear selection diagram that establishes the module of the gear. As a tool for this purpose, a bevel gear selection program (Table 4.1) is developed by using the classical bevel gear selection parameters in the firm catalogs [37].

Table 4.1 Bevel Gear Selection Guide (values are for the knee joint)

$C_{a_p}$	$C_{a_g}$	$d_{o_1}$ (mm)	$T_1$ (Nm)
480	720	32	12
$F_{a_p}$ (N)	$F_{a_g}$ (N)	$F_{r_p}$ (N)	$F_{r_g}$ (N)
180	270	270	180

Table 4.2 Bevel Gear Selection Guide (values are for the ankle joint)

$C_{a_p}$	$C_{a_g}$	$d_{o_1}$ (mm)	$T_1$ (Nm)
390	780	30	22.5
$F_{a_p}$ (N)	$F_{a_g}$ (N)	$F_{r_p}$ (N)	$F_{r_g}$ (N)
292	585	585	292

In Table 4.1 and Table 4.2, loads acting upon the bevel gear pair are determined by the following procedure. First, a table of factors that are supplied by the manufacturer is used. This table evaluates the calculation factors depending on gear ratios that are presented in Table 4.1 as  $C_{a_p}$  and  $C_{a_g}$ .  $T_1$  is the maximum input torque,  $d_{o_1}$  is the pitch diameter of the pinion.  $F_{a_p}$  is the axial force on pinion,  $F_{a_g}$  is the axial force on gear,  $F_{r_g}$  is the radial force on gear,  $F_{r_p}$  is the radial force on pinion. Secondly, equations 4.1 to 4.4 are implemented in MS Excel to compute forces acting upon the bevel gear pair.

Desired joint moments are obtained by walking simulations. Bevel gear ratios of 1:1.5 and 1:2 are found suitable for knee and ankle joints. Motor gearheads on hip joints handle required moments; therefore hip joints are designed as directly coupled to the motors.

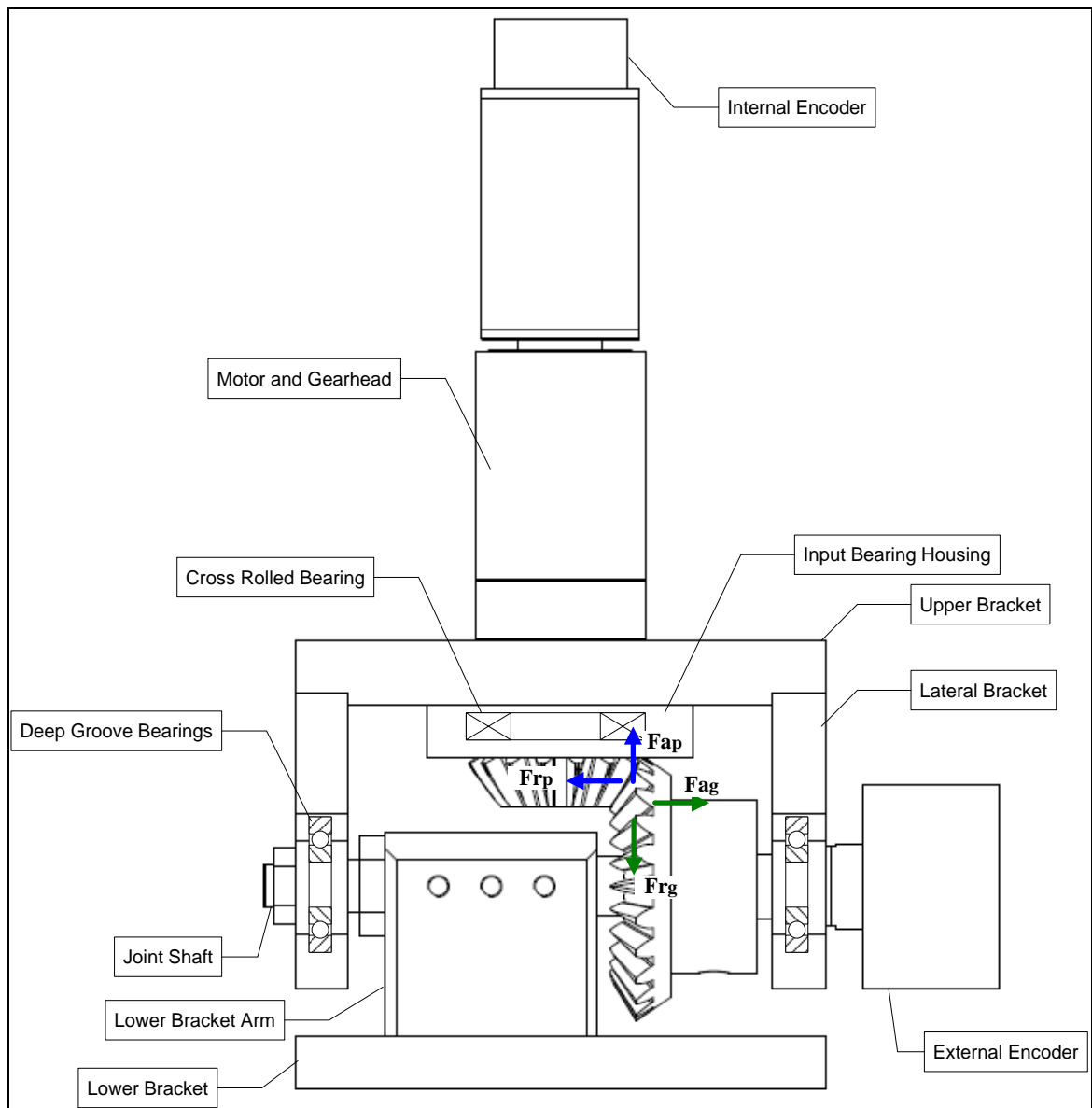


Figure 4.3 Description of joint design and gear force calculation parameters

$$F a_p = \frac{T_1}{d_{o1}} C a_p \quad (4.1)$$

$$F a_g = \frac{T_1}{d_{o1}} C a_g \quad (4.2)$$

$$F r_p = \frac{T_1}{d_{o1}} C a_g \quad (4.3)$$

$$Fr_g = \frac{T_1}{d_{o1}} C a_p \quad (4.4)$$

By utilizing this tool, bearings are selected on the motor side and the output shaft side. Forces calculated by this tool indicate that maximum axial forces and moments generated by these forces on the motor side exceed the limitations of the motor. Thus, crossed roller bearing type is chosen on motor side due to their compactness and durability on axial forces and moments. Results of the load calculations for the ankle joint are shown in Table 4.2.

## 4.2. STRUCTURAL COMPONENTS

Lower extremity of an anthropomorphic robot must have limbs such as shank, thigh, waist, foot and torso. These limbs hold together the robot. For this purpose, components must not only have enough strength, but also has to be lightweight. There are several materials that can satisfy these properties such as, Delrin, aluminum and carbon fiber (Table 4.3). Among the materials considered, Delrin has the lowest density ( $1420 \text{ kg/m}^3$ ), has a modulus of elasticity of 3000 MPa and a tensile strength of 71 MPa. Carbon fiber has the best strength/mass ratio among the materials considered. However, due to its high cost, inconvenient machinability and difficulty in finding in the market, it is not chosen. Aluminum 6000 series sticks out with its ease of finding, low cost, good strength properties and availability in various off the rack shapes.

After material is selected, the profile shape for the link segments is discussed. First cylinder shape is considered but this shape came with assembly difficulties. A rectangular profile is much easier to assemble to joint mechanisms by gussets. 60x60 mm ready-made aluminum square profile with 2.5 mm thickness is selected for waist, shanks and thighs. Feet are made with 2 optional materials due to their stiffness. One of them is aluminum 6000 series and the other one is Delrin 100P.

In joint mechanisms two types of materials are used. Most critical components of the robot are determined as the shafts and couplings in joints. Among the materials considered, 1040 steel is chosen for the shafts and 304 stainless steel for couplings.

Table 4.3 Structural materials and their properties [38]

<b>Material</b>	<b>Density (kg/m<sup>3</sup>)</b>	<b>Tensile Strength (MPa)</b>	<b>Modulus of Elasticity (GPa)</b>
Carbon-fiber, Thornel® P-25 Continuous Pitch-Based Fiber	1900	1380	160
304 Stainless steel	7700	568	190
1040 Steel	7700	620	207
Delrin 100P	1420	71	3
7075-T6 Aluminum	2800	503	72
6061-T6 Aluminum	2700	310	69

All the components except the shafts and couplings of the joints are manufactured from 7075-T6 aluminum. This is mainly because of manufacturability, low density and high tensile strength properties of this material.

### 4.3. LATERAL SUPPORTING SYSTEM

Since the biped robot is initially designed as a planar robot, a lateral supporting system is crucial to constraint the motions of the robot in the sagittal plane. In the literature, wheel horse like mechanisms or designing robot with dual feet and legs are common approaches. These approaches are inadaptable to our project because, wheel horse like mechanisms need a big space due to length of the support bar and duplicating feet and legs approach increases complexity of the structure. Hence, a new lateral supporting system is designed. System consists of linear motion guides that are fixed to a wheeled carrier structure. There are two linear motion guides on the horizontal axis and an aluminum plate connects linear motion guide carts together. On this aluminum plate a vertical linear motion guide is mounted, thus the motion is constrained to be planar. Rotation on this plane is obtained by a bearing, which is mounted on the robot's waist. This supporting system also prevents the robot to fall down. To provide sufficient structural strength of the lateral supporting system, basic load calculations are done. As a result, vertical linear motion guide is designed as a two cart system to endure moments due to impacts by falling down. Horizontal motion guide length is determined by considering the step length of the robot. The vertical motion guide length is determined by considering the vertical movement limitations of the robot, as shown in Figure 4.4.

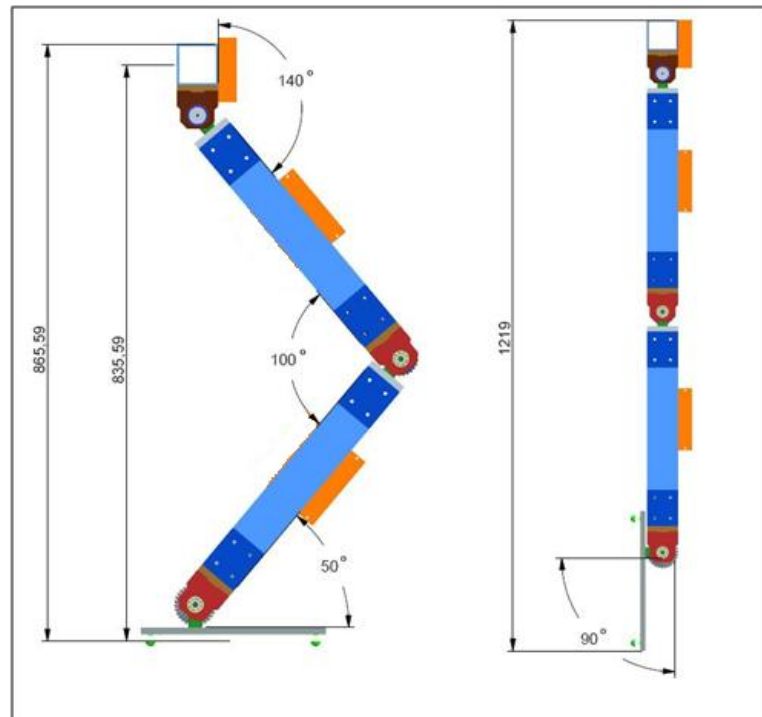


Figure 4.4 Vertical collision limitations of robot's movement

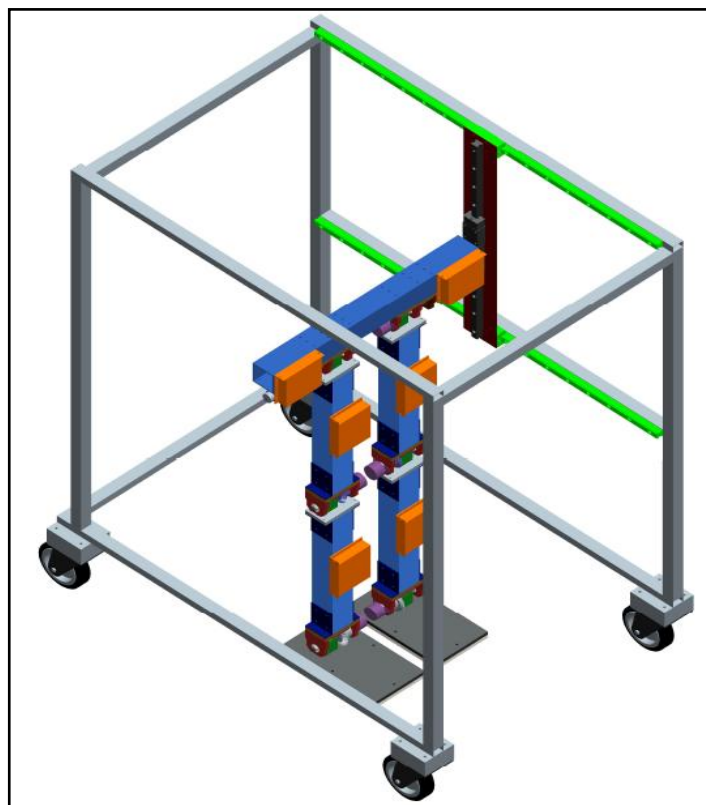


Figure 4.5 Lateral supporting system and robot assembly



Figure 4.5 shows the integration of full robot assembly and lateral supporting system. Green rails are the horizontal linear motion guides. They are connected together by an aluminum plate (dark red in the picture). This aluminum plate not only keeps horizontal guides together but also it creates a ground to fix the vertical linear motion guide which is the dark gray one in Figure 4.5.

#### **4.4. ELECTRICAL AND CONTROL SYSTEM DESIGN**

Electrical and control system design section covers the design and selection of the sensors, implementation, interfacing and general electrical design of the whole robot. Electrical assembly layout of the robot is shown in Figure 4.6. Selection of the sensors is done by considering brand, model, price and main sensor specifications such as sensitivity, measurement range, supply voltage and interface. An individual battery is placed for each motor controller. This independent power source approach has some benefits such as avoiding the cabling mess and enabling battery charging from regeneration power of the motors.

Advanced features of Maxon EPOS2 motor controllers (Figure 4.7) make possible to use them as a data acquisition system. Therefore, not only they control the motors, but also they gather data from external encoders, force resistive sensors and inertial measurement unit. EPOS2 motor controllers can create a data flow network by communicating each other via CAN (Controlled Area Network) protocol. Hence, every EPOS2 have a role as a data concentration point on the network. This entire CAN bus network is connected to a main computer by a USB bus.

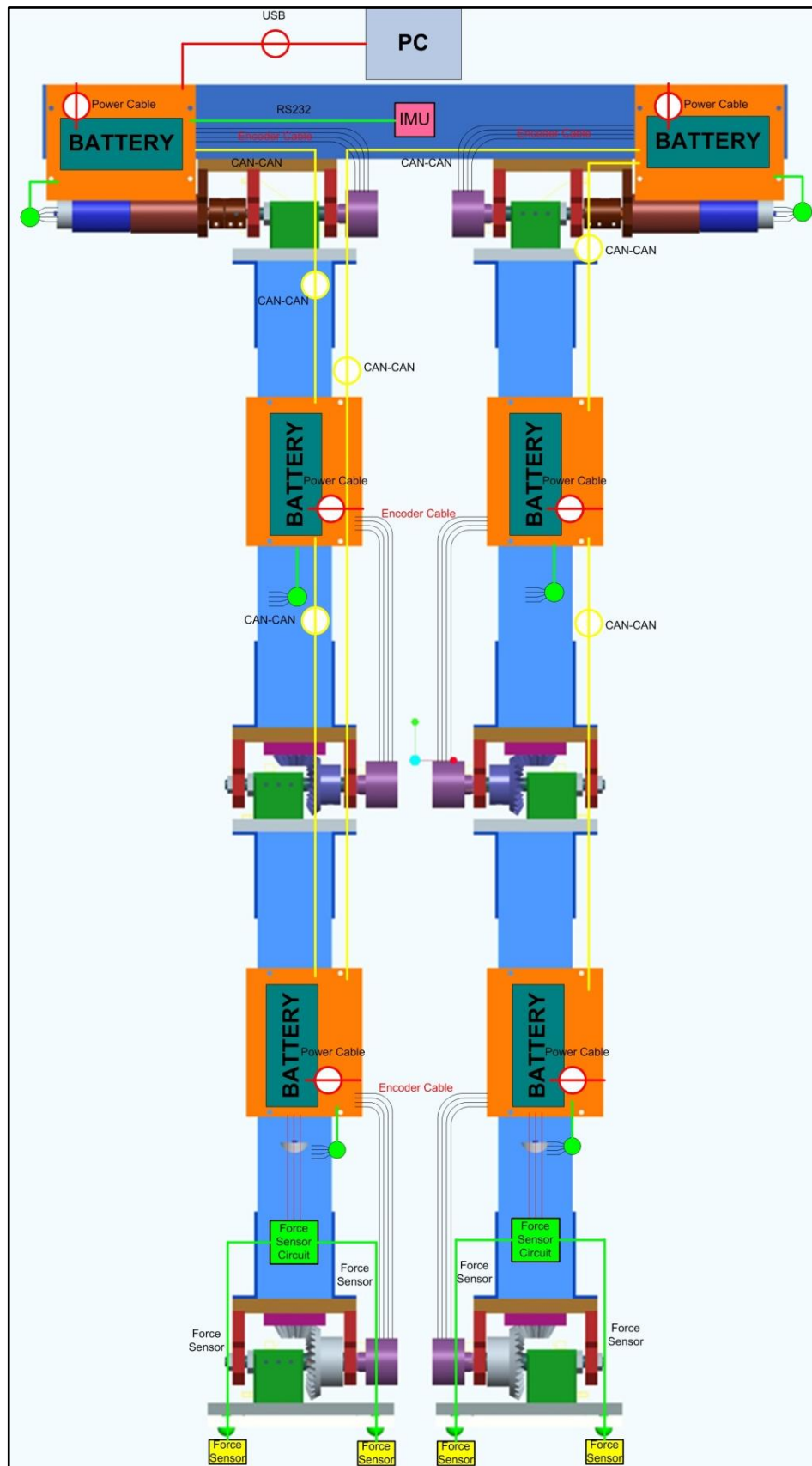


Figure 4.6 Electrical assembly diagram of the sub-systems of the robot



Figure 4.7 Maxon EPOS2 motor controller [33]

As shown in Figure 4.7, EPOS2 has various communication alternatives. Power supply and logic supply are main electrical supply jacks. Logic supply is optional but, it offers major advantages like safe and economical power backup features. Motor, hall sensor and encoder jacks are motor related jacks. Motor jack transmits power to the motor. Hall sensor jack is needed for detecting rotor position of the motor. An internal encoder with a built-in line driver is necessary for self positioning control of the motor. EPOS2 is endowed with three communication protocols, which are USB, RS232 and CAN. Drive systems typically require inputs and outputs; on this purpose EPOS2 device supports two analog inputs and one output from signal 3 connector. Furthermore, 11 digital inputs and 5 outputs are available with general and specific purposes.

#### 4.4.1. IMU and External Encoders

Inertial measurement unit (IMU) and external encoders provide vital information regarding the position and orientation of the biped robot. IMU can determine robot's

position and orientation with respect to the ground and external encoders determine the angular position of joint shafts reliably. Information provided by the encoders is not affected by backlash on gearheads and bevel gears. Hollow type Nemicon HES encoder (Figure 4.8) is selected. EPOS2 uses internal encoders only to drive the motors. Internal encoders have 1000 pulses per turn, but external encoders have 3600 pulses per turn. External encoders can be connected to EPOS2 digital input ports.



Figure 4.8 Picture of Nemicon HES external encoder [34]

While external encoders enable true joint angular position measurements, IMU detects robot's global position and orientations in the form of numerical integrations of accelerations and angular velocities. Microstrain 3D-GX2 (see Figure 4.9) is endowed with a RS232 interface. Thus, data acquisition from this device can be achieved by EPOS2. The unit consists of roll, pitch, and yaw gyro sensors and includes three axis translational acceleration sensors. This sensor is temperature and magnetic field compensated. It has sensitivity of  $\pm 0.005$  g within a  $\pm 5$  g range for translational movements and a sensitivity of  $\pm 0.2^\circ/\text{sec}$  within a  $\pm 300^\circ/\text{sec}$  range for rotational movements. Acceleration, angular rate, deltaAngle and deltaVelocity, Euler angles, and rotation matrix output modes are available.



Figure 4.9 Picture of Microstrain 3D-GX2 Inertial Measurement Unit [35]

#### 4.4.2. Foot Contact Sensors

The zero moment point (ZMP) concept was introduced in 1969 by Vukobratovic, and has since been widely used as a measure of stability of biped robots. In the literature different definitions of the ZMP can be found, the most common is “If there is no rotation of the supporting foot (or feet) about its (or their common) edge during walking, ZMP is the point on ground, where the moments around any axis, passing through this point and being tangential to the ground, is equal to zero” by Vukobratovic [11]. Although ZMP is generally defined in x and y axes, a planar biped robot’s stability varies in the x axis only. Equation for ZMP [13] is constructed as follows:

$$X_{zmp} = \frac{\sum_i^n m_i(\dot{y}_i + g)x_i - \sum_i^n m_i y_i \ddot{x}_i - \sum_i^n I_{iy} \alpha_{iy}}{\sum_i^n m_i(\dot{y}_i + g)} \quad (4.5)$$

where  $m_i$  is mass of the  $i^{th}$  link,  $I_{iy}$  is the inertia and  $\alpha_{iy}$  is the angular acceleration of the  $i^{th}$  link about y axis,  $z_i$  and  $\ddot{z}_i$  is the position and acceleration of the  $i^{th}$  link in z axis direction with respect to ground, g is the gravity.

Since dynamic stability is measured by the ZMP method, experimentally it must be measured by force/torque sensors. Due to their good shock resistance, low price and

thickness, FlexiForce (see Figure 4.10) brand force sensitive resistors (FSR) are used in this project. The FSR sensor is an ultra-thin and flexible printed circuit, which can be easily integrated into most applications. With its paper-thin construction, flexibility and force measurement ability, the FSR force sensor can measure force between almost any two surfaces and is durable enough to stand up to most environments. The sensors are constructed of two layers of substrate. This substrate is composed of polyester film (or Polyimide in the case of the High-Temperature Sensors). On each layer, there is a conductive material (silver), followed by a layer of pressure-sensitive ink. An adhesive is applied to laminate the two layers of substrate together to form the sensor. The silver circle on top of the pressure-sensitive ink defines the “active sensing area.” Silver extends from the sensing area to the connectors at the other end of the sensor, forming the conductive leads. A 0-110 N ranged version is used with a linearity (error) of  $\pm 3\%$ .

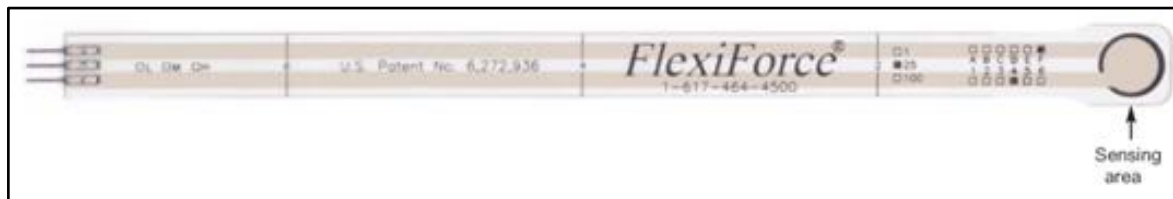


Figure 4.10 Force Sensitive Resistor [36]

Design of a sensor circuit was essential, because the sensor acts as a variable resistor in an electrical circuit. When the sensor is unloaded, its resistance is very high (greater than 5 Mega ohms); when a force is applied to the sensor, its resistance decreases. To convert this resistance value into a 0-5 V analog output, a basic op-amp circuit is designed (Figure 4.11). As seen in Equation 4.6, the test voltage,  $V_T$  must be negative for this circuit. The negative  $V_T$  will result in a positive 0-5 V analog output signal that can be measured by EPOS2.

$$V_{out} = -(R_{feedback}/R_{flexiforce}) \cdot V_T \quad (4.6)$$

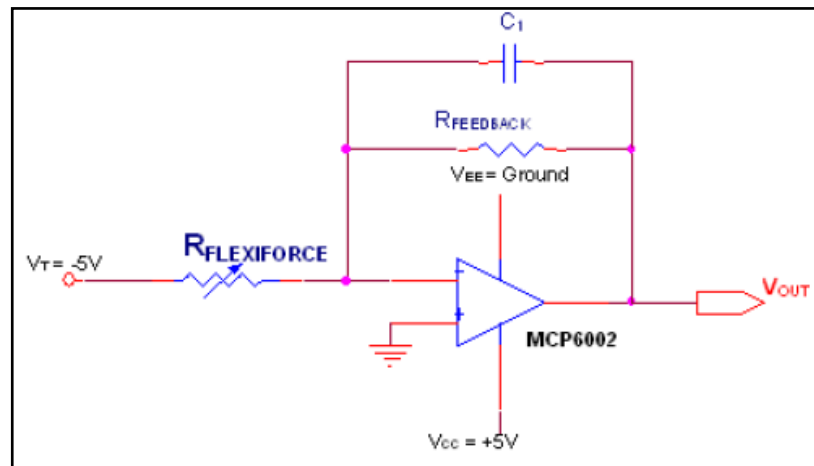


Figure 4.11 Dual-source inverting amplifier circuit for FSR sensors [36]

Different  $R_{\text{feedback}}$  choices directly affect the relationship between the output voltage,  $V_{\text{out}}$ , versus the force applied. As the value of  $R_{\text{feedback}}$  increases, the corresponding values of  $V_{\text{out}}$  also increase at the same applied force. Briefly, as  $R_{\text{feedback}}$  or  $V_{\text{out}}$  increases, measurable force range decreases by preventing saturation of the circuit output for a given force. Conversely, slope of the voltage vs. force curve is escalating. Therefore the sensitivity of the circuit is decreasing. In sight of this information,  $10 \text{ k}\Omega$  for  $R_{\text{feedback}}$  resistance and  $-5\text{V}$  for  $V_T$  are selected. A  $\pm 5 \text{ V}$  is supplied to circuit by using  $9 \text{ V}$  batteries and  $7905$ ,  $7805$  voltage regulators.

It is recommended that a capacitor ( $C_1$ ) in the range of  $47$  to  $270\text{pF}$ , be connected in parallel with  $R_{\text{feedback}}$  due to the associative capacitance of the FSR sensor. There will be substantial oscillation in the circuit output if it is omitted. A  $47\text{pF}$  capacitor is used in the circuit. MCP6002 low power op-amp which handles  $2$  FSR sensors is used.

In Figure 4.6, connection of the FSR sensors to EPOS2 can be seen. Each EPOS2 has  $2$  analog inputs, besides there are  $4$  FSR sensor output for each foot. Inadequacy of analog input ports is resolved by using optocouplers. By the way, optocouplers are switching the  $V_{\text{out}}$  of two FSR sensors and so  $V_{\text{out}}$  is transmitted to EPOS2 by turns.

Figure 4.12 shows printed circuit board layout that can handle  $4$  FSR sensors. As it is noticed in the layout, there are additional components in the circuit such as LEDs, resistors

and capacitors. Additional capacitors are used for stabilizing the input and output voltages of voltage regulators and preventing noise of other components. LEDs are used to indicate which FSR is turned on by optocouplers and to check the power supply. LEDs and a few components need additional resistors.

FSR's are mounted at four corners of each foot for measuring the moment and the ground reaction force under the feet. It is easy to compute ZMP, once the moment and the total ground reaction force is measured (Equation 4.5). The entire sensing area of the FSR sensor is treated as a single contact point. For this reason, the applied load should be distributed evenly across the sensing area to ensure accurate and repeatable force readings. Readings may vary slightly if the load distribution changes over the sensing area. This condition is achieved by using rubbers that fits sensing area of the sensor. Rubber material also compensates for the shear forces and protects the FSR sensors

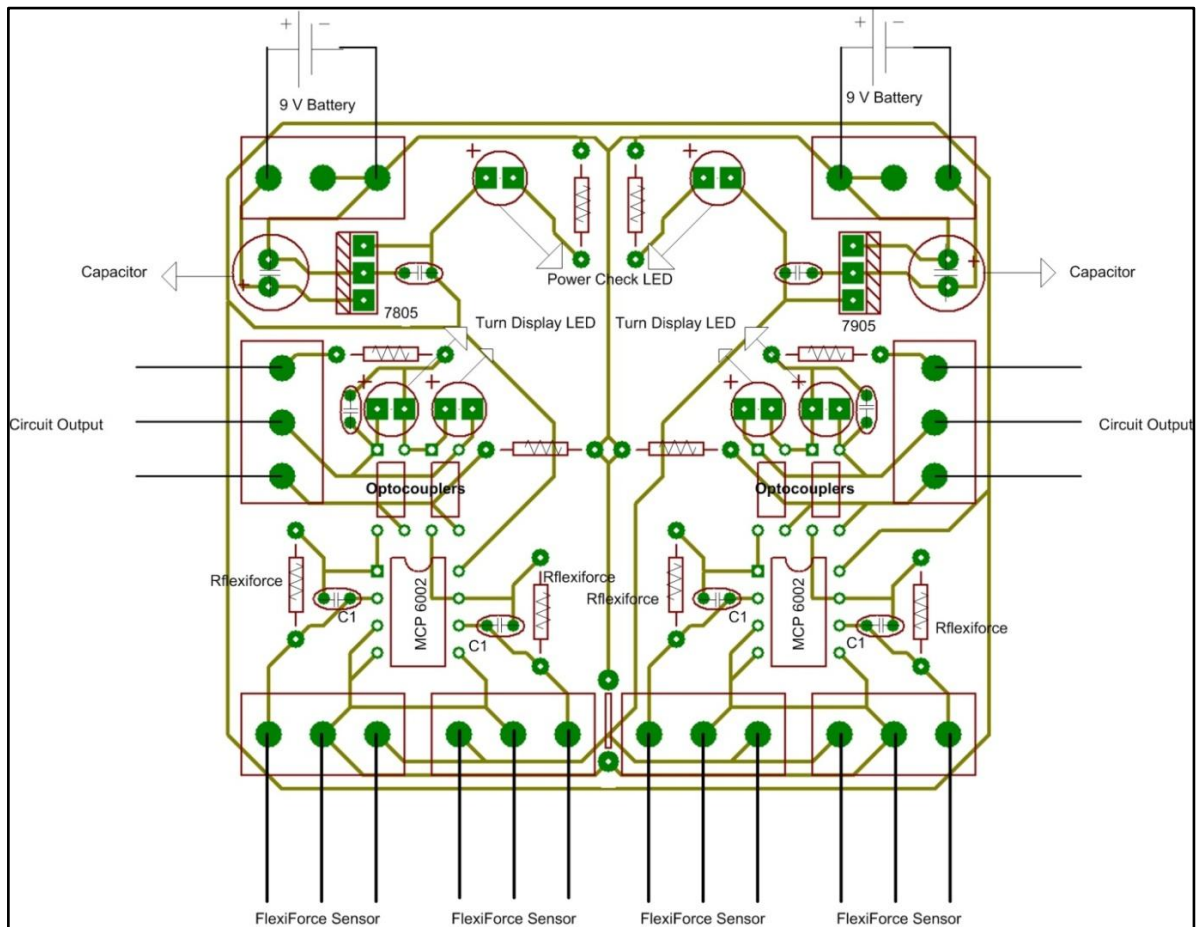


Figure 4.12 PCB component layout of the FSR sensor circuit



Two different FSR testing apparatus are set. First a manual experimental setup is installed. To obtain accurate results, sensors are conditioned before testing. Conditioning procedure is required for new sensors, and for sensors that have not been used for a long time. To condition a sensor, 110% of the test weight (120 N) is placed on the sensor, and waited until the sensor stabilizes, and then removed the weight. This process is repeated four or five times. For measuring the resistance of the sensor a multimeter is used.

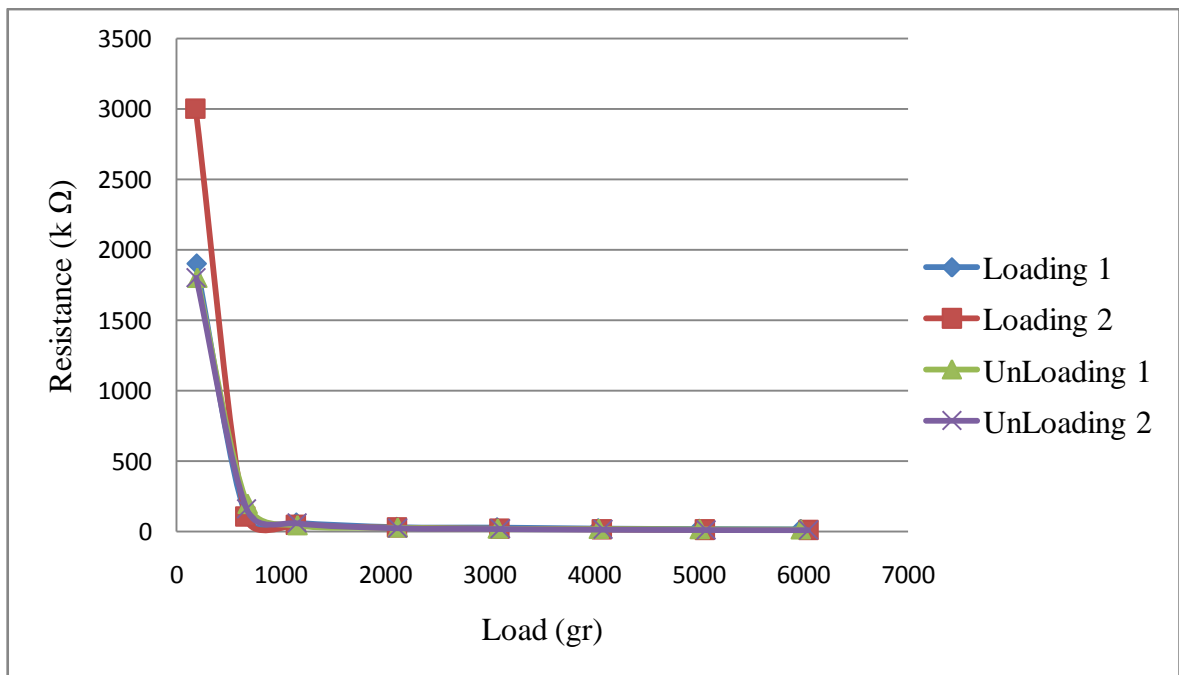


Figure 4.13 FSR sensor resistance with respect to load

As seen in Figure 4.13 and Figure 4.14, FSR sensors are loaded and unloaded two times. Loading starts from 0.5 kg and loaded up to 6 kg with 1 kg increments. Unloading procedure is reverse application of the loading procedure. Linearity of the sensor can be seen in Figure 4.14.

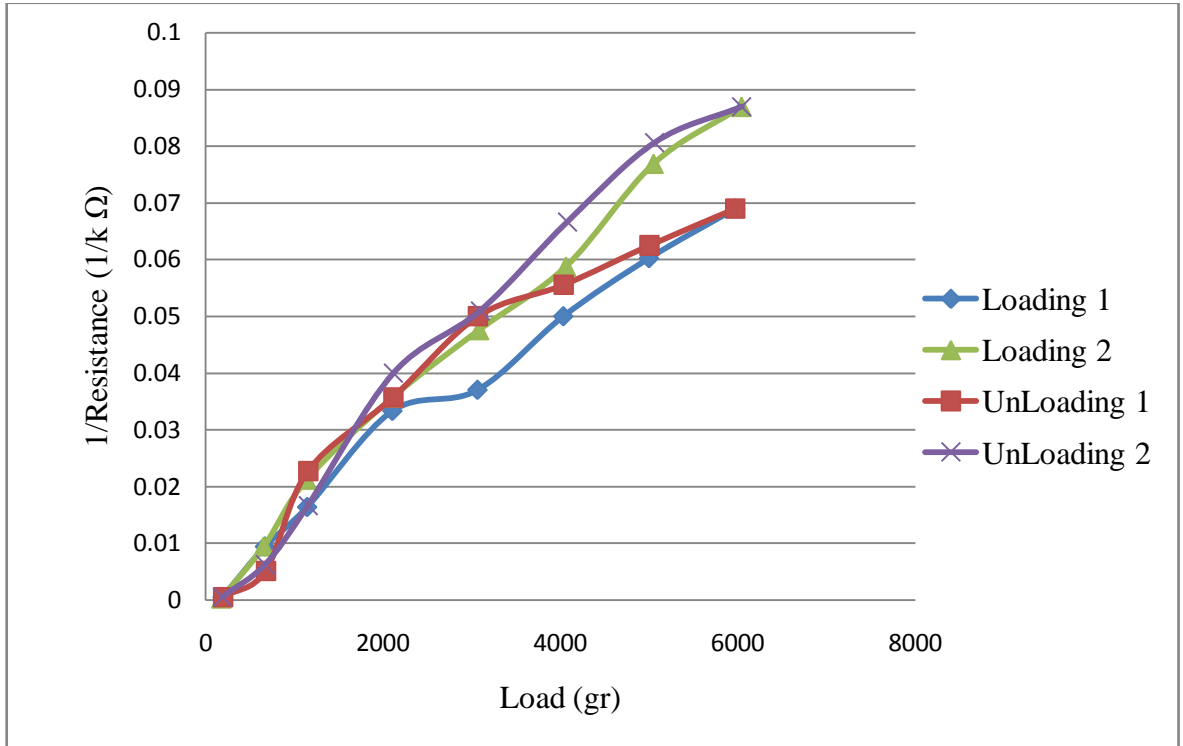


Figure 4.14 FSR sensor's conductance with respect to load

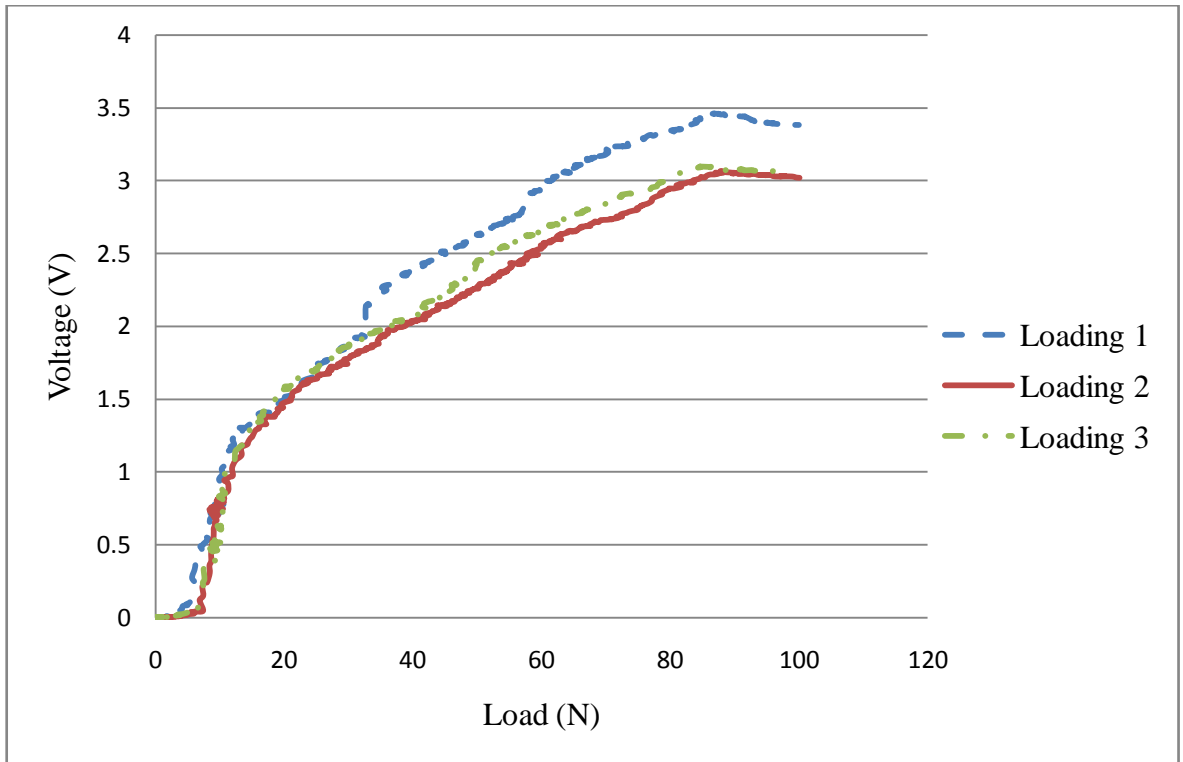


Figure 4.15 FSR sensor circuit's  $V_{OUT}$  with respect to load

After the FSR circuit is obtained, a more sophisticated testing apparatus is installed. Loading process is done by using “Instron” branded tension test system is used. By using a tension test system, a more reliable loading process is obtained. While load values are taken by the load sensor of the tension test system, voltage output values of the FSR circuit are gathered by a USB interfaced desktop multimeter.

#### 4.5. COMPUTER AIDED DESIGN (CAD)

In this section, the design of the robot in the CAD environment is described. Biomimetic approach is chosen throughout the project. For this purpose, research has been done on human lower extremity and anthropomorphic dimensions. In Figure 3.7 human segment length proportions based on the total height is shown. The strength of the components and the use of light weight components are primary design considerations. Some components such as motors have already been chosen before the mechanical design process. All phases of the CAD have been revised many times that converges to a final result. CAD is done in Pro Engineer Wildfire 3 software.

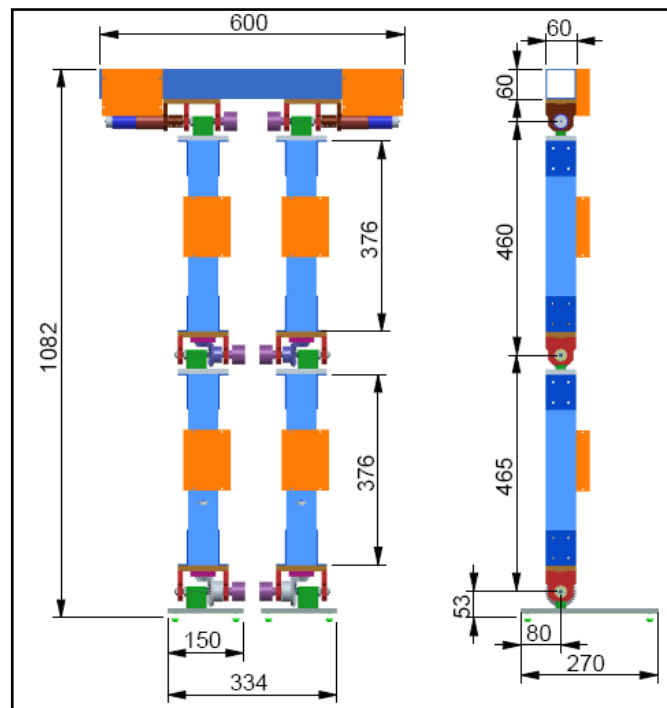


Figure 4.16 Main dimensions and segment lengths of the robot (mm)

Figure 4.16 demonstrates the main dimensions and segment lengths of the robot. Total width and length of the robot are 600 and 1082 mm. Segment lengths are initially based on human proportions on Winter's book [32]. But, length of waist is kept long on purpose to keep hip motors protected. Figure 4.17 displays the isometric view of the robot assembly. Results of the modeling and simulation study play an important role in the design of the robot.

Knee and ankle joints are the most critical parts in the design. Thus, knee joint is chosen as a starting point to the mechanical design of the robot.

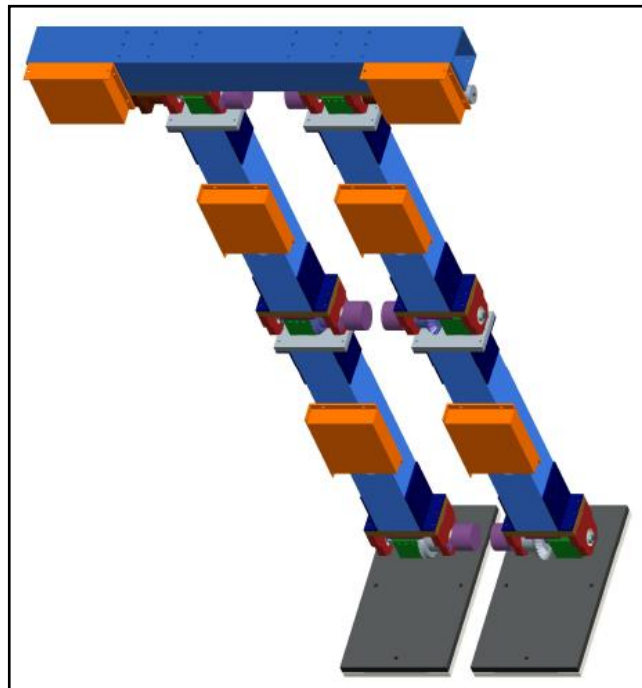


Figure 4.17 Isometric view of CAD of the fully assembled robot

#### 4.5.1. Knee Joint Design

Knee design was an important part of the mechanical design section. Various optimizations and revisions have been made in accordance with the new simulation and calculation results. Actually, robot evolved in the CAD environment in quite a short time. This is the main benefit of using CAD in a project.

In the beginning of the knee design, selected parts were motor, gearhead and bevel gears. With the material in hand, preliminary design in Figure 4.18 is evaluated. Cylindrical profiles are considered as link segments to be compatible with the geometry of motors. These pipe segments were connected to the upper bracket of joint by flanges (purple in Figure 4.18). Upper and lower brackets were all one-piece. All of the components are designed in round shapes to provide coherence with general joint movements. External encoder is not revealed yet.

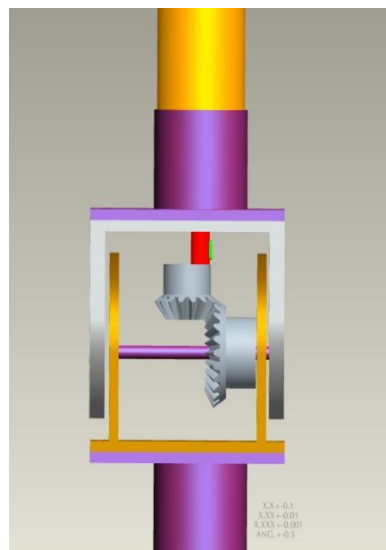


Figure 4.18 First version of the knee joint design, (May 2008)

After selecting the external encoders, their geometry is modeled and added to the assembly. For compactness, external encoders are placed inside the joint (yellow in Figure 4.19). Cabling for electronic components is contemplated in this design. Therefore, slots for motor cabling are made on the pipe segments. Also, EPOS2s are modeled and placed below the knee joint in a back to back arrangement (orange parts in Figure 4.19).

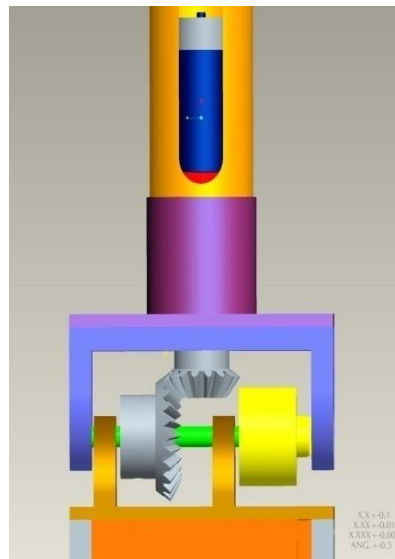


Figure 4.19 Second version of the knee joint design, (July 2008)

In the third version of the knee design (see Figure 4.20), manufacturability considerations and load calculations became the preliminary interest in the revision of the design. To this end, upper and lower brackets are divided into smaller parts. This way, manufacturing has become easier and cheaper. Upper bracket is divided to three parts as one upper bracket and two lateral brackets. Lateral brackets have bearing bushings. Lower bracket is separated into two parts as lower bracket arm and lower bracket. In the previous design versions, pinion was fitted to the gearhead shaft directly. However, calculations of forces on the bevel gears (see Table 4.1) indicate these forces will be greater than the gearhead's axial load limitations. To prevent the axial force on the gearhead a crossed roller bearing is considered. A new bearing means a new bearing housing. Thus a bearing housing is placed on the upper bracket. The loads on the bevel gears act not only in the vertical direction, but also in the horizontal direction. So, fixtures are considered on the shaft for bevel gears and lower bracket arm. A nut is fitted at the end of the shaft. Rotation of the lower arm bracket about the shaft is constrained by using setscrew and a flat surface on the shaft.

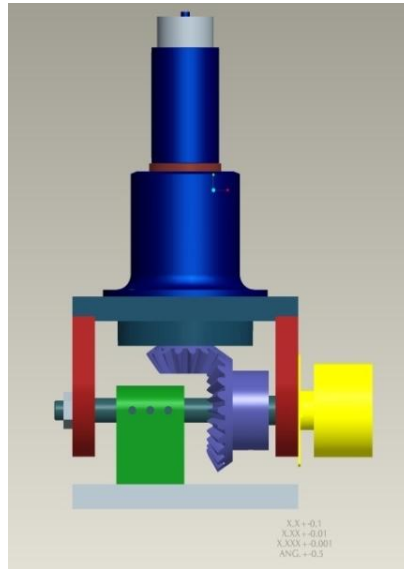


Figure 4.20 Third version of the knee joint design, (September 2008)

In Figure 4.21 fourth version of the knee design is shown. In this version, manufacturing and assembly convenience were standing in the forefront of the design. The rounded edges turn into chamfers and upper bracket is divided into four pieces. For ease of assembly, fixture and fittings have been created. Flanges are embedded into lower and upper bracket for example. Also rotation of the gear about the shaft is constrained by using a setscrew and a flat surface on the shaft.

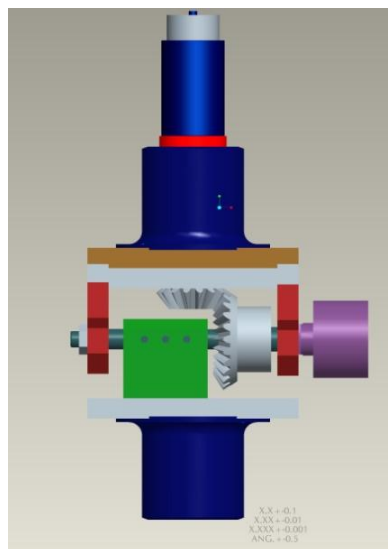


Figure 4.21 Fourth version of the knee joint design, (October 2008)

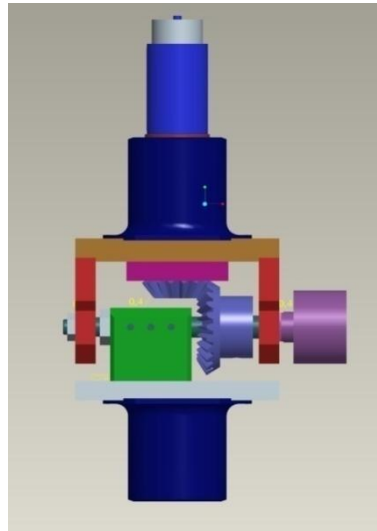


Figure 4.22 Fifth version of the knee joint design, (December 2008)

Figure 4.22 shows the fifth version of the knee design. For the sake of lightweight design, the bearing housing part (purple part) has been designed smaller. To prevent the axial movement of the lower bracket arm (green part), a fixture on shaft and a nut is used.

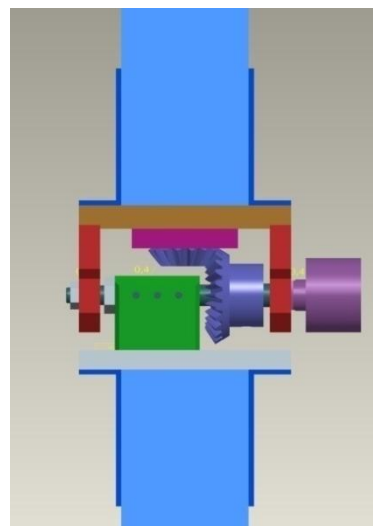


Figure 4.23 Final version of the knee joint design, (January 2009)

Finally in Figure 4.23, cylindrical legs and flanges are substituted with gussets and square shaped profiles for ease of assembly. This final version is chosen for manufacturing. Fittings for motor on the upper bracket and for lower bracket arm on lower



bracket are created in this version. Detailed screw holes and their fittings are created. Tolerances on bearing bushings, fittings and detailed blueprint drawings are generated for manufacturing.

In Figure 4.24, three dimensional assembly view of the knee joint can be seen. Fixtures that restrict movement of the lateral brackets are displayed clearly in this figure. On down upper bracket (purple) and lower bracket (gray) screw fittings for embedding the head of the screw into brackets are displayed. Lateral bearings and their holes on lateral bearings are clearly demonstrated. This three dimensional figure helps understand the design motivation. Chamfers are made for ease of manufacturing.

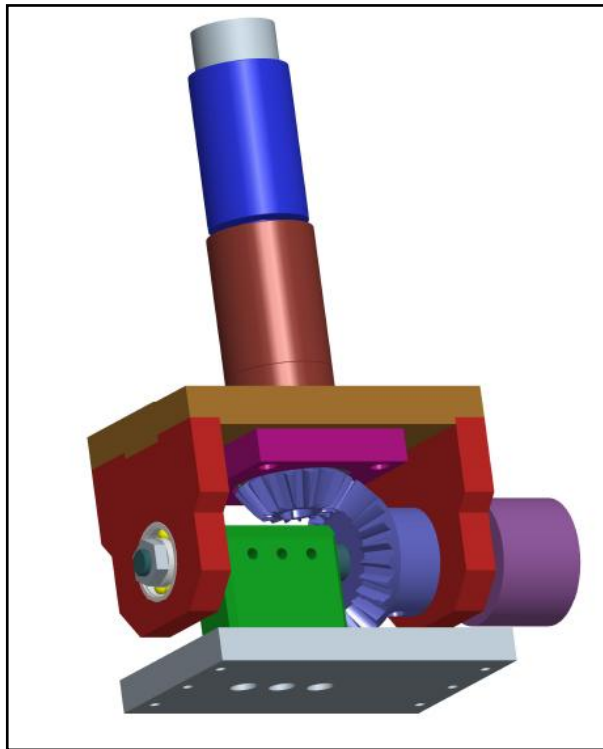


Figure 4.24 Three dimensional view of the knee joint

Exploded view in Figure 4.25 shows the knee joint assembly part by part. Details of each part can be seen clearly. Knee joint assembly consists 16 parts that are assembled by us (motor, gearhead and internal encoder purchased as a package). These parts can be listed as, 2 lateral brackets (red), 2 nuts, upper bracket (brown), 2 lateral bearings, motor bearing that compensates for the thrust forces on the motor, housing to mount this crossed

roller bearing (purple), 2 bevel gears, steel shaft, lower bracket arm, lower bracket, external encoder and motor, gearhead, internal encoder package. Fixtures on the shaft, lower brackets, and upper bracket are displayed. There are two flat surfaces on the shaft on which the setscrews of gear and lower arm bracket press. There are six screws that pass through the clearance fit holes on gussets and top upper brackets and they are screwed on threaded screw holes on the top of the lateral brackets. The same fixing methods are utilized for parts below the knee joint, except threaded holes are made on lower bracket. Three screws keep the lower bracket arm and lower bracket together. Fixtures on motor gearhead can be listed as four screws for fixing the gearhead to upper bracket and pinion is fixed to gearhead shaft by a key.

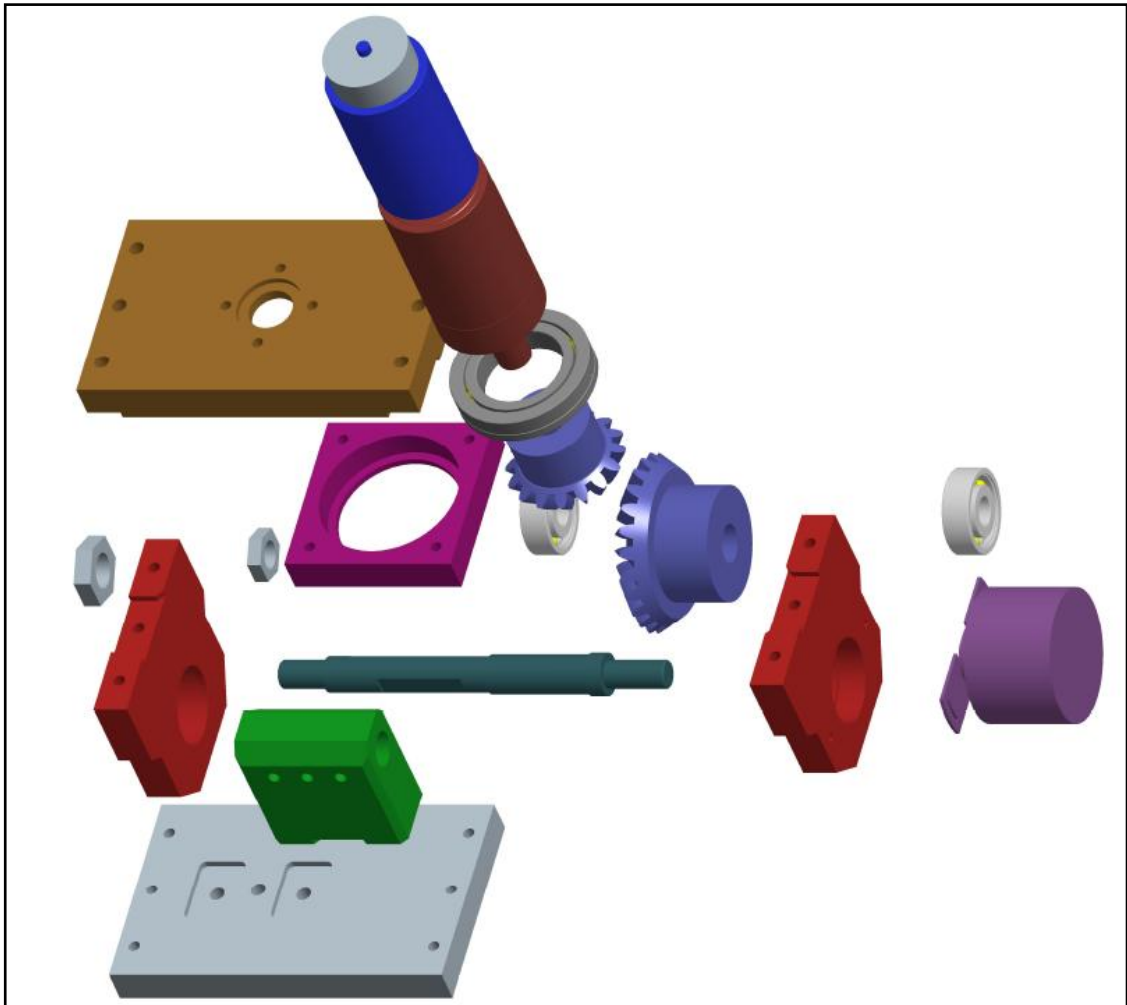


Figure 4.25 Exploded view of the knee joint assembly

### 4.5.2. Hip Joint Design

Design of the hip joint is less complicated compared to knee and ankle joints. Mainly due to lower moment requirements, no reduction such as bevel gears is needed. Different from the knee joint section, only final version of the hip joint is illustrated in this section. Figure 4.26 shows the three dimensional view of the final version of the hip joint. For manufacturing convenience, lateral brackets and bearings, lower arm bracket, external encoder and motor set are kept the same. The knee joint upper bracket and shaft are modified due to change in application. Power transmission from the motor to the joint was done by direct coupling. For this purpose, new components are added to the design like motor bracket and a coupling (dark brown). Thus upper bracket is extended. Despite the extension of the whole joint, hip shaft has become shorter because bevel gears are not used in the hip joint. A custom made coupling is used because there is no coupling in the market with the desired dimensions and strength. To provide symmetry, lower bracket is mounted to lower bracket arm in the middle.

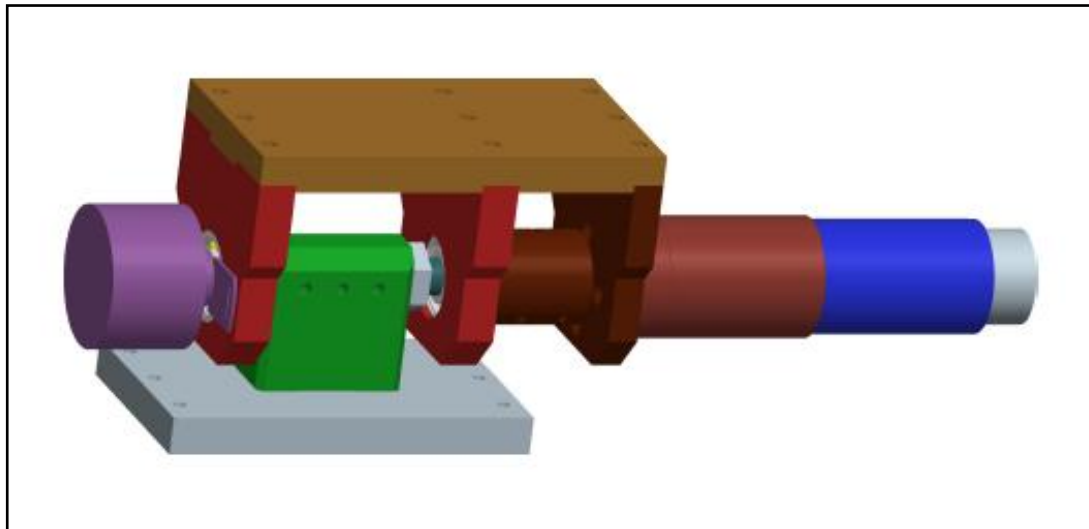


Figure 4.26 Three dimensional view of the hip joint

Exploded view of the hip joint is shown in Figure 4.27. In this design, fittings and fixtures are used similar to the ones in the knee joint design. The difference was in the location of the fittings. Power transmission line can be seen clearly in this figure. Coupling is mounted the gearhead shaft by a key and on the other side, its mounted to the joint shaft

by a setscrew and a flat surface. Finally, interference fit is obtained by tightening the screws on the coupling. To tighten the joint and gearhead shaft separately, slots on the shaft are made in axial direction and radial direction.

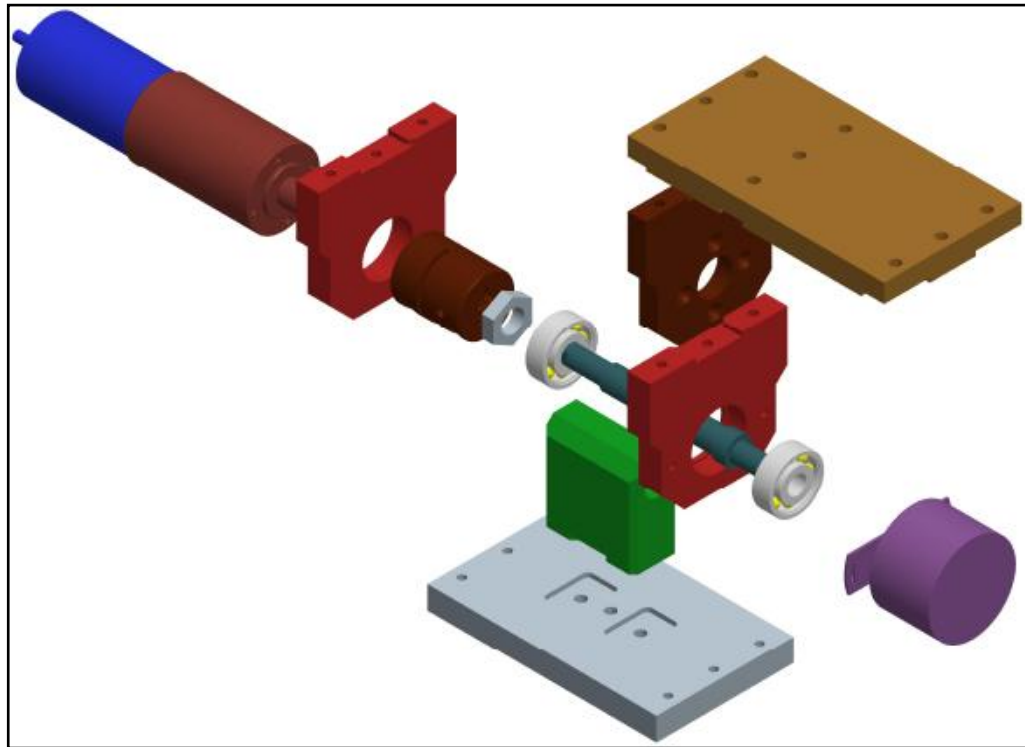


Figure 4.27 Exploded view of the hip joint assembly

### 4.5.3. Ankle Joint Design

After knee joint is designed, ankle is modified from it. Bevel gears and gearhead have larger reduction ratios than the ones in the knee. Larger reduction means larger dimensions, so modification is focused on this issue. Figure 4.28 and Figure 4.29 show the three dimensional and exploded view of the ankle joint assembly. Setscrew and flat surfaces is not preferred to constrain the rotation of the gear about shaft. Instead, a key is fixed on the shaft and a key way is cut on the gear. Pitch diameter of the gear is increased, which means an extension along the vertical dimension of the whole joint. In order to do this, lower arm bracket and lateral brackets are extended. Motor gearhead have a larger diameter. Thus, fixtures and fittings on upper bracket of motor gearhead are changed.

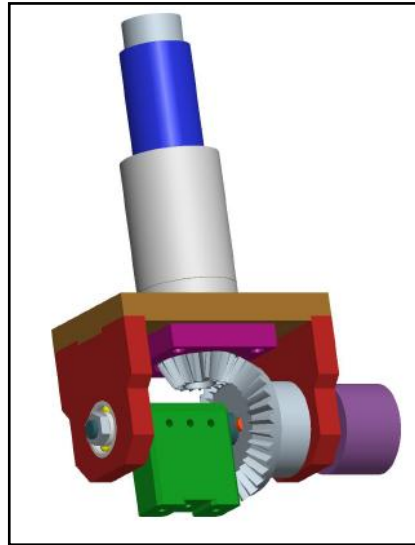


Figure 4.28 Three dimensional view of the ankle joint

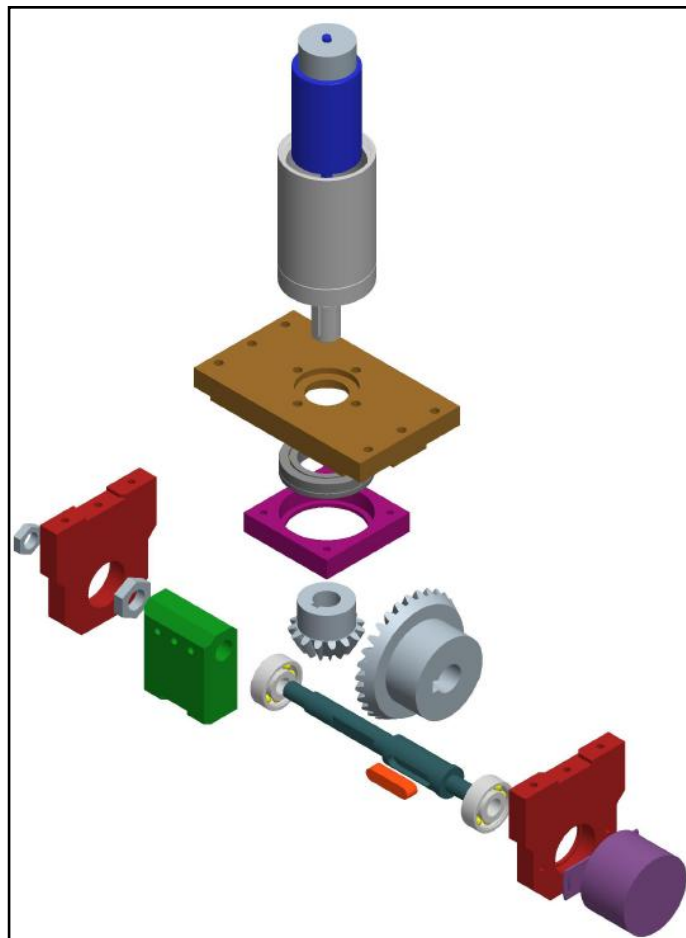


Figure 4.29 Exploded view of the ankle joint assembly

#### 4.5.4. Foot Design

After force sensors are selected, design of the foot has taken place. Figure 4.30 shows the exploded view of the foot assembly. Main criteria in foot design are ease of manufacturing and features for FSR sensor mounting. For ease of machinability, foot is divided into two main pieces. Upper part is designed to mount directly to the lower bracket arm of the ankle joint. One of the considerations in foot design was to transmit ground reaction forces to FSR sensor properly. To protect the sensor and reduce the effect of the impact, rubber is selected as a material to absorb the ground contact force (green). FSR sensors are mounted at the corners of bottom surface of the upper piece by an adhesive. Retaining rings are used to keep rubbers on FSR sensors when the foot is in the air.

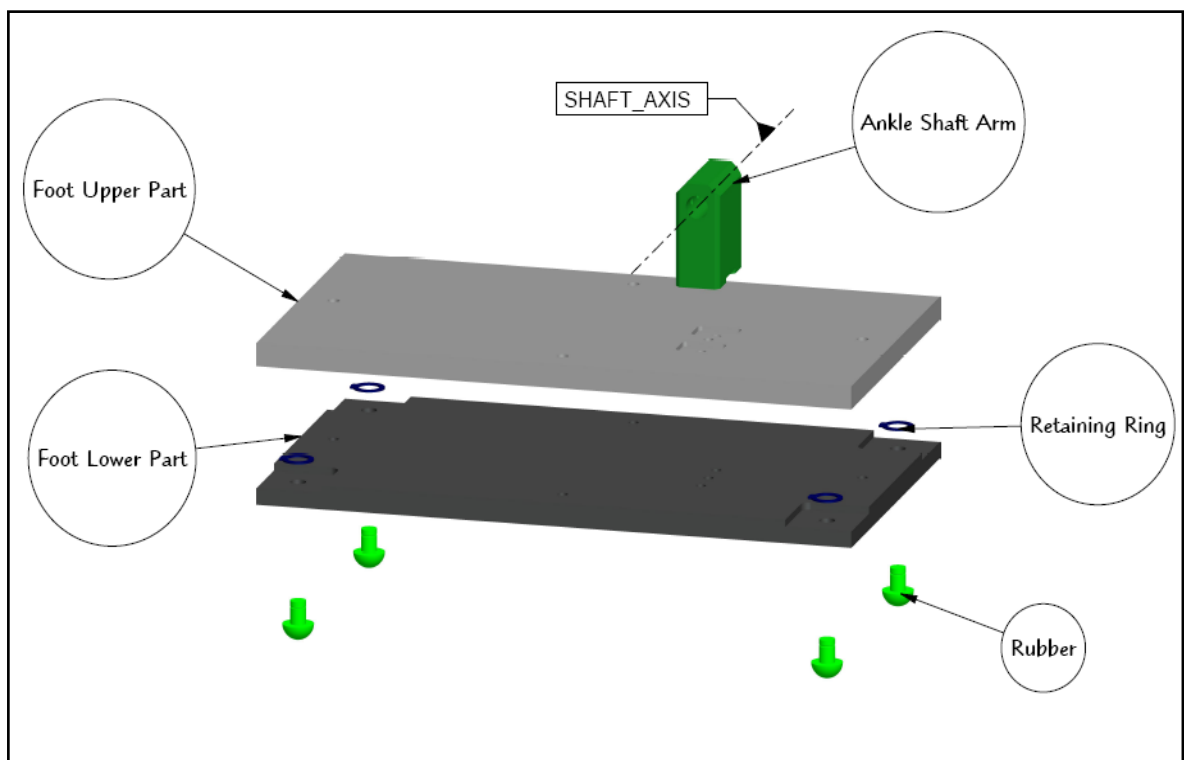


Figure 4.30 Exploded view of the foot assembly

#### 4.6. PROTOTYPING

Prototyping process is divided into 3 main sub processes, after the raw material is obtained. These main sub processes are dimensioning, manufacturing and assembly. While

milling cutter, bench drill and turning lathe is used in the manufacturing processes, dimensioning process requires intense usage of marking gauge, caliper gage, several micrometers and dial gauges. Three dimensional CAD files are converted into two dimensional technical drawings with fitting tolerances.

A typical procedure is followed for prototyping of each part. This procedure starts with a marking process of raw materials on a granite plate. Marking gauge is used to specify the contours of cutting lines on raw materials and locating the centers of holes by a drill bit. Then, exterior surfaces are handled in milling cutter except the shafts. The holes with tolerances are treated on turning lathe by using a lever gauge. Other holes are drilled in the bench drill. Meshing teeth of all gears have been hardened by induction hardening treatment.



Figure 4.31 First assembled prototype of the knee joint

Since the computer aided design has started from the knee joint, the prototyping process has also started from the knee joint. Figure 4.31 illustrates the first prototype of the knee joint assembly. As shown in the picture every component is fitted and mounted to one another as shown in the CAD design.

The first knee assembly production attempt is finished with success. Then, the thigh and shank limbs and gussets are cut into desired lengths by the circular saw machine. Raw material for the limbs is 60x60 mm aluminum square profile and for the gussets is 70x20 mm aluminum L profile. Figure 4.32 presents the mounted limbs, gussets and knee joint. Gussets are mounted to limbs by four screws and to the knee by three screws. Electrical assembly can also be seen in this figure. Electrical assembly consists of motor and encoder connections to EPOS2 controller.

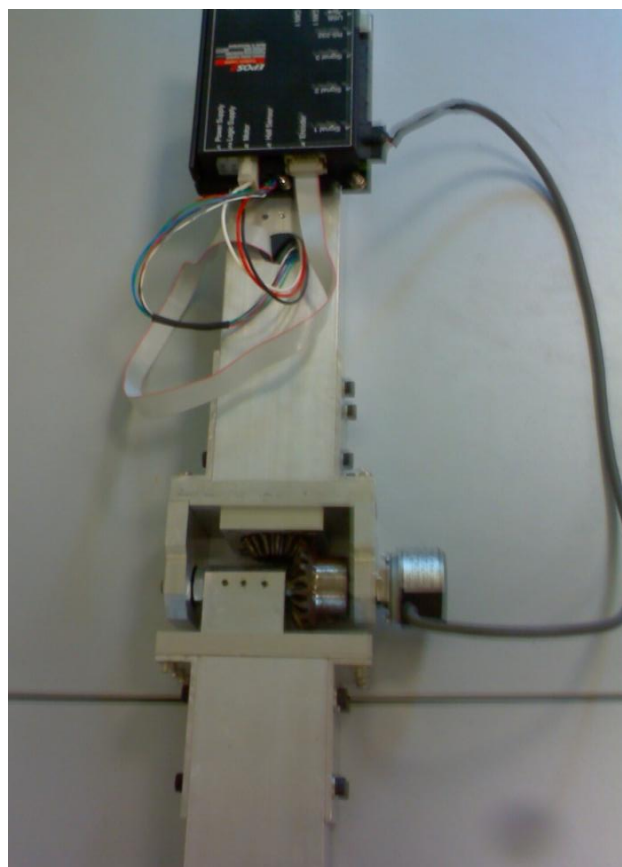


Figure 4.32 Assembled knee joint and limbs

By the success of the first knee joint prototype, other knee joint and limbs are manufactured. Next milestone was hip joint as shown in Figure 4.33 and Figure 4.34. Lateral and lower arm of hip joints were the same as the ones in the knee joint. The process was also the same for every part except the couplings. All the fixtures of the shafts are machined in turning lathe besides flat surfaces. Flat surfaces are made by milling cutter. All the screw threads are cut manually by using a die. A complicated part in the hip joint



was the coupling, since tools in the university were insufficient to manufacture this part. Holes were too small to machine a keyway for gearhead shaft. Narrow gaps make it difficult to machine it in the milling cutter. Thus, it is sent to an outside machine shop for wire erosion machining.

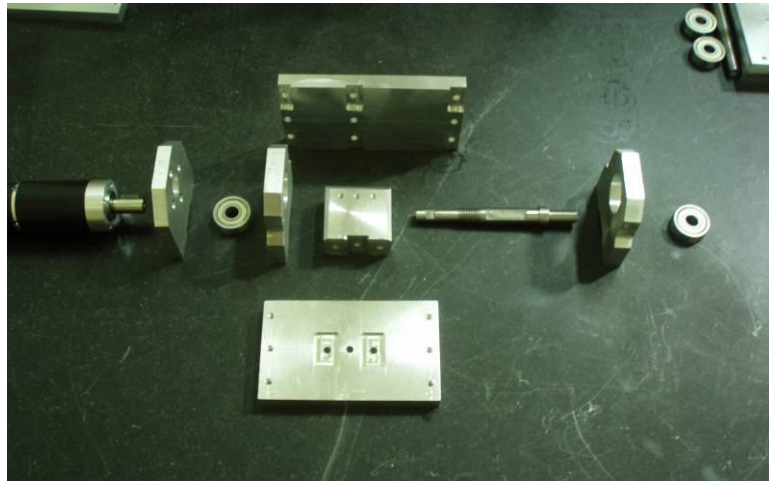


Figure 4.33 Picture of the disassembled hip joint parts

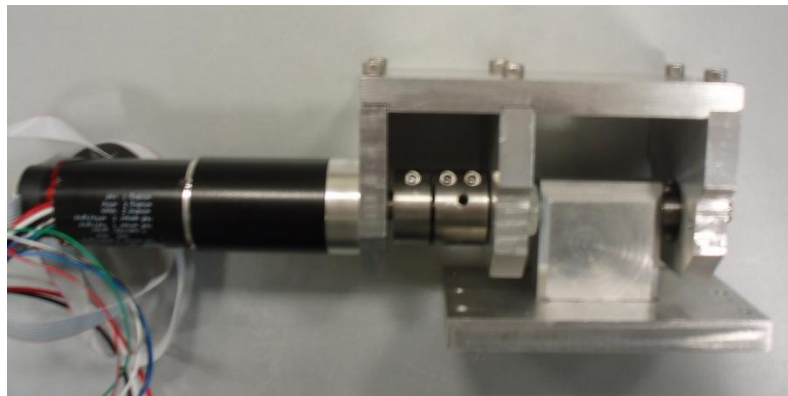


Figure 4.34 Picture of the assembled hip joint

The last and the hardest joint to manufacture is the ankle joint. Figure 4.35 and Figure 4.36 shows the manufactured parts separately and as assembled, respectively. Although the lateral, lower and bottom upper brackets are similar to the knee joint parts, upper bracket and shaft have more complex geometry than the corresponding parts in the knee joint. As a result of high moment requirement of the ankle joint, gear has been fixed

to the shaft by a key and gearhead diameter has been increased. To use a key for fixation, a key scot is needed on the shaft and it is produced by the milling cutter process. Motor gearhead is mounted to the upper bracket by four screws.



Figure 4.35 Picture of the disassembled ankle joint parts



Figure 4.36 Picture of assembled ankle joint parts

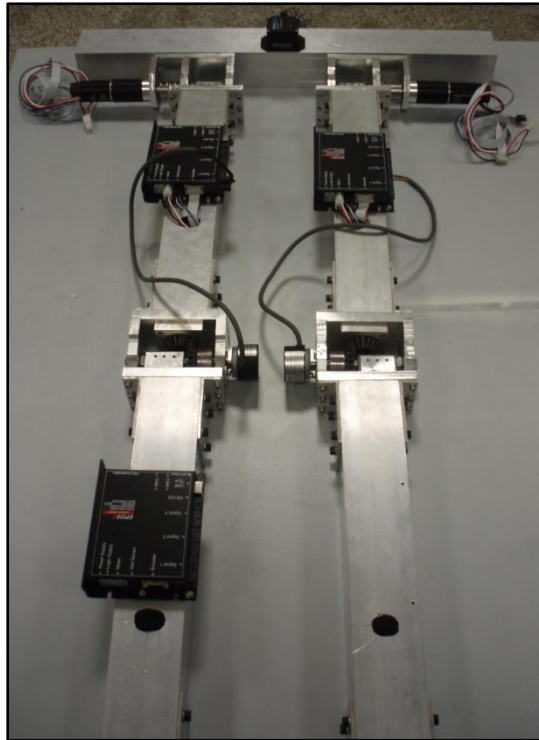


Figure 4.37 Assembly of the whole robot

Whole robot assembly is shown in Figure 4.37. All components of the biped robot are manufactured and assembled except the feet. All of the robot's components are selected based on the simulation results and design considerations. Then, detailed design for hip, knee and ankle joints are obtained in the CAD environment. Structural, electrical and control system components are assembled with the joint models.

## 5. CONCLUSION AND FUTURE WORKS

A planar biped robot is modeled, simulated and designed within the scope of this thesis. Modeling had been started from a model with two links and a hip joint called the simplest walker and gone through the gait generation program in MATLAB. In the design section, all of the components of the robot are selected and assembled in the CAD software and most parts are manufactured and assembled. Simulations are also performed for the simplest walker by using MATLAB and ADAMS software and had been enhanced to a faithful model of the prototyped robot in ADAMS software.

A preliminary study in the modeling and simulations section was the simplest walker. Simplest walker gave information about the specifics of walking. After simplest walker, a seven link, anthropomorphic biped robot model is generated in ADAMS software. Each joint is driven by human gait data obtained from the literature [32]. By fixing the stance foot of the robot to the ground, power and moment based simulation results that lead to the actuator design are obtained. Offline gait trajectory generation is used in this study. For this purpose, a gait generation function is created in MATLAB. This function generates ankle and hip joint trajectories by generating cubic splines from characteristic via points in cartesian coordinates. Knee joint trajectory is solved from kinematics and cartesian joint trajectories are converted to angular joint trajectories by inverse kinematics. A realistic simulation environment is created in ADAMS software by generating an identical model of the manufactured robot. An impact contact model and coulomb friction model is used for simulating interaction of the robot with the ground. Two different gait trajectories are applied to this model and the simulation results are obtained.

In the design and prototyping section, all of the robot's components are selected based on the simulation results and design considerations. Then, detailed design for hip, knee and ankle joints are obtained in the CAD environment. Structural, electrical and control system components are assembled with the joint models. Foot design is assembled with force sensitive resistor (FSR) sensors. All components of the biped robot are manufactured and assembled except the feet.

Control, stability and gait optimization sections of the robot were not the primary concern in this study. These subjects are not crucial for obtaining a walking mechanism but necessary to obtain a human like walking biped robot. The selected electronics and sensors are already suitable for creating a real time sensor based control or real time trajectory update by using the sensor data in the future. For example, selected force sensors are suitable for the ZMP based control. Gait generation method in this study has 12 gait parameters that can be optimized. Thus, generated trajectories can be optimized with respect to stability or power consumption criteria. Identical ADAMS model can be used as a test bed for the development of advanced control strategies and optimized gait trajectories.

## REFERENCES

1. Hase K., M. Yamazaki, "Computer simulation of the ontogeny of bipedal walking", *Anthropological Science*, 106, 4, pp. 324-347, 1998.
2. Kato H., "Development of WABOT-1," *Biomechanism 2*, The University of Tokyo Press, pp. 173-214, 1973.
3. Sakagami Y., R. Watanabe, C. Aoyama, S. Matsunaga, N. Higaki, and K. Fujimura, "The intelligent ASIMO: System overview and integration" *In Proceedings of IEEE/RSJ International Conference on Intelligent Robots and Systems*, Lausanne, Switzerland, pp. 2478-2483, 2002.
4. Sony, *Sony develops small biped entertainment robot*, <http://www.sony.co.jp/en/>, 2002.
5. Raibert M.H., H.B. Brown, Jr., and M. Chepponis, "Experiments in balance with a 3D one legged hopping machine", *International Journal of Robotics Research*, Res. 3, pp. 75-92, 1984.
6. McGeer T., "Passive Dynamic Walking", *International Journal of Robotics Research*, vol.9, no.2, pp. 62-82, 1990.
7. Goswami A., B. Thuilot, B. Espiau, "Compass-like biped robot Part I: Stability and bifurcation of passive gaits", *INRIA research report, no 2996*, 1996.
8. Thuilot B.; A. Goswami, B. Espiau, "Bifurcation and Chaos in a Simple Passive Bipedal Gait", *IEEE International Conference on Robotics and Automation*, New Mexico, 1997.
9. Spong M. W., "Passivity Based Control of the Compass Gait Biped", *IFAC World Congress*, Beijing China, B, pp 17-24, 1998.

10. Pratt J.E., M.C. Chee, A. Torres, P. Dilworth, and G.A. Pratt, "Virtual model control: An intuitive approach for bipedal locomotion," *International Journal of Robotics Research*, vol. 20, pp. 129-143, 2001.
11. Vukobratović M., B. Branislav, "Zero-Moment Point – Thirty Five Years of its Life", *International Journal of Humanoid Robotics*, v.1, n.1, pp. 157-173, 2004.
12. Hirai K., M. Hirose, Y. Haikawa, & T. Takenaka, "The development of Honda humanoid robot", *IEEE International Conference on Robotics and Automation*, 1998.
13. Huang Q., K. Yokoi, S. Kajita, K. Kaneko, H. Arai, N. Koyachi & K. Tanie, "Planning Walking Patterns for a Biped Robot", *IEEE Transactions on Robotics and Automation*, 2001.
14. Yamaguchi J., E. Soga, S. Inoue, & A. Takanishi, "Development of a bipedal humanoid robot-control method of whole body cooperative dynamic biped walking", *IEEE International Conference on Robotics and Automation*, 1999.
15. Kajita, S., & K. Tani, "Study of dynamic biped locomotion on rugged terrain-derivation and application of the linear inverted pendulum mode", *IEEE International Conference on Robotics and Automation*, 1991.
16. Minakata, H., & Y. Hori, "Real-time speed-changeable biped walking by controlling the parameter of virtual inverted pendulum", *International Conference on Industrial Electronics, Control and Instrumentation*, 1994.
17. Napoleon, Nakaura, S., & Sampei, M., "Balance control analysis of humanoid robot based on zmp feedback control", *IEEE/RSJ International Conference on Intelligent Robots and System*, 2002.
18. Arakawa T., & T. Fukuda, "Natural motion generation of biped locomotion robot using hierarchical trajectory generation method consisting of ga, ep layers", *IEEE International Conference on Robotics and Automation*, 1997.

19. Nagasaka K., H. Inoue, & M. Inaba, "Dynamic walking pattern generation for a humanoid robot based on optimal gradient method", *IEEE International Conference on Systems, Man, and Cybernetics*, 1999.
20. Huang Q., K. Kaneko, K. Yokoi, S. Kajita, T. Kotoku, N. Koyachi, et al., "Balance control of a biped robot combining off-line pattern with real-time modification", *IEEE International Conference on Robotics and Automation*, 2000.
21. Hirai K., M. Hirose, Y. Haikawa, & T. Takenaka, "The development of Honda humanoid robot", *IEEE International Conference on Robotics and Automation*, 1998.
22. Park J. H. & H. C. Cho, "An online trajectory modifier for the base link of biped robots to enhance locomotion stability", *IEEE International Conference on Robotics and Automation*, 2000.
23. Yamane K., & Y. Nakamura, "Dynamics filter concept and implementation of online motion generator for human figures", *IEEE International Conference on Robotics and Automation*, 2000.
24. Nakamura Y., & K. Yamane, "Interactive motion generation of humanoid robot via dynamics filter", *IEEE-RAS International Conference on Humanoid Robots*, 2000.
25. Nishiwaki K., S. Kagami, Y. Kuniyoshi, M. Inaba, & H. Inoue, "Online generation of humanoid walking motion based on a fast generation method of motion pattern that follows desired zmp", *IEEE/RSJ International Conference on Intelligent Robots and System*, 2002.
26. Kagami S., T. Kitagawa, K. Nishiwaki, T. Sugihara, M. Inaba, & H. Inoue, "A fast dynamically equilibrated walking trajectory generation method of humanoid robot", *Autonomous Robots*, 12(1), pp. 71-82, 2002.
27. Matsuoka K., "Mechanisms of frequency and pattern control in the neural rhythm generators", *Biological Cybernetics*, 56(5-6), pp. 345-353, 1987.



28. Taga G., Y. Yamaguchi, & H. Shimizu, "Self-organized control of bipedal locomotion by neural oscillators in unpredictable environment", *Biological Cybernetics*, 65(3), pp. 147-159, 1991.
29. Nakanishi J., J. Morimoto, G. Endo, S. Schaal, & M. Kawato, "Learning from demonstration and adaptation of biped locomotion with dynamical movement primitives" *IEEE/RSJ International Conference on Intelligent Robots and Systems*, 2003.
30. Garcia M., A. Chatterjee, A. Ruina, M. Coleman, "The Simplest Walking Model: Stability, Complexity, and Scaling", *Department of Theoretical and Applied Mechanics, Cornell University*, 1998.
31. Personal communication with Assist. Prof. Koray K. Şafak.
32. David A. Winter, *Biomechanics and motor control of human movement 3rd ed.*, Hoboken, N.J, John Wiley & Sons, 2005.
33. *Maxon Motor Catalog*, [www.maxonmotor.com](http://www.maxonmotor.com), 2009.
34. *Nemicon Encoders*, <http://www.nemicon.com>, 2009.
35. *Microstrain Orientation Sensors*, <http://www.microstrain.com>, 2009.
36. *Tekscan Pressure Mapping and Force Measurement*, Tekscan Electronics Integration Guide (For FlexiForce Sensors) (Rev A) <http://www.tekscan.com/flexiforce.html>, 2009.
37. Atlanta Drive Systems, Straight Bevel Gear Sets, [http://www.atlantadrives.com/pdf/ads\\_elements-d.pdf](http://www.atlantadrives.com/pdf/ads_elements-d.pdf), 2008.
38. Matweb, *material property database*, <http://www.matweb.com>, 2009.